Controlling Cavity Magnon Polariton Properties in Frequency and Time Domain

zur Erlangung des akademischen Grades

DOKTOR DER NATURWISSENSCHAFTEN (Dr. rer. nat.)

von der KIT-Fakultät für Physik des

Karlsruher Instituts für Technologie (KIT)

Genehmigte

Dissertation

von

M.Sc. TIM WOLZ

Contents

1 Introduction

The invention of the transistor and the concepts of digital circuit- and information theory [Sha38; Sha48] have spurred a revolution, which has transformed the economy and changed our every-day's life. This transformation has been backed by the exponential increase in computing power, as described by Moore's law. And as of 2021, more than half of the world's population owns a mobile phone and has access to the internet [Kem21]. With the advent of the internet, previously unthinkable technologies have emerged such as artificial intelligence, cloud computing, on-demand streaming, virtual reality, and block chains together with crypto currencies [Nak08].

The rapid spread of these new technologies and digital devices, however, poses significant problems. First, Moore's law of always more is accompanied by an ever stronger hunger for energy. The energy consumption of the information and communication technology (ICT) sector is expected to make up one fifth of the global energy need in 2030 [AE15; Jon18]. A prime example is given by the bitcoin block chain, which already requires an amount of energy equaling the expenditure of whole countries, such as Norway and Argentina [Rau+]. The culprit behind this energy consumption is the heat dissipation due to Ohmic losses while storing and transferring data. A quest for alternative technologies trying to circumvent Ohmic loss has hence begun and the fields of spintronics [XAN16] and magnonics [ŽFD04; KDG10; SCH10; CSH14; Kar+16] already offer a possible rescue. In both cases, the spins of electrons instead of charge carriers are utilized for lossless information processing. Magnonics, in particular, specializes on the collective excitations of spins, so-called spin waves or magnons.

But the energy hunger alone is not ICT's only problem. With huge amounts of gathered and generated data, the complexity of problems increases and many of them, so called NP-hard problems, scale non-polynomial with the size of input data. These problems are beyond reach for classical computers but solving them promises great progress in chemistry, drug discovery, secure communication, and optimization algorithms. Here, quantum computing is believed to play the crucial role [Pre18; Cao+19; Gis+02; All+14; Bia+17]. It harnesses quantum mechanical features, such as superposition and entanglement for calculations, empowering

quantum algorithms, e.g., Shor's prime factorization [Sho97] and Grover's search algorithm [Gro96], which can crack NP problems in reasonable time. A promising physical realization of quantum bits (qubits) are superconducting circuits [Kra+19]. Their quantum behavior can be engineered via controllable circuit parameters and the quantum state of the system is encoded in electromagnetic modes. This allows for a read out of the quantum state by probing an LC resonator with photons in the GHz regime [Bla+04]. In 2019, the Google group, for instance, already demonstrated quantum supremacy (an exponentially faster calculation than any classical computer) for a specific problem solved with 50 superconducting qubits [Aru+19], illustrating the progress in this field.

Now considering both described challenges together, one can easily imagine the need for a hybridization of the different fields to develop energy efficient yet powerful computational devices. However, information is encoded into different physical realizations, magnetic spins versus microwave photons, which raises the question: How can we transfer information between these two? The cavity-magnon polariton (CMP) [Hue+13; Zha+14; Tab+15; HH18] gives a possible answer. The CMP is the quasi particle of a coupled system consisting of an LC resonator (cavity) and a magnetic material (magnon). Due to its electromagnetic coupling [Bai+15], photon excitations can be transferred to spin excitations and vice versa. This ability casts the CMP as an ideal candidate for so-called "hybrid magnonics" [Li+20; Lac+19], see Fig. 1.1. First publications have already demonstrated the coupling of magnons to a superconducting qubit [Tab+16; Lac+17; Pfi19; Lac+20], with the qubit acting as a sensor for single magnons, for example. Moreover, theoretical proposals exist for an encoding of quantum states in magnons [EBB20; RZ69]. A possible way would be through a shared anharmonicity via the coupling to a superconducting qubit, similar to the research on superconducting resonators [Hof+08]. Additionally, the CMP also allows for a radiofrequncy to light conversion [His+16; Zha+16; Osa+16; Hai+16] opening ways to information transfer based on visible light and hence offering a route to a quantum internet [Kim08].

However, the CMP has by far not yet reached a competitive level for computational tasks compared to superconducting qubits. For the CMP to live up to the expectations as the interface for hybrid systems, a specific control of its fundamental properties is imperative. Data in the form of physical states need to be manipulated at will and stored sufficiently long. Translating this request into the language of a coupled system of oscillators implies controlling the following CMP properties: coupling strength, eigenmodes, and decay rates. Demonstrating such control options and their effects is the topic of this work.

The coupling strength defines the rate of energy exchange and hence controlling this rate would increase the flexibility of coherent information exchange. Normally,
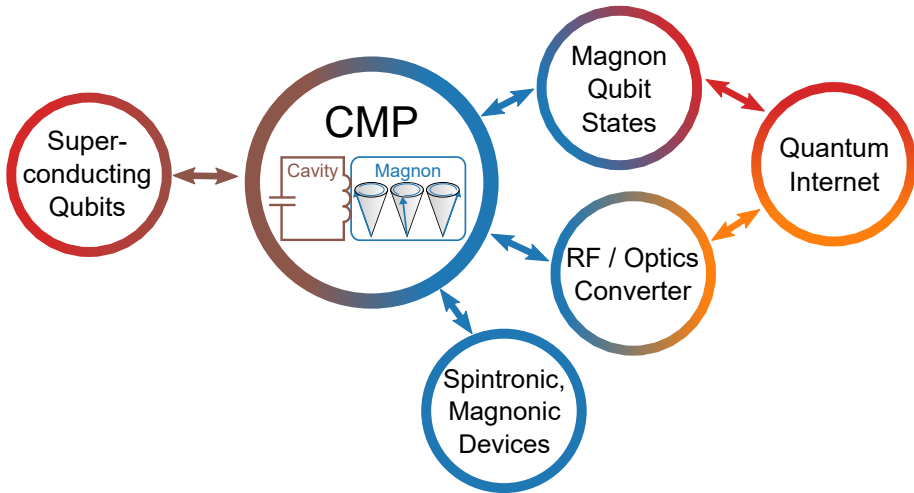
Figure 1.1: The cavity magnon polariton (CMP) as a possible interface between different future information technologies. Colors of the circle represent the several physical implementations of information processing technologies. Red highlights quantum computing, brown represents information in the form of radio frequency photons as stored in a cavity, blue devices are based on magnons and yellow stands for optical technologies. Due to its light-matter combination, the CMP can couple via the cavity part to superconducting qubits and then transfer the information to either spintronic and magnonic devices or convert radio frequency photons into the optical regime, which may be useful for a quantum internet. Another possibility is given by a shared anharmonicity between superconducting qubits and magnons allowing for magnon qubit states.

the coupling strength is fixed by the geometric design [Zha+14; Flo+19] and leads to the typical mode repulsion. However, adding dissipation to the coupling process [WH20] changes the picture. The two eigenmodes do not repel but attract each other [Har+18; PMS19; Yao+19b; Bho+19]. Again, a dissipative coupling can be achieved by a specific geometric design of the CMP. Such a design constraint prevents an easy switching between the two regimes. Yet, we will see in this work that based on the proposal of Ref. [GSX18] coherent microwave tones can be employed to not only control the amount of the repulsive coupling strength but also to generate level attraction during the experiment [Bov+20; Bov+19].

For computational tasks a *fast* change between the different states of the physical system is necessary. Despite this need, the CMP has mostly been probed by a continuous drive tone only yielding the steady-state response. And in the few pulsed experiments[Zha+14; Zha+15; Mat+19] only the cavity has been excited. Such a pulse scheme, however cannot switch between the different modes of the CMP. In this work, we also demonstrate that a fast manipulation is possible with a

second short but coherent drive pulse to the magnon system, which enables us to exert control over the CMP modes [Wol+20].

Progress on the manipulation of different states is only one necessary part towards CMP based information processing. Another crucial goal is a sufficiently long storage of information. Here, the decay rate, or rather its inverse, the life- (and coherence) time of any system, is a measure of how long (quantum) information is preserved. Superconducting qubits show coherence times of several 100 μs [Pla+20]. The longest life time of a spin wave, however, is only on the order of few μs [SLL61]. It is evident that the magnon life time has to be improved to keep up with superconducting qubits and to build a useful connection between the two of them. Improving the life time requires a fundamental understanding of the loss-mechanisms in the system, but little is known about these mechanisms at mK temperatures, the required environment for superconducting qubits. A few experiments have indicated the influence of two-level systems (TLS) [Tab+14; Pfi+19; Kos+19]. Inspired by the TLS research on superconducting resonators [Gao+07; Bur+14], we perform a frequency noise spectroscopy of the magnon resonance, i.e., tracking frequency fluctuations over time, to gain new insights about loss mechanisms.

This thesis is structured as follows: After a brief overview of the physical background for the CMP in Ch. 2 and how to access it with microwave tones (Ch. 3), we will tackle the three points presented above: In Ch. 4, we will discuss the CMP driven with a second continuous but phase-coherent microwave tone directly applied to the magnon system. The underlying theory will be presented with a focus on the control of the coupling strength by the external parameters of the drive tones. Its experimental demonstration is given in Refs. [Bov+20; Bov+19]. The two-tone experiment is taken one step further in Ch. 5. Employing a time-domain setup, adapted from qubit experiments, we manipulate the different states of the CMP with short pulses in the nanosecond regime and seize control over state superposition and total energy in the system [Wol+20]. The magnon coherence is addressed in Ch. 6, where frequency noise is measured and subsequently investigated with time series analysis. At last, Ch. 7 summarizes and concludes this work.

2 The Cavity Magnon Polariton (CMP)

The cavity magnon polariton (CMP) is a quasi-particle arising from the hybridization of photon and magnon. The photonic part originates from cavity excitations and the magnonic part represents spin wave excitations in magnetic materials. To understand the physics behind the CMP, we will first focus on the two uncoupled systems, i.e., microwave resonator and ferromagnetic resonance. And then study three different models that elucidate the coupling mechanism of these systems and give rise to the CMP. After having understood the coupling process, we will discuss different coupling regimes in general. All regimes exhibit distinct physical behaviors, which may be interesting for future information processing; foremost the coherent energy exchange in the strong coupling regime, where the experiments are based upon in Ch. 4 and 5. At last, we will come back to the magnetic part only, and examine the coherence properties of spin waves in YIG more closely, which will be built upon in Ch. 6.

2.1 Microwave Resonators and Cavities

The first part of creating a CMP requires, as the name suggests, a cavity; or more generally a microwave resonator (see Fig. 2.1a), representing the photonic part. In a cavity, the electromagnetic fields are confined and hence standing waves emerge at specific fixed frequencies ω_c. The behavior of a microwave resonator [Poz12] is governed by the well-known RLC model, Fig. 2.1b, which is also essential for the electromagnetic coupling model [Bai+15] in Sec. 2.3.2. Using the current density j flowing through the cavity walls, we can write the differential equation of the RLC model as

$$Rj(t) + \frac{1}{C} \int j(t)\mathrm{d}t + L\frac{\mathrm{d}j(t)}{\mathrm{d}t} = V(t). \tag{2.1}$$

R denotes the cavity's resistance, L its inductance and C its capacitance. The cavity is connected to the environment and driven by a microwave field, which is
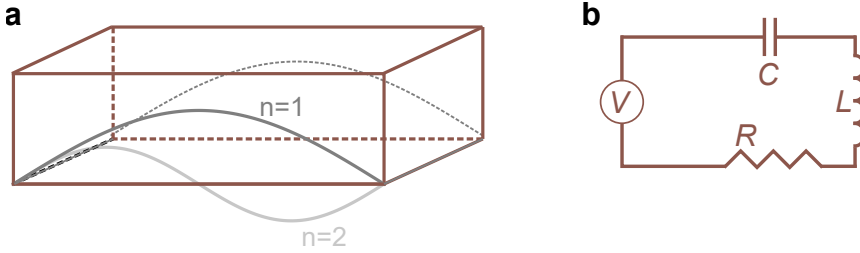
Figure 2.1: Cavity microwave resonator. Panel **a** shows a sketch of a rectangular microwave cavity with its first two resonating modes. Grey lines represent the voltage distribution along the surface with the long edge of the cavity. **b** RLC circuit as representation for a driven microwave cavity.

represented by its amplitude $V(t)$. A solution of the left hand part of Eq. (2.1) is of course a sinusoidal oscillation of the cavity current with resonance frequency $\omega_c = \sqrt{\omega_0^2 - \tilde{\beta}^2}$, including the natural frequency $\omega_0 = 1/\sqrt{LC}$ and $\tilde{\beta} = R/(2L)$. The resistance leads to energy loss and hence broadens the resonance linewidth, which is a measure for the lifetime of the excitation. Achieving a narrow linewidth is crucial for future information processing applications. In Sec. 3.1, we will study the linewidth in more detail and see how we can extract the important physical quantities of a resonating system from the response to a continuous drive field.

2.2 Ferromagnetic Resonance, Spin Waves and Magnons

We now switch to the second oscillating system in the CMP: the magnonic part, i.e., the ferromagnetic resonance (FMR) [Kit48]. This resonance arises from a collective oscillation of electron spins in a ferromagnetic material [1] and is also called spin wave or magnon as the associated quasi-particle. We will mainly discuss magnons in the language of quantum mechanics following Refs. [Tab+16; Kus19] and shortly from a classically viewpoint, to prepare for the discussion of different coupling models in the next section.

---

[1] Magnetic resonances also exist in antiferromagnetic and ferrimagnetic materials, with Yttrium-Iron-Garnet (YIG) being the most prominent example.
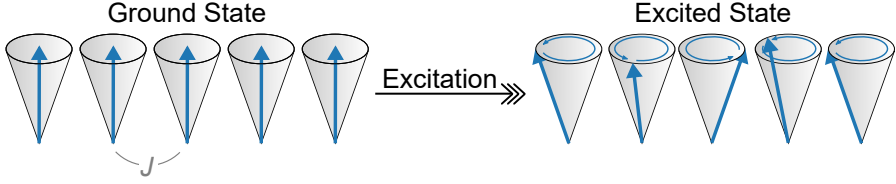
Figure 2.2: Spin wave representation in the Heisenberg model. Due to the exchange interaction J the spins' magnetic moments are aligned parallel in the ground state. However the first excited state does not consist of a single flipped state but of a spin wave. The z-component is aligned along the external field, whereas the xy components of the spin precess. For a better visualization, a higher order magnon modes is shown here, i.e., the spins do not precess uniformly.

Quantum Description

To understand magnons, let us first consider a one-dimensional chain of spin $1/2$ particles with their corresponding magnetic moments, i.e., three dimensional vectors in space, see Fig. 2.2. For the ferromagnetic case, an interaction between nearest neighbors exists that aligns the z-component of all spins in parallel and hence sets the ground state. Now, one may assume that the first exited state corresponds to one single flipped spin. However, this is not the case. The energy cost of flipping a single spin is too high. A more energetically favorable state can be achieved by spreading the equivalent excitation of a single spin over the whole range of the spin chain in the form of a spin wave. We can confirm this statement by looking at the Heisenberg Hamiltonian plus Zeeman term for a ferromagnet:

$$\mathcal{H} = -\frac{1}{2}J \sum_{\langle i,j \rangle} \mathbf{S_i} \cdot \mathbf{S_j} - g\mu_{\mathrm{B}} \sum_i \mathbf{H} \cdot \mathbf{S_i}, \tag{2.2}$$

with J as the exchange energy, $\mathbf{S}$ as the spin operator at lattice sites i, j, where the sum only considers nearest neighbors, $\mathbf{H}$ as the external magnetic field, and g, μ_{B} as Landé factor and Bohr magneton. Employing the spin-raising and spin-lowering operators $\mathbf{S}^{\pm}$ one can rewrite Eq. (2.2) to

$$\mathcal{H} = -\frac{1}{2}J \sum_{\langle i,j \rangle} S_i^z S_j^z - g\mu_b H \sum_i S_i^z - \frac{1}{4}J \sum_{\langle i,j \rangle} \left(S_i^+ S_j^- + S_i^- S_j^+ \right). \tag{2.3}$$

The last term shows that a single flipped spin cannot be an eigenstate of this Hamiltonian. The spin operators flip this spin and the neighboring spins as well. Hence, a spin flip propagates through the entire chain, resulting in a spin wave.

Working with spin operators can be cumbersome. The Holstein Primakoff Transformation (HPT) [HP40], however, provides a means to map spin operators to the

bosonic creation and annihilation operators $m, m^{\dagger}$ and we can describe spin waves in the occupation number representation (second quantization). The transformation of the spin operators is as follows:

$$S_+ = \hbar\sqrt{2s}\sqrt{1 - \frac{m^{\dagger}m}{2s}}\, m \approx \hbar\sqrt{2s}\, m, \qquad (2.4)$$

$$S_- = \hbar\sqrt{2s}\, m^{\dagger}\sqrt{1 - \frac{m^{\dagger}m}{2s}} \approx \hbar\sqrt{2s}\, m^{\dagger}, \qquad (2.5)$$

$$S_z = \hbar(s - m^{\dagger}m). \qquad (2.6)$$

One can see that the raising and lowering operators are associated with the annihilation and creation operators respectively - in first order. The spin number s for spin waves is high, which justifies this first order approximation in Eq. (2.4),(2.5). Together with the Fourier transformation of the bosonic ladder operators Eq. (2.3) can be rewritten to:

$$\mathcal{H} = \sum_{\mathbf{k}} \hbar\omega_{\mathbf{k}} m_{\mathbf{k}}^{\dagger} m_{\mathbf{k}}. \qquad (2.7)$$

This is the Hamiltonian of a (quantum) harmonic oscillator with resonance frequency $\omega_{\mathbf{k}}$. It simply follows from the above approximation. In the long wave length limit (small wave vector $\mathbf{k}$, compared to lattice constant a_0) one finds a quadratic dispersion relation with respect to $\mathbf{k}$:

$$\hbar\omega = 2sJa_0^2|\mathbf{k}|^2 + g\mu_{\mathrm{B}}B_z \qquad (2.8)$$

A special role plays the $\mathbf{k} = 0$ mode, the so-called Kittel mode, where all spins precess in phase and which is the only employed mode in this work. According to Eq. (2.8), the eigenfrequency of the Kittel mode follows a linear dispersion with respect to the external applied field, often abbreviated to $\omega = \gamma B$, with $\gamma/2\pi = g\mu_{\mathrm{B}}/h = 28\,\mathrm{GHz/T}$, allowing one to tune the FMR resonance frequency.

For the sake of completeness, it is mentioned that the finite sample geometry and hence its boundary conditions with the driving electromagnetic field play a more dominant role than the k^2-term in Eq. (2.8) [Tab+16]. Considering these conditions for a spherical geometry, Walker calculated the eigenfrequencies and the spin wave geometry for so-called higher order modes, magnetostatic modes or Walker modes [Wal57; Wal58]. Instead of spheres one could also use thin films of magnonic materials, often called magnonic wave guides. In these cases, one obtains still other dispersion properties of the magnetostatic modes, depending on the directions of wave vector and magnetic field [SCH10]. In this work, we focus on the uniform mode of spheres allowing us to neglect sample geometry effects.

Classical Description

Magnons can, of course, also be described classically. Especially for the uniform mode, it is intuitive to consider all precessing spins as one macrospin with magnetization $\mathbf{M}$ in an effective magnetic field $\mathbf{H}$. Its time-dependent behavior ("motion") is governed by the Landau-Lifshitz-Gilbert Equation (LLG) [LL35]

$$\frac{d\mathbf{M}}{dt} = \gamma \mathbf{M} \times \mathbf{H} - \frac{\alpha}{M}\left(\mathbf{M} \times \frac{d\mathbf{M}}{dt}\right). \tag{2.9}$$

This equation states that the change in magnetization is perpendicular to the macrospin and to the applied magnetic field. With a (sinusoidal) driving force perpendicular to the external magnetic field, a precessional motion of the macrospin takes place. The second term describes the damping with Gilbert damping parameter α (see Sec. 2.5), which brings the system back to the "untilted" state. The LLG is often solved [HH18] by splitting the magnetization (as well as the external field) into a static component along the z-axis and a time-dependent component $\mathbf{m}(t)$ ($\mathbf{h}(t)$) in the xy-plane.

$$\mathbf{M} = M_0\hat{z} + \mathbf{m}e^{i\omega t}, \tag{2.10}$$
$$\mathbf{H} = H_0\hat{z} + \mathbf{h}e^{i\omega t}, \tag{2.11}$$

with angular drive frequency ω given by the external rf field $\mathbf{h}(t)$. One can then calculated the linear response by assuming circularly polarized fields m^+, h^+ [2] leading to

$$m^+ = \frac{-\omega_m}{\omega - \omega_r + i\alpha\omega}h^+, \tag{2.12}$$

with $\omega_m = \gamma M_0$. These equations play a key role in understanding the coupling mechanism of the CMP from an electromagnetic viewpoint (Sec. 2.3.2) and again show the analogy of the FMR to a driven harmonic oscillator.

2.3 Coupling Models

Over the last years, three different models have helped to unravel the behavior of the CMP and its physical coupling mechanisms. A review is given in Ref. [HH18], which is roughly followed in this section. The three coupling models are:

---

[2] In case of a non-spherical sample geometry, one has to account for the specific geometry and use elliptical fields.
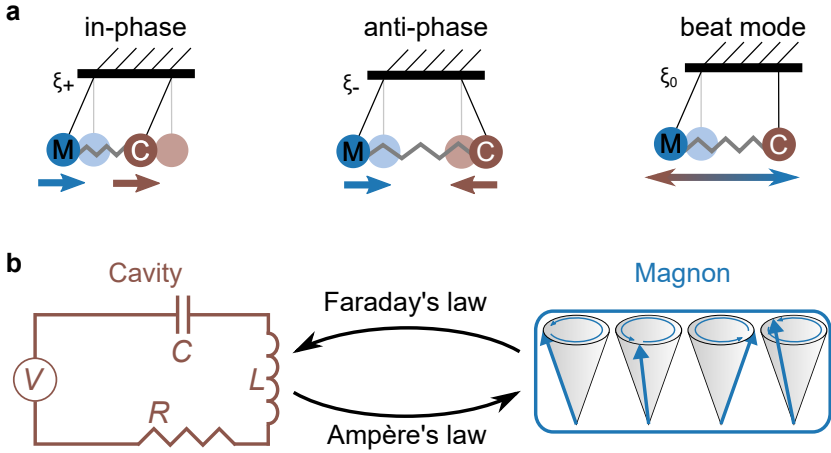
Figure 2.3: CMP modes and schematic depiction of the CMP coupling mechanism. Panel **a** shows the coupled pendula representation of the different CMP modes, adapted from Ref.[Wol+20]. **b** Explanation of the CMP coupling mechanism from an electromagnetic viewpoint: The cavity current excites the spin waves in the magnonic medium via Ampère's law. Then according to Faraday's law the changing magnetization of the magnons acts as a back action to the cavity inducing a voltage drop [Bai+15].

- the simple picture of two coupled oscillators, which gives an intuitive understanding of the CMP behavior and will be drawn upon in Ch. 5 for explanations of the CMP's time evolution;

- an electrodynamic model, revealing the underlying coupling mechanisms, and showing the origin of a phase correlation between the two subsystems,

- a quantum model describing the CMP in second quantization, practical for hybrid quantum systems comprising qubits and magnons as well as for the input-output formalism employed in Sec. 3.3.

In the following, due to its unique usefulness every model will be discussed in more detail.

2.3.1 Coupled Oscillators

In the previous sections, the RLC resonator as well as the dynamics of the Kittel mode were described by the equation of harmonic oscillators. The intuitive way to model a coupling of these two systems can thus be similar to two coupled

oscillator [Bai+15] ("mechanical pendula") with constant coupling strength g and the following system of equations:

$$\begin{pmatrix} \omega - \tilde{\omega}_c & g \\ g & \omega - \tilde{\omega}_r \end{pmatrix} \begin{pmatrix} h \\ m \end{pmatrix} = 0. \tag{2.13}$$

The complex resonance-frequencies for cavity and magnon, $\tilde{\omega}_c$ and $\tilde{\omega}_r$, already include the decay rates κ_c, κ_r, i.e., damping terms, $\tilde{\omega}_c = \omega_c - i\kappa_c = \omega_c - i\beta\omega_c$ and $\tilde{\omega}_r = \omega_r - i\kappa_r = \omega_r - i\alpha\omega_c$. The above equation is also already simplified by the rotating wave approximation (RWA), i.e., neglecting fast oscillating terms, making the system linear in ω instead of quadratic. Since the right hand side of Eq. (2.13) is zero, it is valid for the case of free evolution, i.e., coupling to the environment is neglected. The coupled or driven case, however, can be easily modeled by replacing the right hand side with a harmonic drive force of the form $A = \exp(i\omega t)$ for the sub-system under driving. The big advantage of this simple picture is the intuitive understanding of the CMP and the right predictions for the behavior close to resonance. The eigenfrequencies of the coupled system are then given by diagonalization of Eq. (2.13)

$$\omega_\pm = \frac{1}{2}\left(\tilde{\omega}_c + \tilde{\omega}_r \pm \sqrt{(\tilde{\omega}_r - \tilde{\omega}_c)^2 + g^2}\right). \tag{2.14}$$

This equation already yields the characteristic avoided level crossing of the two normal mode frequencies (for $g > \kappa_c, \kappa_r$ see, Sec. 2.4).

From this picture, it is also clear that the eigenmodes correspond to in-phase and anti-phase oscillation of the two sub-systems. Exciting only one system with a short pulse leads to the beat mode, where energy is exchanged periodically (see Fig. 2.3a). We can use Eq. (2.13) to calculate the field dependent mixing ratio of the normal modes, i.e., the ratio of photon and magnon excitation with respect to the detuning, and find the following expressions for the normalized eigenmodes [HH18]:

$$\xi_{1,2} = \frac{1}{\sqrt{2\Omega}}\begin{pmatrix} \pm\sqrt{\Omega \mp \Delta} \\ \sqrt{\Omega \pm \Delta} \end{pmatrix}, \tag{2.15}$$

with $\Omega = \sqrt{(\omega_r - \omega_c)^2 + 4g^2}$ and $\Delta = \omega_r - \omega_c$. Importantly, the linewidth evolution of the CMP follows this mixing ratio, i.e., if cavity and magnon system posses different decay rates, they too hybridize.

Although the linewidth mixing is determined by the detuning, we can take inspiration from the coupled pendula system and realize that the mode composition of the CMP can be changed by simultaneous pulsed drive tones. This topic will be discussed and demonstrated experimentally in Ch. 5.

2.3.2 Electrodynamic Model - Origin of Phase Correlation

The coupled oscillator models predicts the behavior of the CMP well. However, it does not explain the physical origin of the coupling mechanism. This origin is revealed by the electrodynamic model, which has been developed by Bai *et al.* [Bai+15]. Considering the differential equation for an RLC circuit (Eq. 2.1) as well as the LLG (Eq. 2.9), we can use Maxwell's laws to connect these two equations. In essence, the oscillating voltage in the cavity produces a current j generating a magnetic rf-field according to Ampère's law. This rf-field then drives the spin waves (magnon) of the magnetic material. Now due to Faraday's induction law, the changing magnetization m of the magnon produces an electric field, which drives the cavity in return. Thus, we have a closed cycle between the two subsystems and can see how they are coupled. Figure 2.3b visualizes the coupling mechanism. Merging the just enumerated equations together, we find the following coupled systems of equations:

$$\begin{pmatrix} \omega^2 - \omega_c^2 + 2i\beta\omega_c\omega & i\omega^2 K_c \\ -i\omega_m K_m & \omega - \omega_r + i\alpha\omega \end{pmatrix} \begin{pmatrix} j \\ m \end{pmatrix} = 0. \qquad (2.16)$$

with coupling constants K_m and K_c. Moreover these equations give rise to a phase correlation between the actual physical quantities, cavity current j and magnon magnetization m. This phase correlation is similar to the intuitive picture of the coupled oscillators with the in-phase and anti-phase eigenmode. Again, applying the RWA simplifies Eq. (2.16) to Eq. (2.13), emphasizing the similarity of the two models.

2.3.3 Quantum Model

According to Sec. 2.2, we can treat the spin wave excitations in the language of quantum mechanics. The most general Hamiltonian describing the interaction of N spins (two-level systems) with photons of a single cavity mode in quantum optics is the Dicke model [Dic54]. In the following, we will treat the FMR as a single macrospin, which allows us to neglect this distinction between one and N spins and leads to the quantum Rabi model [Rab37]. The Hamiltonian reads:

$$\mathcal{H}_{QR} = \hbar\omega_c a^\dagger a + \hbar\omega_r m^\dagger m + \hbar g \left(a + a^\dagger \right) \left(m + m^\dagger \right). \qquad (2.17)$$

Here, $a^\dagger, a$ are the bosonic creation and annihilation operators of the cavity. The original quantum Rabi model uses the spin raising and lowering operators σ^+, σ^-. However the Kittel-mode is not a two-level system, but a harmonic oscillator,

i.e., infinite energy levels with equal spacing, and hence $m^\dagger m$ are the bosonic ladder operators for magnons, as defined before. The use of bosonic operators instead of spin operators leads to subtle differences, e.g., the dispersive shift of the Kittel-mode does not depend on the photon number in the cavity.

We can simplify Eq. (2.17) by applying the RWA again, which leads to the well-known Jaynes Cummings Hamiltonian [JC63] (again with bosonic operators):

$$\mathcal{H}_{\mathrm{JC}} = \hbar\omega_c a^\dagger a + \hbar\omega_r m^\dagger m + \hbar g \left(a m^\dagger + a^\dagger m \right). \tag{2.18}$$

From this Hamiltonian, we can directly see the exchange of excitations between the two modes and the similarity to Eq. (2.13). This coupling picture is especially useful in the few magnon limit and subsequently in the coupling of magnons, resonator and qubit [Tab+16; Lac+17; Lac+20; Pfi19; Sch20]. However the model is not confined to these cases. Although originating from quantum mechanics, the extracted results have been employed for room temperature experiments, e.g, a magnon gradient memory [Zha+15] and observation of exceptional points [Zha+17]. Moreover, adding a non-hermitian term to Eq. (2.18) allows for the description of the so-called dissipative coupling in CMPs, as we will see in Ch. 4, and which was demonstrated in Refs. [Har+18; WH20; Bov+20], for instance. Furthermore, one can employ the above Hamiltonian together with the input-output formalism [Cle+10] to calculate the experimentally accessible dispersion spectra of CMPs [HH18] (see Sec. 3.3.1).

2.4 Coupling regimes

In the previous sections, we have discussed the coupling mechanism of the CMP but not the interplay of coupling strength g versus decay rates κ_c, κ_r and resonance frequencies ω_r, ω_c. Depending on the ratios of these quantities, one distinguishes several coupling regimes [Koc+19], with different properties. The following overview aims for a basic understanding of these regimes to prepare experiments accordingly to the given requirements.

Weak Coupling

In the weak coupling (WC) regime, the loss rate is greater than the coupling strength $\kappa_c, \kappa_r > g$, which means that an excitation in one system does not live long enough to interact with its counter-system. Therefore, no coherent energy exchange is possible. Although efficient single and entangled photon emission

could be shown for semiconducting devices [Shi07] in this regime, the WC has played a minor role for the CMP.

Strong Coupling

The hallmark of the strong coupling (SC) regime is the avoided level crossing and was first observed by Huebl *et al.* [Hue+13].The SC manifests itself if $g > \kappa_c, \kappa_r$. In the SC, the two normal modes are separated completely with a maximum gap of $2g$ (compare (Eq. 2.14)) and a coherent energy exchange takes place. At the crossing point ($\omega_r = \omega_c$) the complete energy is periodically transferred from one system to another, which is visible in the time domain and has been titled magnon-Rabi oscillations [Zha+14]. Here, the coupled oscillator analogy is the previously mentioned beat mode. The SC plays the fundamental role for quantum information processing and allows for the dispersive readout of superconducting qubits [Wal+04; Bla+04], for example. It has so far been the most studied regime for the CMP and is the foundation for the presented results in Ch. 4 and Ch. 5.

Ultra Strong Coupling

For the previous two regimes, the coupling strength g was compared to the decay rates κ_c, κ_r. For the ultra strong coupling (USC) regime, however, the quotient of g over $\omega_c = \omega_r$ is the important quantity. The USC is reached if $0.1\,\omega_c < g < 1.0\,\omega_c$. In this regime, the RWA can no longer be applied, counter-rotating terms in the Hamiltonian need to be considered, and the quantum Rabi- / Dicke-, instead of the Jaynes Cummings-, model must be employed. The quantum Rabi model does not preserve the particle number and predicts a ground state population, for instance. The USC promises application for fast and protected quantum information processing [Koc+19]. It has already been demonstrated for the CMP several times [Zha+14; Gor+14; KGT16; Bou+16; Flo+19]. Yet, recall, that the CMP (based on the uniform mode) consists of two harmonic systems. Thus, one has to introduce additional anharmonicity to garner all effects predicted by the quantum Rabi model.

Deep Strong Coupling

The deep strong coupling regime (DSC) completes the list. The coupling strength exceeds the resonance frequency $g \gtrsim \omega_c$. The DSC has so far been demonstrated with superconducting flux qubits [Yos+17; Yos+18] and Landau polaritons [Bay+17],

exhibiting light matter decoupling, for example. It can be argued that, without additional tricks, the CMP cannot be pushed into the DSC because of its classical Hookian-like coupling [Sud+12]. Here, a stronger coupling entails a renormalization of ω_c, ω_r, which themselves then include the coupling strength, making the condition above impossible to reach.

2.5 Spin Wave Coherence in YIG

Improving device performance requires a thorough understanding of the occurring loss and decoherence mechanisms. Despite exhibiting the highest life time of spin waves, Yttrium-Iron-Garnet (YIG), the most prominent material, still lags magnitudes behind the excitation life time of superconducting devices. Due to the variety of possible magnon applications, a study of these processes is important at room temperature as well as at low temperature. After introducing YIG, an overview of the main loss mechanisms above 1 K is given, and then the focus is set on two-level systems (TLS), which are possible suspects for loss at mK-temperatures and therefore of special interest for CMPs coupled to quantum devices.

2.5.1 Properties of YIG

YIG is a complex and artificially fabricated material, exhibiting a crystal structure with a unit cell containing four formula units of $Y_3Fe_2^{3+}Fe_3^{3+}O_{12}$, [CKL93], resulting in two sub-lattices and 80 atoms per cell. Regardless of this complexity, it has become the material of choice for magnonics. The refined fabrication process [SCH10] due to industrial applications in microwave devices, such as circulators, makes the material easily available for research. Moreover, YIG's high Curie temperature of $T_c = 560\,K$, allows for room temperature- as well as low-temperature experiments. And last but not least, YIG offers the lowest spin wave damping with a life time of several 100 ns at room temperature, because of the absence of conduction electrons [SCH10]. This lifetime corresponds to a mean free path of a few cm, permitting information transport based on spin waves. Nevertheless the loss mechanisms at mK temperatures are still not yet understood. There, the complexity of the material demands more research about the physical realization of loss channels. To complete this short summary and avoid any confusion, we also note that YIG is a ferrimagnetic material but often simply considered as a ferromagnet in the low energy range [Tab+16].

2.5.2 Loss Mechanisms above 1 K

A brief summary giving a background for magnetic losses in YIG is presented in the following. The loss mechanism are often simply hidden inside the phenomenological Gilbert damping parameter a, which is also assumed to be frequency independent. This however is often not the case. More detailed information can be found in recent linewidth investigations, e.g., Refs. [Mai+17; Bov+18]. The authors measured magnon modes over a broad temperature range from 300 K to 4 K and attributed distinct loss mechanisms to changes in the linewidth.

Intrinsic relaxation can be described by the Kasuya-Le Craw mechanisms [KL61], which are scattering processes between magnons and phonons. An alternative explanation was given by Cherepanov, where the uniform mode interacts with optical magnons [CKL93]. These processes decrease with decreasing temperature. For highly pure YIG at 4 K, its intrinsic linewidth was found to be 42 kHz [SLL61]. However in most measurements, other processes play dominant roles below 100 K.

Temperature peak processes arise due to scattering with slowly and rapidly decaying rare earth impurities and show a distinct peak at a certain temperature between 1 K to 100 K.

Two magnon surface scattering describes the scattering of the uniform mode with surface pits. This scatter process creates a new magnon with the same frequency but with wave vector $k \neq 0$. It can be mitigated by polishing the surface. [SLK61; Nem64]

Radiation damping can be a problem at any temperature. The changing magnetic field of the spin waves excite eddy currents in metallic parts, i.e., the strip line underneath. According to Lenz's law, the currents then counteract the spin wave precession and hence lead to energy loss. Radiation damping is especially problematic for thin films but can be mitigated by wide strip lines and an increased distance to the sample [MK15; Kos16].

2.5.3 Two-Level Systems (TLS)

Going into the mK region, we now consider TLS, which have been found to strongly hamper the quality of (superconducting) quantum devices. In the last years, they have been suspected to cause loss for magnons as well. This presumption is based on the typical linewidth increase towards low powers and temperatures. [Tab+14; Pfi+19; Kos+19]
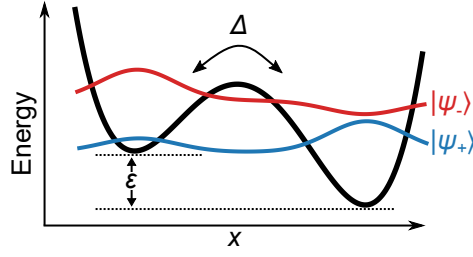
Figure 2.4: Potential of the standard tunneling model for two-level systems (TLS). Two harmonic potentials hybridize leading to a double well potential with asymmetry energy ϵ and tunnel barrier Δ. This hybridization also results in a symmetric and anti-symmetric wave function describing the probability density of a charged particle mostly living in either well. The two states $|\psi_-\rangle$ and $|\psi_+\rangle$ have an energy difference of $E = \sqrt{\Delta^2 + \epsilon^2}$. The standard tunneling model assumes the two hybridizing potentials to be in the spatial domain. Since several TLS realizations exist, here the x-axis is chosen to be generic. Schematic adapted from [MCL19].

The concept of TLS was first applied to amorphous solids with the goal of explaining their thermal and acoustic properties in the form of the standard tunneling model (STM) [Phi72; AHV72]. An excellent overview of TLS and their effect on quantum devices is given by Müller *et al.* [MCL19]. I will now review the important points to understand the linewidth contribution of TLS to a resonating system.

In the STM, two atomic sites, each with a harmonic energy potential, hybridize, which leads to the well-known double well potential (see Fig. 2.4). The two potential wells can have an asymmetry energy ϵ and the energy required to overcome the potential barrier by tunneling is denoted as Δ. In the basis of the lowest confined states of each well, $|L\rangle, |R\rangle$, the Hamiltonian governing the system can be written as:

$$\mathcal{H}_{\text{STM}} = \frac{1}{2} \begin{pmatrix} \epsilon & \Delta \\ \Delta & -\epsilon \end{pmatrix}. \tag{2.19}$$

Diagonalizing the Hamiltonian gives the two eigenstates

$$|\Psi_+\rangle = \sin\left(\frac{\theta}{2}\right)|L\rangle + \cos\left(\frac{\theta}{2}\right)|R\rangle, \tag{2.20}$$

$$|\Psi_-\rangle = \cos\left(\frac{\theta}{2}\right)|L\rangle - \sin\left(\frac{\theta}{2}\right)|R\rangle, \tag{2.21}$$

with mixing angle $\theta = \Delta/\epsilon$, and the energy difference between them is calculated to

$$E = E_- - E_+ = \sqrt{\Delta^2 + \epsilon^2}. \tag{2.22}$$

17

Let us assume a charged particle as possible TLS realization [MCL19]. This particle mainly lives in one potential well (Eq. 2.21, depending on the mixing angle) but can tunnel into the other one. Because of this movement, we can associate electric dipole moments with TLS and the electric field of a resonator, for example, can then couple to TLS' dipole moments. Because of this coupling, the resonator can lose energy to a bath of TLS, resulting in an increased resonator linewidth [Phi87; Wan+09]. Such energy transfer, however, can only happen if there is a difference in the occupation number between the two TLS states $\Delta n = n_+ - n_-$ [EH05], which is affected by temperature and drive power. We will now quantify these effects with respect to the resonance linewidth.

Temperature

Assuming a Boltzmann distribution, the difference in occupation number is given by

$$\kappa_{\text{TLS}} \propto n_+ - n_- = \tanh\left(\frac{\hbar\omega_{\text{c}}}{k_{\text{B}}T}\right), \tag{2.23}$$

where the TLS energy difference equals the resonator frequency due to resonant absorption. Increasing the temperature leads to a smaller occupation number and for GHz resonance frequencies, the equilibrium is reached in the few Kelvin region, making the effect of TLS negligible. Bringing the TLS bath into equilibrium is often also called "saturating the TLS".

Drive Fields

Driving the TLS strongly (via the resonator) equalizes the occupation number as well. If the Rabi rate, the rate with which the state of the TLS changes, exceeds the TLS' coherence rate, the TLS bath will be in an equal superposition of the two states.

Employing the analogy of a TLS to a spin-particle in a magnetic field plus an interaction term leads to the well-known Bloch equations [Blo46; Gao08]. From which in turn, the power dependence of the linewidth contribution can be calculated as

$$\kappa = \kappa_{0,\text{TLS}} \frac{\tanh\left(\frac{\hbar\omega}{k_{\text{B}}T}\right)}{\sqrt{1 + P/P_{\text{c}}}} + \kappa_{\text{offs}}. \tag{2.24}$$

The term in the square root containing the critical power P_{c} is defined via $P/P_{\text{c}} = \Omega_{\text{R}}^2/(\Gamma_1\Gamma_2)$, with Ω_{R} as Rabi rate and inverse life-time, decoherence rate Γ_1, Γ_2,

respectively [Gao08]. The temperature dependence of Eq. (2.23) has been incorporated as well. $\kappa_{0,\text{TLS}}$ is the proportionality constant of the TLS contribution and κ_{offs} the linewidth contribution independent of power and temperature.

Linewidth data for the uniform FMR mode at mK temperatures were found to follow Eq. (2.24). In Refs. [Tab+14; Pfi+19] a CMP, with a YIG sphere inside a copper cavity, was probed and the magnon linewidth was extracted from fits to input-output theory. Kosen *et al.* [Kos+19] examined a YIG thin film on a transmission line.

However, the physical realization of TLS in YIG has not yet been explained. It is also noted that drive powers far exceeding the single photon limit are required to saturate TLS in YIG, which is in stark contrast to superconducting resonators. This would either suggest very short lifetimes of the TLS or a considerable weaker coupling to them. Moreover a possible coupling mechanism of magnons to TLS has not yet been described either. The associated electric dipole moment in the STM would require electric fields for a capacitive coupling, which is contrary to the magnetic fields of spin waves, giving an inductive coupling. A possible solution could be magnetic impurities, which has been proposed for SQUIDS and superconducting qubits. [KDC07]

Frequency noise of TLS

TLS not only influence device quality negatively due to energy loss but also cause frequency fluctuations in superconducting resonators and qubits leading to bad coherence times. In the picture of the Jaynes-Cummings Hamiltonian, one can see that the resonance frequency of the resonator changes with the state of the TLS. Hence, random occupations of the TLS lead to random fluctuations of the resonance frequency [MCL19; Gao+07]. Averaging over many weakly coupled TLS gives the ubiquitous and infamous $1/f$ noise [Pal+14]. From the temperature and power dependence of the resonance fluctuations, information can be gathered about the TLS properties [Bur+19].

The TLS-like linewidth increase of magnons would suggest that their resonance frequency should show $1/f$ noise as well. However, we will see in Ch. 6 that the dominant magnon noise shows a distinctly different scaling with frequency.

3 Probing the CMP with Microwave Tones

3.1 Introduction and S-Matrix

Now, after having discussed the physical mechanisms underlying the CMP in Ch. 2, we also have to experimentally probe this quasi-particle. The method of choice are microwave reflection and absorption measurements. If the probe frequency of the incoming microwave signal ω_p is close to the resonance frequency ω_c of the cavity (or ω_r of the FMR), the system will absorb energy, store it and partially re-emit it. By coupling the CMP via a microwave transmission line to a vector network analyzer (VNA), we can measure the ratio of reflected/out-coming voltage (V^{out}) to in-going voltage (V^{in}), which provide information about the CMP's physical properties. Such a voltage ratio is denoted as S-Matrix element or scattering parameter [Poz12]

$$S_{ij} = \frac{V_i^{\text{out}}}{V_j^{\text{in}}}.\tag{3.1}$$

The indices i, j denote the ports where the voltages are measured; voltages at all other ports are set to zero. Having for example a two-port network, one can build a 2x2 matrix out of S_{ij}

$$\begin{pmatrix} V_1^{\text{out}} \\ V_2^{\text{out}} \end{pmatrix} = \begin{pmatrix} S_{11} & S_{12} \\ S_{21} & S_{22} \end{pmatrix} \begin{pmatrix} V_1^{\text{in}} \\ V_2^{\text{in}} \end{pmatrix}.\tag{3.2}$$

The scattering parameter is a complex quantity, and often stated in the form of amplitude, $\left| S_{ij} \right|$, and phase, $\arg S_{ij}$, which denotes the phase difference between the in- and outgoing voltage. It should not be confused with the phase-offset of an oscillator with respect to the driving signal. Furthermore a reduction in amplitude can occur because of loss in the system as well as destructive interference of the involved electrical signals.

a   **b**   **c**
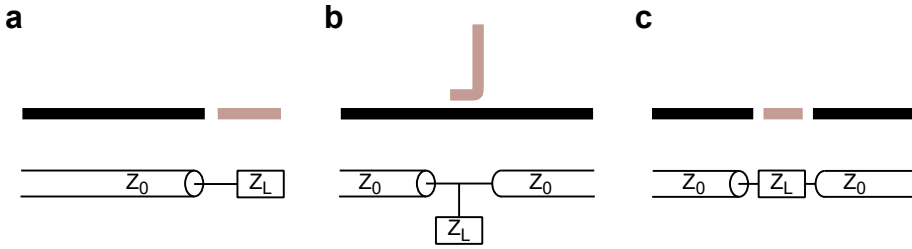
Figure 3.1: Different coupling configurations of microwave resonators, exemplarily shown with transmission line resonators and their schematic circuit diagram underneath. Here, Z_L denotes the load of the coupled resonator **a** Single-port/reflection configuration: the resonator terminates the transmission line. **b** Notch-type configuration: the resonator is placed next to the transmission line. **c** Inline configuration: the signal is transmitted trough the resonator.

Our goal is now to link the S-matrix to the important CMP properties, such as resonance frequencies, decay rates and coupling strength. As the CMP is typically probed only via its cavity, we will first derive the S-Matrix elements for a single resonator, but for different coupling configurations to the transmission line, followed by the S-Matrix element for coupled systems, such as the CMP. Examples of dispersion spectra for different coupling regimes and a short explanation of the standard spectroscopic measurement setup conclude this chapter.

3.2 Scattering Elements of a Single Resonator

To obtain the desired relation between the physical quantities of a single resonator and the S-parameters, one can either follow an impedance based approach [Bra18; Sch07; Maz04] or employ the input-output formalism [Cle+10]. Here, we will first apply the impedance based approach, following the cited references, and use the latter one for the coupled system in Sec. 3.3.

Depending on the geometry resonators are arranged with respect to the transmission line, one distinguishes the following configurations: single port (reflection), notch-type, and inline (see Fig. 3.1). The discussion will be confined to the first two configurations, which are employed in this work.

Single-Port Resonator (Reflection Type)

In radio frequency (rf) applications and measurements, microwave signals travel along a transmission line, e.g., coaxial cables, microstrips, or coplanar waveguides,

designed with a standard impedance of $Z_0 = 50\,\Omega$. The impedance is defined by the ratio of voltage V to current I.Transitioning from one medium into the other, e.g., from a transmission line into a resonator, electromagnetic waves may be reflected depending on the impedance mismatch between two media. Already considering reflections, i.e., waves propagating in opposite directions, we can write down an expression for the load impedance Z_L terminating a transmission line:

$$Z_L = \frac{V}{I} = \frac{V^{\text{out}} + V^{\text{in}}}{V^{\text{in}} - V^{\text{out}}} Z_0. \tag{3.3}$$

Here, we have employed to Kirchhoff's laws stating that one has to add voltages and subtract currents of the incoming and outgoing plane waves. Moreover, this equation is only valid directly at the interface, since superpositions of plane waves lead to a spatially varying impedance [Bra18]. Rearranging Eq. (3.3), we can calculate the reflection coefficient (often denoted as Γ), which equals the scattering parameter S_{11}:

$$S_{11} = \frac{V^{\text{out}}}{V^{\text{in}}} = \frac{Z_L - Z_0}{Z_L + Z_0}. \tag{3.4}$$

Equation. (3.4) connects the scattering matrix element to the impedance of a load Z_L. Such a configuration corresponds to the single port or reflection-type resonator. In the next step, Z_L is linked to the resonator's quantities, i.e., resonance frequency, coupling-, and internal quality factor. For any lossy resonating system, one can define a quality factor (Q-factor), by the ratio of total stored energy E_{tot} and energy loss per cycle P_{loss}

$$Q = \omega \frac{E_{\text{tot}}}{P_{\text{loss}}}. \tag{3.5}$$

For microwave resonators, the overall Q-factor is denoted as loaded factor Q_L, which can be obtained by inversely adding the internal quality factor Q_i and coupling quality factor Q_c, describing energy dissipation and emission into the transmission line, respectively:

$$Q_L^{-1} = Q_i^{-1} + Q_c^{-1}. \tag{3.6}$$

Following [Poz12; Bra18; Maz04; Sch07], we can express the Q-factors of a reflection type resonator capacitively coupled to the transmission line by

$$Q_i = \frac{\omega_0 L}{R}, \tag{3.7}$$

$$Q_c = \frac{\pi}{2 Z_0 Z_R \omega^2 C_c^2}. \tag{3.8}$$

The first equation is simply derived from the RLC model and the second equation describes the energy transfer over the coupling capacitance C_c. Here, Z_R describes the characteristic impedance of the resonator defined by material and design parameters. In this derivation, it is only used as an auxiliary quantity in our goal of expressing the scattering parameter through the Q-factors.

Now, we exemplarily consider an open-ended $l = \lambda/2$ transmission line resonator as depicted in Fig. 3.1a to find an expression [Bra18; Poz12] for the load impedance:

$$Z_L(\omega) = \frac{1}{i\omega C_c} + \frac{Z_R}{\tan vl}, \tag{3.9}$$

with imaginary propagation constant v accounting for the spatial variance of the superpositioned electric fields. It is evident that the length of the resonator changes the impedance with respect to ω due to the resonance condition of such a resonator. Close to resonance and requesting $\Im Z_L = 0$, the above equation can be simplified by a Taylor expansion to

$$Z_L(\omega) = Z_R \left(\frac{\pi}{2Q_i Z_R^2 \omega^2 C_c^2} + i\frac{\pi(\omega - \omega_0)}{\omega_0 Z_R^2 \omega^2 C_c^2} \right). \tag{3.10}$$

Using the expressions Eq. (3.7) and Eq. (3.8) for Q_i and Q_c as well as plugging Eq. (3.10) into Eq. (3.4) yields the desired expression of the scattering parameter for a reflection type resonator

$$S_{11} = 1 - \frac{2Q_L/Q_c}{1 + 2iQ_L\frac{\omega - \omega_0}{\omega_0}}. \tag{3.11}$$

This equation, despite its derivation for a capacitively coupled $\lambda/2$, is actually independent of the resonator type because the underlying physics is absorbed in the generic quality factors. Employing Eq. (3.11), we can calculate the squared amplitude $|S_{11}|^2$, corresponding to the power ratio, and the phase difference $\arg S_{11}$ of the outgoing and incoming signal.

$$|S_{11}|^2 = 1 - \frac{1 - (2Q_L - Q_c)^2/Q_c^2}{1 + 4Q_L^2\left(\frac{\omega - \omega_0}{\omega_0}\right)^2}, \tag{3.12}$$

$$\arg S_{11} = -\arctan\left(2Q_L\frac{\omega - \omega_0}{\omega_0}\right) - \arctan\left(2\frac{Q_L Q_c}{2Q_L - Q_c}\frac{\omega - \omega_0}{\omega_0}\right). \tag{3.13}$$

Comparing Eq. (3.12) to the (unnormalized) Lorentzian distribution $f(x) = a/(1 + 4(x - x_0)^2/\gamma^2) + c$, with a, c as scaling parameter and offset, we can identify the full

width at half maximum (FWHM) of the distribution as $\gamma = \omega_0/Q_L$. The Lorentzian function is linked to an exponential decay with decay rate $\kappa = \gamma/2$ via Fourier transformation. Hence, the inverse of the *half* width at half maximum (HWHM) specifies the lifetime of a resonator.

Notch-type Configuration

We will now switch from the reflection type resonator to the notch-type configuration, depicted in Fig. 3.1b. Here, the resonator does not terminate the transmission line, but is located next to it. This configuration is of special interest for this work because it not only describes LC-resonators but is also valid for the coupling to spin waves excited in a YIG sphere located over the transmission line.

For the notch-type configuration, we have to consider that the resonator sees only half the transmission line impedance $Z_0/2$ due to the parallel network. Adjusting the expression for the coupling Q-factor by the new transmission line impedance, Eq. (3.8) leads to the S_{21} scattering element of the notch-type configuration[Bra18]

$$S_{21} = 1 - \frac{Q_L/Q_c}{1 + 2iQ_L\frac{\omega-\omega_0}{\omega_0}}. \tag{3.14}$$

Amplitude squared and phase of the matrix element read

$$|S_{11}|^2 = 1 - \frac{1 - (Q_L - Q_c)^2/Q_c^2}{1 + 4Q_L^2\left(\frac{\omega-\omega_0}{\omega_0}\right)^2}, \tag{3.15}$$

$$\arg S_{11} = -\arctan\left(2Q_L\frac{\omega - \omega_0}{\omega_0}\right) - \arctan\left(2\frac{Q_L Q_c}{Q_L - Q_c}\frac{\omega - \omega_0}{\omega_0}\right). \tag{3.16}$$

The equations for the two discussed resonator configurations only differ by a factor of 2 in the numerator. This factor, however, leads to distinctly different responses depending on the coupling regimes of the resonators, i.e., ratio of the Q-factors, as we will see in the following section.

Comparison of the Single-Port and Notch-Type Scattering Elements

Depending on the ratio of Q_i and Q_c, one differentiates the following three coupling regimes between resonator and transmission line:

- under-coupled, $Q_i < Q_c$, energy loss mainly inside the resonator
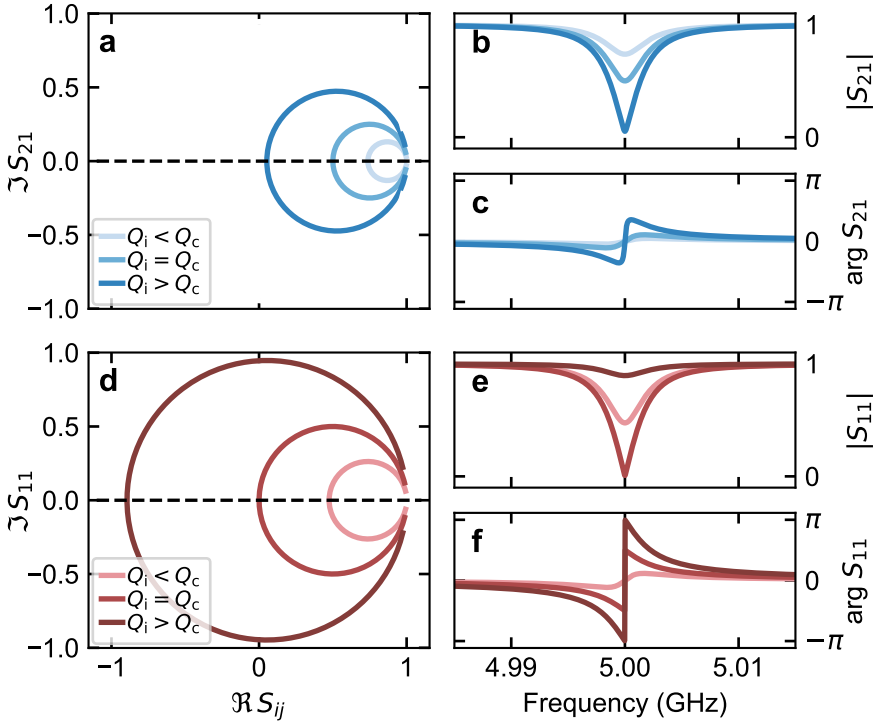
Figure 3.2: Scattering elements of notch- and reflection type resonators for different coupling regimes. Panels **a** to **c** display the S_{21} parameter in the complex plane, the amplitude signal and the phase signal respectively for the under-coupled ($Q_i < Q_c$), critically-coupled ($Q_i = Q_c$) and over-coupled ($Q_i > Q_c$) case of a notch-type configuration. Panels **d** to **f** show the S_{11} parameter of a reflection type configuration with the same Q-factors as in the panels above.

- critically-coupled, $Q_i = Q_c$, *equal* energy loss in resonator and energy transfer to transmission line,

- over-coupled, $Q_i > Q_c$, energy mainly transferred to the transmission line.

Depending on the application, a specific coupling regime may prove advantageous. Knowing how the two resonator configurations respond differently depending on the coupling regime can help us quickly interpret the measurement results. Figure 3.2 shows a comparison of the microwave response of the two discussed resonator types. Panel a and d show the responses of the respective resonator in the complex plane. The resonators trace out a circle with the resonance point as the intersection with the real axis. The diameter increases with the ratio of Q_i/Q_c for both configurations. However, the circle of a notch-type resonator always remains on the positive side of the real axis due to the additional factor of two in the

scattering element. In contrast, the reflection type resonator upon reaching the over-coupled regime covers all quadrants. Bearing these behaviors in mind, we can understand the amplitude and phase response for the different configurations and coupling regimes.

For the under-coupled cases the amplitude and phase signal is weak due to the small circle diameter and high distance from the origin; only little energy is exchanged with the resonator.

The critically-coupled notch type shows an amplitude signal of 0.5 (6 dB); half of the energy is lost inside the resonator. We can also recognize that the strongly over-coupled notch configuration corresponds to the critically coupled reflection configuration. Here, the amplitude signal shows the deepest dip, as the circle touches the origin. For critically coupled reflection-type resonators, the energy transfer equals the internal loss rate and therefore all photons are dissipated inside the resonator. For the strongly over-coupled notch-type resonator, the signal interferes destructively along the transmission line and all energy is reflected back to port one. The phase signal jumps from $-\pi/2$ to $\pi/2$.

In contrast, the strongly over-coupled reflection-type resonator has no dip in the amplitude signal. Due to the high Q_i, no energy is lost in the resonator, and the full signal is reflected after interaction. The resonance circle thus has the maximum diameter and all information about the resonator's properties is contained in the phase signal, which undergoes a phase jump of 2π when transitioning the resonance frequency.

As a last word of caution, impedance mismatches in the microwave lines rotate the circle around its center, thereby shifting the resonance point off of the real axis [Kha+12; Pro+15]. Consequently, the phase and amplitude signal do no longer follow a clean Lorentzian or arctan function. A circle fit algorithm [Pro+15; PA98; Gao08] nevertheless provides a robust way to extract the physical properties even under these experimental imperfections.

3.3 CMP Spectra

Up to now, we only discussed the spectroscopic response of a single resonator. Yet, the CMP is a system of coupled oscillators and thus our new goal is to derive the microwave response (S matrix element) of the coupled system.

3.3.1 Derivation of CMP Dispersion Spectra

For our derivation of the CMP spectrum, I will focus on the microwave resonator probed in the reflection configuration, which is used in this work. As before, the resulting expression for the *S* matrix element can easily be adjusted to the notch-type geometry by inserting a factor of 2 at the right place.

Short Descriptive Explanation

Following a crude but descriptive explanation given in Ref. [Sch20], we first rewrite Eq. (3.11) in terms of decay rates instead of Q-factors:

$$S_{11}(\omega) = 1 - \frac{2\kappa_c}{i(\omega_c - \omega) + \kappa_L}.$$
(3.17)

The coupled FMR mode acts as an additional loss channel inside the cavity, which we have to add to the loaded decay rate. From the perspective of the cavity, the FMR behaves like a second reflection type resonator, however coupled with g^2 instead of $2\kappa_c$, and with resonance frequency ω_r and internal magnon decay rate κ_r. g has to be squared because the rate (of energy loss) is the quantity of interest, instead of the reflection amplitude. This consideration then leads to

$$S_{11}(\omega) = 1 - \frac{2\kappa_c}{i(\omega_c - \omega) + \kappa_L + \frac{g^2}{i(\omega_r - \omega) + \kappa_r}}.$$
(3.18)

This equation is indeed the correct expression for a coupled oscillator system, despite our simple derivation. In the next section, we will see that a derivation based on the input-output formalism will confirm this result.

Input-Output Formalism

Although the CMP spectra can be derived purely classically, we use the quantum approach, given by the input output formalism, as explained in Refs. [Cle+10; HH18; Pfi19] and closely followed here. This formalism allows deriving scattering elements from the system's Hamiltonian and will provide an easy means to calculate the dispersion spectra of a two-tone driven CMP, see Ch. 4.

We must now quantum mechanically model an interaction between the CMP and its environment. A bath of harmonic oscillators represents the transmission line and the interaction is given by a complex coupling. One can then solve the CMP's equations of motions (EOM) and define useful wave packets representing

incoming and outgoing waves, where the ratio of these wave packets corresponds to the scattering matrix; connecting it to the desired physical quantities in the Hamiltonian.

Starting from the Jaynes-Cummings Hamiltonian for the CMP in Eq. (2.18)

$$\mathcal{H}_{\text{JC}} = \hbar\tilde{\omega}_c a^\dagger a + \hbar\tilde{\omega}_r m^\dagger m + \hbar g \left(a m^\dagger + a^\dagger m \right), \tag{3.19}$$

already accounting for internal losses by the complex eigen-frequencies, we model the transmission line as a bath of harmonic oscillators with ladder operators $c_q, c_q^\dagger$

$$\mathcal{H}_{\text{bath}} = \sum_q \hbar\omega_q c_q^\dagger c_q. \tag{3.20}$$

The interaction between transmission line and cavity part of the CMP is given by

$$\mathcal{H}_{\text{int}} = -i\hbar\lambda \sum_q \left(a^\dagger c_q - c_q^\dagger a \right). \tag{3.21}$$

Similar to the Jaynes Cummings Hamiltonian, photons between the systems are exchanged, describing the loss from the cavity into the transmission line. λ denotes the transition matrix element and is here already taken to be real and constant. The total Hamiltonian governing the system then reads

$$\mathcal{H}_{\text{tot}} = \mathcal{H}_{\text{JC}} + \mathcal{H}_{\text{bath}} + \mathcal{H}_{\text{int}}. \tag{3.22}$$

Recalling that scattering elements are ratios of electric fields, we rewrite S_{11} in terms of incoming and outgoing "wave packets", c_{in} and c_{out} to and from the cavity

$$S_{11} = \frac{c_{\text{out}}}{c_{\text{in}}}. \tag{3.23}$$

Thus, our objective is to find expressions for c_{in} and c_{out} that relate these operators first to $c, c^\dagger$ and thereby to a. One can employ the EOM for the operator a and c_q in the Heisenberg picture to describe the response of the CMP. These EOMs are given by

$$\dot{a} = -\frac{i}{\hbar}\left[a, \mathcal{H}_{\text{tot}} \right] = -\frac{i}{\hbar}\left[a, \mathcal{H}_{\text{JC}} \right] + \lambda \sum_q c_q. \tag{3.24}$$

and

$$\dot{c}_q = -\frac{i}{\hbar}\left[c_q, \mathcal{H}_{\text{tot}} \right] = -i\omega_q c_q + \lambda a. \tag{3.25}$$

The last equation is a linear system and can be solved exactly [Cle+10] by

$$c_q(t) = e^{-i\omega_q(t-t_0)} c_q(t_0) + \lambda \int_{t_0}^t e^{-i\omega_q(t-\tau)} a(\tau) d\tau. \tag{3.26}$$

Here $t_0 < t$ denotes a time before the wave packet has reached the cavity. Plugging Eq. (3.26) into Eq. (3.24) and multiplying one term by $\exp(-i\omega_c(t - \tau))\exp(+i\omega_c(t - \tau))$ yields for the last term

$$\lambda a = \lambda^2 \sum_q e^{i\omega_q(t-t_0)} c_q(t_0) + \lambda^2 \int_{t_0}^{t} e^{-i(\omega_q - \omega_c)(t-\tau)} e^{+i\omega_c(\tau-t)} a(\tau)\mathrm{d}\tau \tag{3.27}$$

Now, we use Fermi's Golden Rule

$$2\kappa(\omega_c) = 2\pi\lambda^2 \sum_q \delta(\omega_c - \omega_q), \tag{3.28}$$

which not only provides the needed relation between λ and the (coupling) decay rate but allows us simplify Eq. (3.27). Assuming a frequency independent coupling rate, we can rewrite Eq. (3.28) [Cle+10] to

$$\lambda^2 \sum_q e^{-i(\omega_q - \omega_c)(t-\tau)} = 2\kappa\delta(t - \tau). \tag{3.29}$$

This equation allows us to solve the integral in Eq. (3.27) and we obtain a simpler equation for the cavity EOM:

$$\dot{a} = -\frac{i}{\hbar}[a, \mathcal{H}_{\mathrm{JC}}] - \kappa a - \lambda \sum_q e^{-i\omega_q(t-t_0)} c_q(t_0). \tag{3.30}$$

Since the integration does not cover the delta function completely, but only up to t, a factor of $1/2$ comes into play. For the next step, we have to define our input mode, i.e., the incoming wave packet, in a useful way. Again, we employ Fermi's Golden Rule (with a constant density of states ρ and hence $2\kappa = 2\pi\lambda\rho$) which gives

$$c_{\mathrm{in}}(t) := \frac{1}{\sqrt{2\pi\rho}} \sum_q e^{-i\omega_q(t-t_0)} c_q(t_0) \tag{3.31}$$

and Eq. (3.30) becomes

$$\dot{a} = -\frac{i}{\hbar}[a, \mathcal{H}_{\mathrm{JC}}] - \frac{\kappa}{2}a - \sqrt{\kappa}c_{\mathrm{in}}(t). \tag{3.32}$$

This EOM is our desired equation. To calculate the S-matrix element, we also have to find a similar expression for c_{out}. The procedure is the same as above with the difference that we look at an outgoing wave packet and hence integrate from t to t_1, with t_1 in the distant future after the wave packet has been emitted. Due to the switched limits of the integral, this only leads to a sign change before a:

$$\dot{a} = -\frac{i}{\hbar} [a, \mathcal{H}_{JC}] + \frac{\kappa}{2} a - \sqrt{\kappa} c_{\text{out}}(t). \tag{3.33}$$

Subtracting Eq.(3.33) from Eq. (3.32) yields

$$c_{\text{out}}(t) = c_{\text{in}}(t) + \sqrt{\kappa} a(t), \tag{3.34}$$

which correctly states that the outgoing wave packet is a sum of the reflected wave packet and the photons leaking out of the cavity.

The last equation indicates that we need to solve the cavity EOM for a, which due to the coupling includes solving the magnon EOM as well. Employing Fourier transform we find:

$$\mathcal{F}(\dot{a}(t)) = -i\omega a(\omega) = (-i\omega_{c} - \kappa_{c})a(\omega) - igm(\omega) + \sqrt{2\kappa_{c}} c_{\text{in}}, \tag{3.35}$$
$$\mathcal{F}(\dot{m}(t)) = -i\omega m(\omega) = -i\omega_{r} m(\omega) - iga(\omega). \tag{3.36}$$

By plugging Eq. (3.36) into Eq. (3.35) and subsequently substituting the result into the Fourier transform of Eq. (3.34), we find the S-matrix element

$$S_{11}(\omega) = \frac{c_{\text{out}}(\omega)}{c_{\text{in}}(\omega)} = 1 - \frac{2\kappa_{c}}{i(\omega_{c} - \omega) + \kappa_{L} + \frac{g^{2}}{i(\omega_{r} - \omega) + \kappa_{r}}}. \tag{3.37}$$

In the final step, we substituted real eigenfrequencies plus imaginary decay rates for the complex eigenfrequencies, used $\kappa_{L} = \kappa_{c} + \kappa_{i}$. Furthermore, we multiplied the RHS by -1, which depends on convention [Gir14]. Indeed, this equation is equal to Eq. (3.18), the intuitively derived S-matrix element of the CMP.

3.3.2 Examples of Dispersion Spectra

Equipped with the equation giving us the reflection response of the CMP, we can analyze the interplay of coupling strength and decay rates. Figure 3.3a and b show the amplitude and phase response of a strongly coupled CMP ($g = 10\,\text{MHz} > \kappa_{L} = 4\,\text{MHz}, \kappa_{r} = 1\,\text{MHz}$). We can see that the eigenfrequencies are visible as dips in the amplitude and as jumps in the phase signal as expected for two resonators. Moreover, the hybridization of the linewidth is clearly visible in the amplitude plot. The narrower magnon dip becomes broader as the two frequencies approach each other until the linewidths of both branches are identical at the crossing point and the CMP is fully hybridized, i.e., it consists of 50 % photon and 50 % magnon excitation.
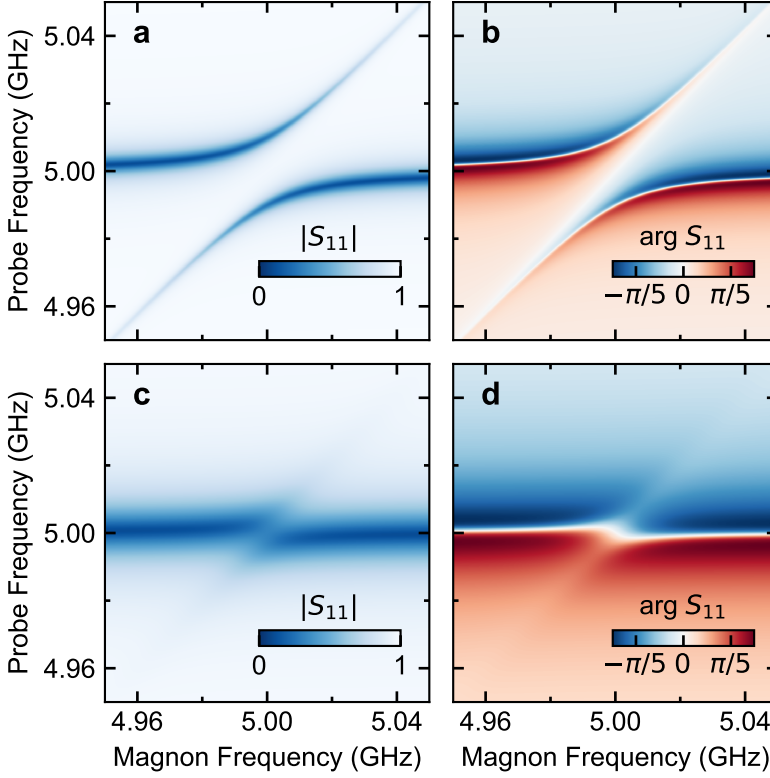
Figure 3.3: Dispersion spectra of the CMP probed in reflection for strong and weak coupling. Panel **a** and **b** display amplitude and phase signal of a strongly coupled CMP dispersion spectrum for different magnetic field values / magnon frequencies. Data are calculated according to Eq. (3.37) with $g > \kappa_L, \kappa_r$. Panel **c** and **d** illustrate the dispersion spectra of a weakly coupled CMP ($g < \kappa_L, \kappa_r$).

The behavior for a weakly coupled CMP ($g = 5\,\text{MHz} > \kappa_L = 10\,\text{MHz}, \kappa_r = 1\,\text{MHz}$) is displayed in Fig. 3.3c, d. Here, the energy stored in one mode is lost before the two systems can interact with each other and hence no mode splitting is visible. This is also emphasized in the phase signal, where one can only see a single phase jump. Accordingly, no linewidth hybridization can be observed.

To summarize, we can experimentally record CMP dispersion spectra, from which we can extract the important properties characterizing the CMP and their underlying physical mechanisms.
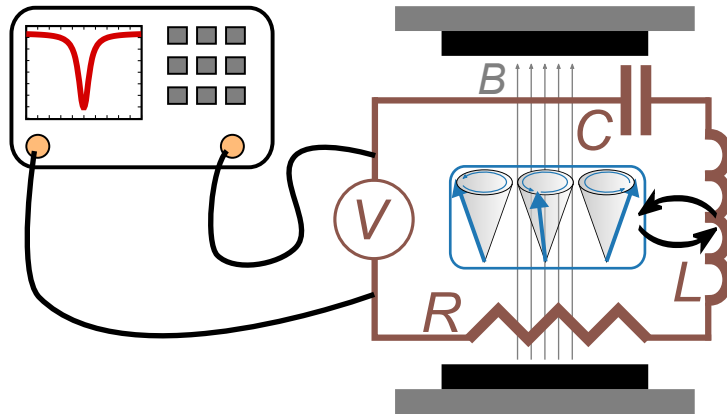
Figure 3.4: Standard measurement setup for cavity magnon polariton (CMP) experiments. The cavity hosting the magnetic material is brought into an external static magnetic field and connected to a network analyzer via a coupling probe. This allows the measurement of the CMP's *S*-matrix element. By changing the external magnetic field, the magnon resonance can be brought close to the cavity resonance and the two systems interact.

3.3.3 Spectroscopic Setup

After the theoretic discussion of the CMP's spectrum, the question remains: how does one access this quasi-particle experimentally? The basic spectroscopic measurement setup comprises a vector network analyzer and the CMP sample, which is placed inside a static magnetic field. CMP research has almost exclusively been performed with spectroscopic setups akin to the one sketched in Fig. 3.4. Here, only the cavity is excited and probed with the VNA. Without the static external field, the system is described by the equations discussed in Sec. 3.2. For CMP measurements, all of the previous mentioned resonator configurations are applicable. By increasing the magnetic field, the FMR mode can be tuned close to the cavity resonance, where it is then excited by the cavity's magnetic field. This interaction changes the microwave response of the system and one can observe the hybridized CMP eigenmodes and the mixture of dissipation channels, as explained in Sec. 2.3.

4 Controlling the Coupling Strength

4.1 Introduction and Geometric Control

The coupling strength may be considered the most crucial parameter of a coupled system. Based on design considerations, it can be engineered easily as opposed to an improvement of the decay rates. Recall from Sec. 2.4, that a high coupling strength is necessary for the strong coupling regime and therefore for information processing devices. A precise control of the coupling strength is hence important in this context.

The coupling strength is normally given by the geometric design of the cavity field in conjunction with the position of the magnonic material, due to the underlying magnetic dipole interaction. The coupling strength can be calculated [Zha+14] via:

$$g = \frac{\eta}{2} \gamma \sqrt{\frac{\hbar \omega_c \mu_0}{V_a}} \sqrt{2Ns},$$
(4.1)

with N as the total number of spins (with spin number $s = 5/2$ for YIG) in the sample, μ_0 the vacuum permeability, V_a the mode volume of the cavity and $\eta \leq 1$ is an overlapping coefficient of how well microwave field and magnon mode match spatially. Considering mainly the uniform mode, one can rewrite the equation to [Flo+19]:

$$g = \frac{\gamma}{2} \tilde{\eta} \sqrt{\frac{\mu_0 \mu}{g' \mu_B} n_s \hbar \omega_c},$$
(4.2)

$$\tilde{\eta} = \sqrt{\frac{\left(\int_{V_m} \mathbf{H} \cdot \hat{\mathbf{x}} \, dV\right)^2 + \left(\int_{V_m} \mathbf{H} \cdot \hat{\mathbf{y}} \, dV\right)^2}{V_m \int_{V_c} |\mathbf{H}|^2 \, dV}}.$$
(4.3)

μ denotes the magnetic moment of the sample ions, g' the g-factor of the electron, n_s the spin density of the material and $V_{m,c}$ the volume of the magnetic sample and cavity respectively. This expression, in contrast to Eq. (4.1), does not directly depend on the number of spins (only the spin density) but on how much magnetic field is inside the sample, as determined by $\tilde{\eta}$. It thus gives us a more intuitive

instruction on engineering the cavity to control the coupling strength. Roughly speaking, a high coupling strength can be achieved by confining the magnetic field mode of the cavity to exactly the volume of the magnetic sample.

However, once the cavity is machined and the magnonic material is fixed at one position, the coupling strength has been set, as is evident from Eq. (4.2) - at least at first glance. Yet, we will see that we can still control the coupling strength for a given geometry during the experiment: One can apply a second, *continuous* drive tone applied to the magnon [Wan+18] tricking it into seeing a different field geometry. Moreover in this two-tone scheme, choosing the right parameters of the drive tones allows for a transition from level repulsion to so-called "level attraction", first observed for the CMP by Harder *et al.* [Har+18]. In the level attraction regime, the two CMP eigenmodes do not repel each other but coalesce in the vicinity of the crossing point. Level attraction has been observed in a variety of physical systems. In CMPs, this phenomenon arises mostly because of a dissipative coupling, for which an overview is given by Wang and Hu [WH20]. A microscopic explanation can be found in Ref. [PMS19]. Level attraction can also observed for the right interplay of positive and negative decay rates with respect to the coupling strengths [Zha+17]. Moreover, it also occurs in optical systems and was reviewed in the context of exceptional points by Miri and Alu [MA19].

In this chapter, the focus lies on a theoretical overview of the possibilities given by a two-tone coupling strength control. I will first explain the theoretical proposal [GSX18] and its experimental realization. From the modified coupling model, one can derive the normal modes together with their eigenfrequencies and extract the (now) complex coupling strength. Rewriting the system in the language of quantum mechanics, i.e., in second quantization, we can employ the input-output formalism to calculate the dispersion spectra of a two-tone CMP. However, those spectra are idealized cases, which are often difficult or impossible to replicate exactly for such open systems. Some subtleties in these derived spectra have, especially in cavity magnonics, not yet been given proper attention and will be pointed out at the end of the chapter.

The presented project was realized in a cooperation between KIT and the University of Mainz. The experiments were performed with a CMP comprising a re-entrant cavity [Gor+18] and a YIG sphere with diameter $d = 0.2\,\text{mm}$. The experimental results that support the theoretical discussion and can be found in Refs. [Bov+20; Bov+19].
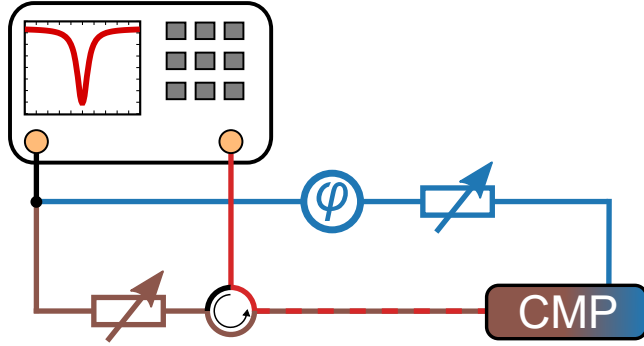
Figure 4.1: Spectroscopic two-tone setup for a control of the coupling strength. The two-tone setup is an extension of the standard CMP measurement setup. Not only the cavity part (brown lines) but also the magnon system (blue line) can be excited directly. The signal of the first VNA port is split, which ensures a constant phase difference for the two oscillating systems. This phase difference φ can be controlled with a phase shifter in the magnon line. Additionally, variable attenuators are installed in each line allowing for the control of the amplitude ratio Δ between the two signals. The cavity is probed in reflection but due to the split signal, a circulator is used forwarding the reflected signal to the second port of the network analyzer. Thereby, unwanted reflection from the magnon system are avoided. See also [Bov+20; Bov+19].

4.2 Theoretical Proposal and Two-Tone Microwave Setup

The CMP is normally probed with a single tone to the cavity (Ch. 3). However, in a theoretical study Grigoryan *et al.* [GSX18] included a second drive tone directly applied to the magnon and extended the phase correlation model [Bai+15]. The crucial point is now that the two drive fields can have an arbitrary phase difference φ and amplitude ratio $\Delta = A_{\mathrm{r}}/A_{\mathrm{c}}$, with $A_{\mathrm{r,c}}$ as driving amplitudes of magnon system and cavity, respectively. The additional magnon drive field can superpose the magnetic field produced by the cavity current and therefore affects the coupling between cavity and magnon, leading to a modified Eq. (2.16):

$$
\begin{pmatrix}
\omega^2 - \omega_{\mathrm{c}}^2 + 2i\beta\omega_{\mathrm{c}}\omega & \omega^2 K^2 \\
\omega_{\mathrm{m}}(1 + \Delta e^{\mathrm{i}\varphi}) & \omega - \omega_{\mathrm{r}} + i\alpha\omega
\end{pmatrix}
\begin{pmatrix}
h \\
m
\end{pmatrix} = 0. \tag{4.4}
$$

Here, in contrast to Eq. 2.16, we already substituted the magnetic field h for the cavity current to ensure equal units of the drive fields and redefined $K = \sqrt{K_{\mathrm{c}}K_{\mathrm{m}}}$, following Ref. [GSX18]. Now, one can identify the additional term containing $\Delta e^{\mathrm{i}\varphi}$ as a consequence of the second drive field, which is due to the FMR dynamics

governed by the LLG (Sec. 2.2). Standing in an off-diagonal element, this term already indicates that the coupling can be altered, controlled by the two parameters φ and Δ. A quantitative discussion will follow in the next sections.

Furthermore, Grigoryan *et al.* also predicted that for a value of $\varphi = \pi$ and an amplitude ratio $\Delta = 2$ the two eigenmodes will coalesce, or in other words, the levels attract each other. This level attraction, however, is indeed more ubiquitous in this system and the above stated parameters are just one example, where "pure" level attraction can occur.

One way to add a second phase-coherent drive tone is given by the setup [Bov+20] displayed in Fig. 4.1. The signal of a VNA is split into two parts, one part traveling to the cavity and the other to the magnon system. A mechanical phase shifter is included in the magnon path, allowing one to vary the phase offset. The desired amplitude ratio can be controlled by variable attenuators in each path. To probe the CMP spectrum, we insert a circulator in front of the cavity and record the reflected signal with the second VNA port. This way, reflections from the magnon port to the readout port are minimized.

4.3 Complex Coupling Strength of the Driven Two-Tone CMP

The presented effects in Ref. [GSX18] were mostly confined to few calculated CMP dispersion spectra for special cases of Δ and φ. To obtain a better overview about the control possibilities of such a system, we will more systematically explore the behavior of the CMP eigenmodes with respect to our control parameters. We start by linearizing the coupling equations with the (classical) RWA, which yields

$$\begin{pmatrix} \omega - \tilde{\omega}_c & g_0 \\ g_0(1 + \Delta e^{i\varphi}) & \omega - \tilde{\omega}_r \end{pmatrix} \begin{pmatrix} h \\ m \end{pmatrix} = 0, \tag{4.5}$$

with g_0 as the geometrically defined coupling strength. To calculate the eigenvalues, we diagonalize Eq. (4.5) and obtain similar results as the single-tone CMP eigenfrequencies, Eq. (2.14) but with a new expression for the coupling strength

$$g(\varphi, \Delta) = g_0 \sqrt{1 + \Delta e^{i\varphi}}. \tag{4.6}$$

By choosing right parameters of Δ and φ, we can set the coupling strength to be completely real, totally imaginary or have both, a real and imaginary part. A
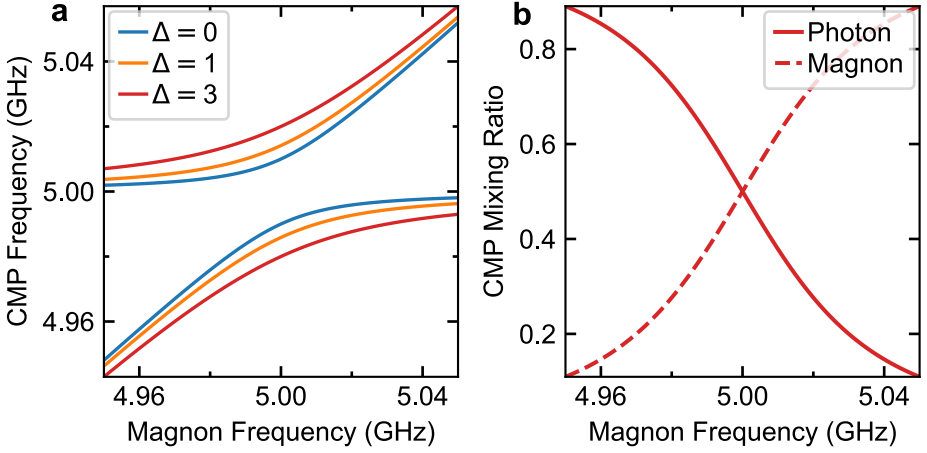
Figure 4.2: Increased Level repulsion. Panel **a** shows the real part of the CMP, when cavity and magnon drive are in-phase. The coupling strength increases with increasing amplitude ratio Δ and therefore the anticrossing gap widens. **b** The mixing ratio of photon and magnon is given by the square of the normalized eigenvectors and is equal to that of a single-tone CMP. This is exemplary shown for the upper branch of the anticrossing and $\Delta = 3$.

complex coupling strength is associated with dissipation (gain or loss) during the coupling [MA19]. Depending on the complex value of g, the frequency spectra of the eigenmodes show distinctly different behavior. We will find the normal level repulsion regime (g is real), level attraction (g is purely imaginary) or a coexistence of both.

4.3.1 Increased Level Repulsion

Setting the phase-difference to $\varphi = 0$ results in a constructive (in-phase) superposition of cavity and magnon drive field. The magnetic field as seen by the magnon increases for larger Δ. Considering Eq. (4.2), we intuitively suspect a greater coupling strength due to the stronger field at the sample position. And indeed, Eq. (4.6) explicitly confirms this presumption. Since g remains real, the same is true for the eigenfrequencies. For larger Δ and thereby greater g the avoided level crossing gap widens, see Fig. 4.2a. The CMP mixing ratio, i.e., the percentage of magnon and photon excitation, also shows the same behavior as the single port CMP (Fig. 4.2b). A second, in-phase drive tone thus allows for an "in-situ" increase of the repulsion coupling strength.

Increasing the coupling strength through drive tones may come in handy for pushing the CMP, despite potential design constraints, into the ultra-strong cou-
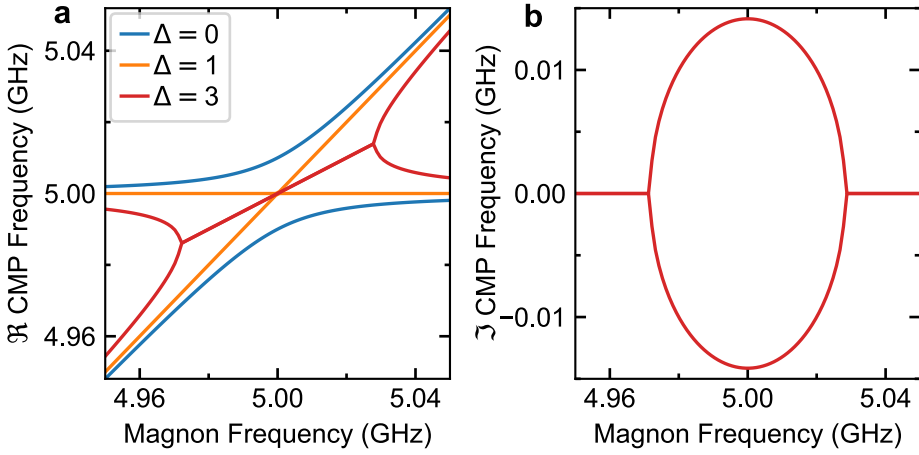
Figure 4.3: Level attraction. a Setting the two drive tones with $\varphi = \pi$ first closes the anti crossing gap and then leads to the level attraction of the eigenfrequencies. If g is purely imaginary, i.e. $\Delta > 1$, the eigenmodes coalesce and are identical over a frequency range of $4g$. **b** Imaginary part of the CMP eigenfrequency for level attraction.

pling regime or even the deep-strong coupling regime, which may not be possible otherwise for two Hookian-like coupled oscillators (Sec. 2.4).

4.3.2 Level Attraction

In the previous section, the two drive tones were applied in-phase, leading to a real coupling strength. In contrast, applying the two drive tones in anti-phase ($\varphi = \pi$) changes the picture fundamentally: First, for $\Delta < 1$, the local magnetic field at the magnon sample decreases with increasing Δ and hence the anti crossing gap shrinks. Increasing Δ further, beyond unity, transitions the coupling strength to an imaginary quantity and instead of level repulsion, we find level attraction. Here, the curvatures of the two modes have a different sign compared to the repulsion case, which finally leads to their coalescence. The points of coalescence are called exceptional points [MA19]. Over a region of $4\Im g$ the real part of the two CMP eigenfrequencies (see Fig. 4.3a) remain identical. However, the eigenfrequencies now also have an imaginary part (Fig. 4.3b) associated with gain or loss, leading to an unstable mode [Ber+18]. For level attraction as well, by changing Δ, we can control the value of the coupling strength, and subsequently the frequency range of the mode coalescence.
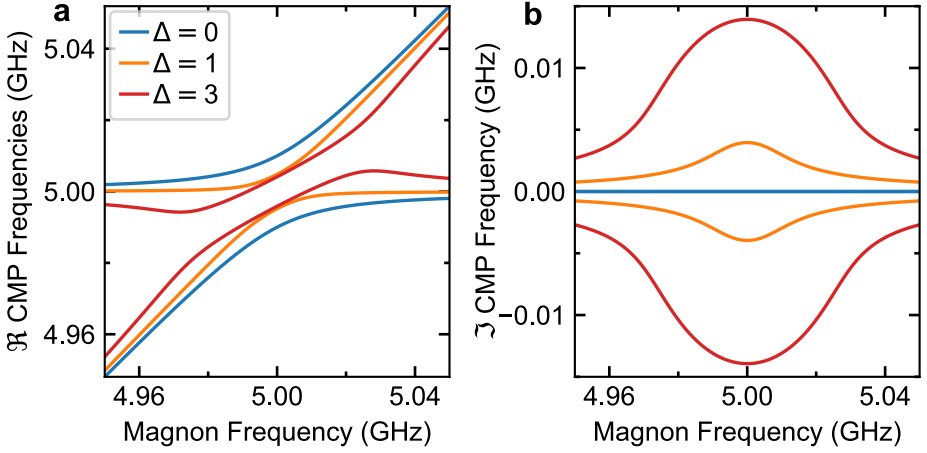
Figure 4.4: Coexistence of repulsion and attraction. a The CMP eigenmodes show a simultaneous attraction and repulsion for a coupling strength with real and imaginary part; in this case $\varphi = 7/8\pi$. The two modes never coalesce, they repel each other by $2\Re g$ but run in parallel over a range $4\Im g$. **b** Imaginary part of the eigenfrequencies. In contrast to the pure level attraction regime, the eigenfrequencies are imaginary over a broader region than $4\Im g$.

4.3.3 Coexistence of Repulsion and Attraction

We have discussed the two special cases in which the drive tones are either in-phase leading to increased repulsion or anti-phase resulting in level attraction. In contrast to the dissipative coupling and controlled decay rates engineered via the cavity geometry [Har+18; Bho+19; Zha+17; Yao+19a; Yao+19b; Yan+19], our setup additionally enables us to set the phase difference to any arbitrary value. For cases of $\varphi \neq 0, \pi$ and $\Delta > 1$, the coupling strength, according to Eq. (4.6), becomes a complex number with both real and imaginary part. The real part repels the coupled mode while the imaginary part attracts the coupled modes. We are in a regime where both level repulsion and level attraction coexist. This effect is best visible for large Δ and φ close to π. Figure 4.4a shows that the two modes never coalesce completely. They are still separated by a gap of $2\Re g$. Nevertheless, they run in parallel over a range of $4\Im g$, similar to pure level attraction. Again, the eigenfrequencies become complex quantities, even over a wider frequency range as in the pure attraction regime. Similar to before, the imaginary part leads to an unstable mode. Although the eigenfrequencies can easily be calculated, measuring unstable modes is, of course, another question, which will be discussed in the next section.

4.4 Dispersion Spectra of the Two-Tone CMP

Seeing the progression of the eigenfrequencies gives a good picture about the underlying physics. However to observe the CMP, we have to rely on dispersion spectra. Recall, a complex coupling strength is associated with gain or loss and subsequently the calculated eigenmodes can become unstable and do not show as dips in the dispersion spectra.

We can calculate the dispersion spectra for the two-tone CMP employing input-output theory (see Sec. 3.3), similar to Refs. [Har+18; Bov+20]. This will give a basic understanding, what we can expect in the experiment but, as we will see later, it does not offer a complete description. The first step is to rewrite the coupling Eq. (4.4), into the quantum version:

$$\mathcal{H} = \omega_c a^\dagger a + \omega_r m^\dagger m + g_0 \left(m^\dagger a + \left(1 + \Delta e^{i\varphi} \right) a^\dagger m \right). \tag{4.7}$$

This equation is a non-Hermitian Hamiltonian, which is necessary to account for the open system due to the second drive, affecting the photon and magnon occupation numbers. This non-Hermiticity also leads to non-real eigenvalues, as seen in the previous section. Please also note that the role of $a^\dagger m$ and $m^\dagger a$ is switched in contrast to Ref. [Bov+20]. In this work, the Hamiltonian is chosen such that the correspondence to the electrodynamic equations, Eq. (4.4), is preserved. The results remain the same for all practical purposes. We can now employ Eq. (4.7) to calculate the derivatives of the annihilation operators $\mathcal{F}(\dot{a})$, $\mathcal{F}(\dot{m})$ for the input-output formalism. Comparing the new results with the operator equations for the single-tone CMP, Eq. (3.35) and Eq. (3.36), we notice that a simple substitution of the coupling strength, $g^2 \rightarrow g_0^2 \left(1 + \Delta e^{i\varphi} \right)$, in Eq. (3.36) is sufficient. Subsequently, the new reflection coefficient for the two-tone CMP becomes:

$$S_{11}(\omega) = 1 - \frac{2\kappa_c}{i\left(\omega_c - \omega\right) + \kappa_L + \frac{g_0^2 \left(1 + \Delta e^{i\varphi} \right)}{i(\omega_r - \omega) + \kappa_r}}. \tag{4.8}$$

Evaluating this equation for reasonable values, we can observe theoretical dispersion spectra, as depicted in Fig. 4.5. Normal level repulsion and increased level repulsion are shown in Fig.4.5a,b. The dispersion spectra look as usual due to the completely real coupling strength. Next, we can examine the dispersion spectrum for perfect level merging (Fig.4.5c.) Here, the magnon mode is not visible since cavity field and magnon drive field cancel each other out and hence no magnon mode will be excited. Unfortunately, such a perfect field matching is difficult or
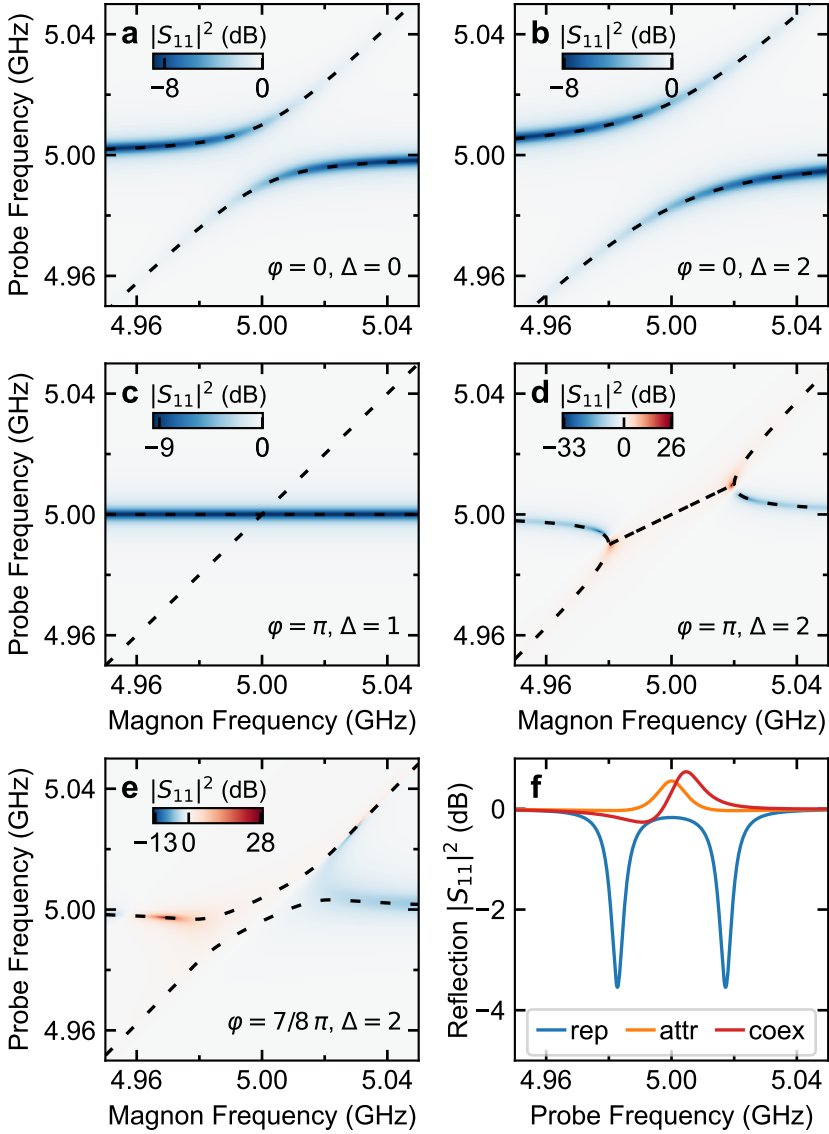
Figure 4.5: Dispersion spectra of the two-tone CMP calculated according to Eq. (4.8). Dashed lines denote the eigenfrequencies of the CMP. Depending on the control parameters, amplitude ratio Δ and phase difference φ, opposing regimes of level repulsion and attraction can be reached. **a** Avoided level crossing of the single tone CMP. **b** The level repulsion can be increased by two in-phase tones resulting in a widening of the anticrossing gap. The eigenfrequencies remain visible as simple dips. **c** At perfect level merging the magnon mode would not be excited and only the resonanator dip is visible. **d** Level attraction can be observed for the anti-phase driven CMP. Exceptional points show up in a theoretically diverging amplitude. **e** For a phase difference $\varphi \neq 0, \pi$, both, level attraction and repulsion coexist. **f** Line cuts at the crossing point of **b,d,e** giving a comparison of repulsion (rep), attraction (attr) and coexistence (coex).

43

even impossible to realize experimentally, and therefore a magnon mode is always observed.

The spectrum for level attraction (Fig.4.5d) shows how the two modes move towards each other, following the previously calculated eigenfrequencies. The linear slope of the coalesced modes, however, is only barely visible, due to the discussed mode's instability [Ber+18]. For equal decay rates of magnon and photon, the reflection amplitude diverges in the point where the two modes coalesce, i.e., at the exceptional points. Poles in the S-Matrix have also been found for optical systems [CGS11]. Although exceptional points do not obey conversation laws because the systems exchange energy with their environment [MA19], it is not possible to observe such a strong divergence in the experiment, where the maximum power is simply given by the VNA output and hence the input-output formalism should be used with care. The same behavior of a non-physically increased amplitude can be seen in the coexistence regime (Fig.4.5e). Yet, whereas for level attraction only a small peak is visible at the crossing point, in the coexistence regime a dip and a peak feature, representing the two non-coalesced eigenmodes, can be observed (Fig.4.5f).

An additional problem of the input-output approach for an imaginary coupling strength is apparent in the phase response, $\arg S_{11}$. The measured phase jump of 2π for a transmission cavity [Har+18] is not given by input-output theory, see Appendix A.1 for more details.

Moreover, for the two-tone approach, imperfect field configurations and crosstalk can affect the measured amplitude drastically, making the interpretation of experimental data difficult. It is also noted that, different from Ref.[Bov+20], the second drive tone has only been considered implicitly through the non-Hermitian Hamiltonian; and not by an additional transmission channel S_{12} through the CMP.

4.5 Discussion

The theoretical presentation in this chapter demonstrates that the geometrically defined coupling strength can still be altered through a second microwave tone that is directly applied to the magnon system. Two parameters, phase difference and amplitude ratio of these drive tones allow for a control of the coupling strength in the complex plane. The experimental results underpinning this overview are presented in Refs.[Bov+20; Bov+19], showing the discussed widening and closing of the anticrossing gap, as well as level attraction and coexistence. It should be noted that due to the coupling geometry, the superposition of the drive fields is
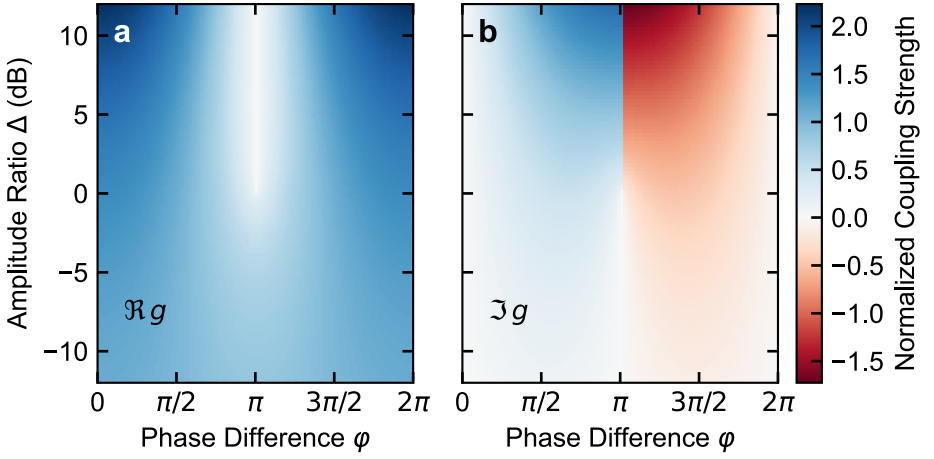
Figure 4.6: Color-coded depiction of the normalized complex coupling strength g/g_0 according to Eq. (4.6). **a** The real part of the coupling strength is responsible for level repulsion. Values greater than 1 represent an increase of the geometrically defined coupling strength and values smaller than 1 a decrease of it. **b** Imaginary part of the coupling strength leads to level attraction. Only for $\varphi = \{0, \pi\}$ pure repulsion or attraction regimes can be observed (white lines). Otherwise level attraction and repulsion coexist.

more complex than the assumption of a linear polarization, leading to experimental imperfections with respect to the discussed dispersion spectra.

For the two-tone technique, the coupling strength is best described as a complex number, accounting for energy loss/gain in the process. The real part represents the amount of level repulsion and the imaginary part that of level attraction. Figure 4.6 summarizes the dependence of the coupling strength on amplitude ratio and phase difference, Δ and φ.

The two-drive configuration is one more option to achieve level attraction in the CMP. However, it stands apart from other realization by its in-situ control over the coupling strength and the possibility to prepare the CMP in a coexistence of repulsion and attraction. If and how level attraction in the CMP can be used in a dynamic case and for information processing has not yet been answered. Nevertheless, it was theoretically linked to entanglement [Yua+20] in the single magnon regime and may thus prove useful for quantum technologies.

In conclusion, the addition of a second drive tone fundamentally changes the static picture of a coupling fixed by geometry and allows for a control over level repulsion and level attraction.

5 Coherent Mode Control in the Time Domain

5.1 Introduction

In this chapter, we will switch from continuous drive signals, allowing for a control of the coupling strength, to short pulses, permitting an on demand manipulation of the CMP. Still relying on the two-port CMP, we will now observe its response to pulsed measurements in the time domain as opposed to frequency space. Instead of changing the coupling strength, our goal is now to excite the different CMP modes (see Sec. 2.3) and demonstrate coherent, i.e., phase stable, control over both subsystems, cavity and magnon system.

Current information processing schemes are based on ns-short gates for data extraction and manipulation. But despite the CMP's promising potential for information technology, most CMP experiments have been confined to probing the steady state of this quasi-particle under continuous driving and mostly with one single tone. In only a few experiments, short pulses were applied to the CMP [Zha+14; Mat+19; Mor+17]. But even in these studies, solely single pulses to the cavity were used and therefore only the beat mode with its periodic energy exchange could be excited. Normal modes during free evolution were not observed. However, for the CMP to unfold its full potential in the area of information processing, one should be able to exert control over the different CMP states at arbitrary times. Replacing the network analyzer by a time-domain measurement setup will enable us to coherently control the CMP. It is then possible to not only excite the CMP in any mode but also to dynamically control the occurrence of these modes as well as the stored energy in the system.

In the following, I will first explain the measurement setup allowing for coherent control and then shortly give a characterization of the measured sample. After that, we will study the experiments that demonstrate fast and dynamic control over both subsystems of the CMP, and accordingly over the different oscillating modes. The results presented in this chapter led to the publication of Ref. [Wol+20].
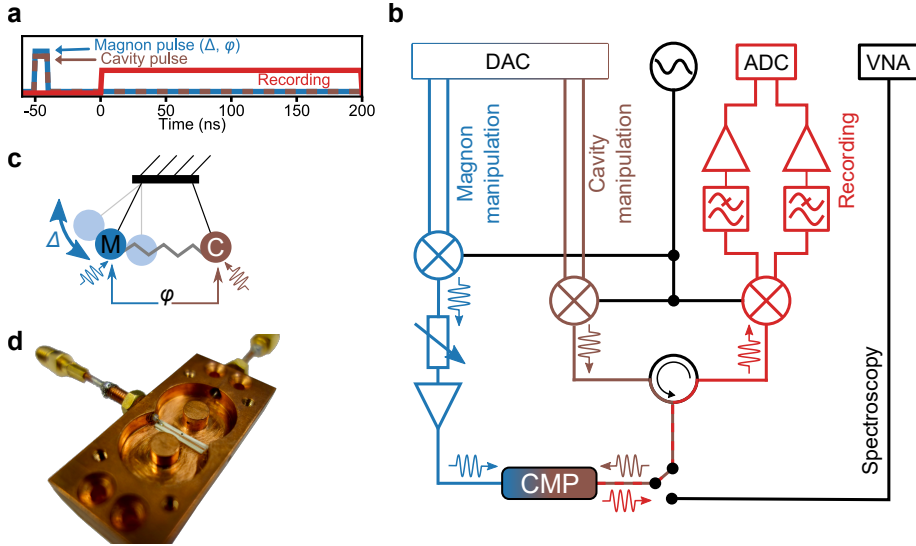
Figure 5.1: Time domain setup for coherent cavity magnon polariton (CMP) manipulation. **a** Possible pulse sequence for a coherent control of the CMP. **b** The microwave setup comprises three parts: cavity manipulation, magnon manipulation and recording. For manipulation purposes ns-short pulses are generated with a digital to analog converter (DAC) and then upconverted into the GHz regime with a continuous microwave signal. The emitted energy coming back from the cavity is downconverted, filtered and amplified before it is digitized with an analog to digital converter (ADC). For spectroscopic characterization, the sample is also connected to a vector network analyzer via a microwave switch. **c** Effect of the control parameters, phase offset φ and amplitude ratio Δ in the picture of two coupled pendula. **d** Photograph of the employed sample, consisting of a re-entrant cavity [Gor+14] and a YIG sphere with 0.5 mm diameter. The cavity field is excited via a coupling loop and the magnon system via a stripline underneath the sphere. Figure adapted from [Wol+20].

5.2 Experimental Methods

5.2.1 Microwave Time Domain Setup

A versatile microwave setup builds the foundation that makes coherent control of the CMP possible. Here, a simple vector network analyzer is not enough. Instead, we need the flexibility of pulse sequences with pulses differing in length and amplitude. Such a setup has to meet at least the following requirements:

- Independent ns-short pulses to both subsystems,

- Adjustable but stable phase offset between all applied pulses,

- Adjustable amplitude ratio of the applied pulses,

- Recording of the outgoing energy from either subsystems with ns resolution.

Similar requirements can be found for the control of quantum systems based on superconducting qubits [Kra+19]. Phase coherent pulses can, for instance, represent quantum gates, or prepare the system in quantum simulations experiments [Bra+17], and help characterizing qubits [Ste+20]. We have adapted the microwave setup for a continuous recording of the cavity while sending phase-coherent pulses to magnon system and cavity. A typical pulse sequence with two simultaneous pulses to cavity and magnon system is displayed in Fig. 5.1a.

The microwave setup, depicted in Fig. 5.1b can be divided into three parts: cavity manipulation, magnon manipulation and cavity recording. For both manipulation parts, short ns pulses having a complex carrier frequency of $f_{\mathrm{car}} = 200\,\mathrm{MHz}$, are generated with an arbitrary waveform generator (AWG). This enables us to choose an arbitrary phase offset φ between any two pulses. The AWG comprises two pairs of digital to analog converters (DAC); one pair for each manipulation line. A single microwave source emits a continuous signal to upconvert the pulses to the resonance frequency of our system, $\omega_{\mathrm{c}} = \omega_{\mathrm{r}}$, via single side band mixing with identical IQ mixers. The upconversion preserves the chosen envelope and phase of the generated pulses. The magnon manipulation additionally includes a voltage controlled attenuator followed by an amplifier to control the amplitude ratio Δ of the applied pulses (see Fig. 5.1c for visualization in the pendula picture).

The cavity is probed in reflection and thus a circulator is inserted in front of the cavity port, which transfers the manipulation signals to the cavity and returning the reflected and re-emitted signals to the recording line. The signal coming back from the cavity is downconverted into its IQ components via the previously split microwave tones. The IQ components are then low pass filtered, amplified and recorded.

5.2.2 Data Processing

We control all measurement devices and record the data with qkit [qki], an open source measurement suite. Due to the heterodyne character of the measurement setup, the recorded time traces still exhibit the carrier frequency. Employing a digital down conversion to DC, i.e., multiplying the complex signal by $\mathrm{e}^{\mathrm{i}2\pi f_{\mathrm{car}}}$, we remove the carrier frequency and eliminate higher frequency components by low-pass Butterworth filter with a cut-off frequency of $0.8 f_{\mathrm{car}}$. From the processed data, we then calculate the amplitude $\sqrt{I^2 + Q^2}$ of the reflected signal, which is linked to the stored energy in the system. To find the correct proportionality factor between recorded amplitude and outgoing power of the cavity, we replace the cavity with a

microwave source, sweep the emitted power and record the amplitude, with the described technique.

5.2.3 Pulse Sequence Calibration

Before we can employ the presented measurement setup for coherent control experiments, a correct calibration of the cable delay between the two manipulation lines is crucial. The necessary phase and amplitude matching can only be ensured if the pulses for cavity and magnon reach the sample simultaneously. Utilizing the normally unwanted crosstalk between the two ports at the sample gives a straightforward way for an extraction of the cable delay. We emit two Gaussian pulses for each line respectively with a known delay, leading to one pulse with a high amplitude reflected from the cavity line and one pulse transmitted from the magnon line with a low amplitude in the recorded signal. By using Gaussian pulses we not only minimize amplitude distortion from the microwave setup, sample and post processing but we can also extract their mean values from a fit of their amplitude (see Appendix Fig. B.1). We extract a delay time of 7 ns, by which we correct the emission of the pulses at the AWG. However, we will later observe that even a timing mismatch below 1 ns can cause slight discrepancies from theory (see Sec.5.4.2).

For most experiments in this project, we choose square pulses with a length of 10 ns. Although these short pulses are heavily distorted by the notch-type filter of the cavity and magnon system, our motivation was to find a compromise of Dirac delta-like excitation pulses and sufficient energy in the system.

5.2.4 Numerical Simulation Technique

We also compare our experimental results to numerical simulations. For that, we use the standard set of differential equations for two coupled oscillators and model the drive tones in a way that we can easily investigate the influence of crosstalk, i.e, a superposition of the two drive fields at the place of each resonating system as well as timing mismatches:

$$\ddot{x}_c + 2\beta\omega_c\dot{x}_c - g^2\omega_c x_r = (1 - \zeta)F_c + \zeta F_r, \tag{5.1}$$

$$\ddot{x}_r + 2\alpha\omega_r\dot{x}_r - g^2\omega_r x_c = (1 - \zeta)F_r + \zeta F_c, \tag{5.2}$$

with

$$F_c = A_c \cos(\omega_0 t)\, \theta(t - t_{c,1})\, \theta(t_{c,2} - t), \tag{5.3}$$

$$F_r = A_r \cos(\omega_0(t - \delta t) - \varphi)\, \theta(t - t_{r,1})\, \theta(t_{r,2} - t). \tag{5.4}$$

$x_{c,r}$ denote the amplitude of the cavity and the magnon oscillator, respectively. Using heaviside functions in the drive force, we can model our drive tones $F_{c,r}$ as 10 ns short square pulses and also include timing mismatches $\delta t = t_{r,1} - t_{c,1} = t_{r,2} - t_{c,2}$. Hence, this set of equations models our experiments, where a driven system followed by free evolution is considered. The parameters $A_{c,r}$ represent the strength of the linear drive force and hence the power ratio of stored energy is given by[1] $\Delta = A_r^2/A_c^2$. Crosstalk is taken into account by the parameter ζ, defining the (linear) amount of the drive force that acts on the other resonating system. Additionally, choosing slightly different resonance frequencies provides us with the possibility to observe the effects of an unwanted detuning $\Delta f = (\omega_r - \omega_c)/2\pi$

Having set up our model and defined the parameters, we solve the equations with the `scipy.integrate` package and use the solutions to calculate the stored energy in the cavity:

$$E_c(t) = \frac{1}{2}\omega_0^2 x_c^2 + \frac{1}{2}\dot{x}_c^2. \tag{5.5}$$

Since the coupling constant (from transmission line to oscillator) is neglected in this model, we adjust the stored energy to the observed one at the time the first pulse ends with a constant parameter. By including several pulses in Eqs. (5.3) and (5.4) we can also simulate the dynamic control experiments in Sec. 5.5.

5.3 Sample Characterization

The CMP sample used for coherent control is displayed in Fig. 5.1d. It is similar to the one employed in Ref. [Bov+20] and mentioned in the previous chapter. This time however a YIG sphere with a diameter of 0.5 mm is installed, i.e., placed in the antinode of the cavity's magnetic field. The bigger diameter increases the coupling strength, compare Sec. 4.1. This increase allows for an observation of several magnon Rabi oscillations within the natural decay of the system. The magnon system is excited via the magnetic field of a microstrip line, which gives a homogeneous ac-field and reduces the crosstalk due to the perpendicular geometry of all magnetic fields. See Appendix B.2.

---

[1] Equal coupling constants for resonator and magnon system are assumed.
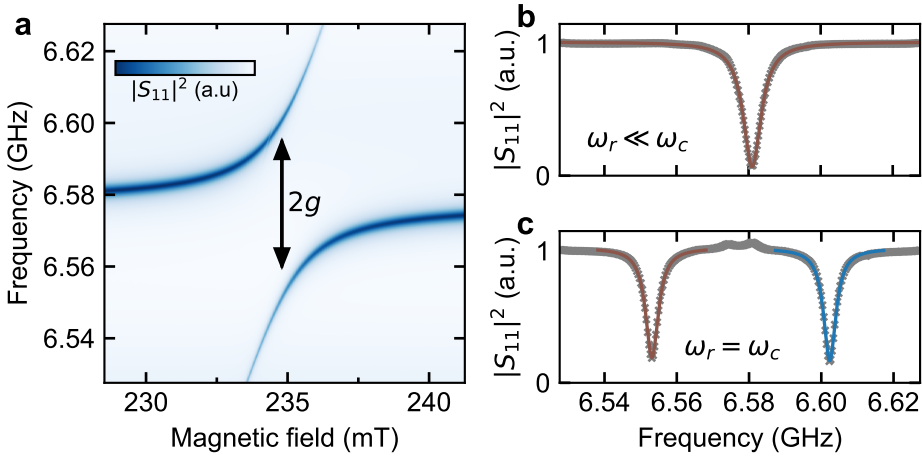
Figure 5.2: Spectroscopic characterization of the cavity magnon polariton. a Avoided level crossing as the signature of strong coupling. The two normal modes are visible as dips in the dispersion spectrum. **b** Background corrected linetrace of the pure cavity resonance with the magnon far detuned ($\omega_r \ll \omega_c$) and **c** linetrace at the crossing point ($\omega_r = \omega_c$), where magnon and cavity mode are equally hybridized. Solid lines represent Lorentzian fits to the measurement data (gray points). Figure adapted from [Wol+20].

We first characterize this sample spectroscopically by applying a continuous drive from the VNA to the cavity port. Fig. 5.2a shows the characteristic avoided level crossing of the Kittel mode with the cavity resonance, typical for the strong coupling regime. We can fit the dispersion curves of the avoided level crossing to Eq. (2.14) and extract a coupling strength of $g/2\pi = 24.7$ MHz. This result is in agreement with theoretical calculations for this geometry [Bov+18]. An additional higher order FMR mode can also be seen close to the crossing point, at 234 mT, which is not of interest for this work.

We extract the decay rates of the system from spectroscopic data measured off-resonant (Fig. 5.2b) and at the crossing point, where the two resonance dips are equally broad (Fig. 5.2c), compare Sec. 2.3. Lorentzian functions are fitted to the two dips of the background corrected data. The fits at the crossing point yield a linewidth (HWHM) of $\kappa_{crp}/2\pi = 2.1$ MHz corresponding to $(\alpha + \beta)/2 = 0.032\%$. Tuning the FMR away and fitting the pure cavity resonance gives a linewidth of $\kappa_c = 3.0$ MHz and hence $\beta = \kappa_c/\omega_c = 0.046\%$ ($Q_L = 1090$). With these values, we can find the frequency independent Gilbert damping factor $\alpha = 0.014\%$ ($Q = 3570$) for the Kittel mode. We can conclude that $g > \kappa_{c,r}$ and thus the spectroscopic characterization also confirms the strong coupling regime quantitatively.

5.4 Control of Oscillator Modes

Recall from Sec. 2.3 that the CMP, similar to coupled pendula, can be excited in the in-phase mode ξ_+, the anti-phase mode ξ_- and the beat mode ξ_0. In this section, the different modes will be observed in the time-domain. We furthermore show how the parameters Δ and φ of the manipulation pulses have to be chosen for any superposition of these CMP modes.

5.4.1 Beat Mode and Normal Modes

Beat Mode - Single Pulse Experiment

The system's parameter g, κ, found spectroscopically, are linked to the decay time τ and the period of the classical magnon-Rabi oscillation t_R via Fourier transformation. To measure these corresponding time domain parameters, we emit a single pulse to the cavity but none to the magnon system. We monitor the out-coming power from the cavity and sweep the external magnetic field around the crossing point in between the recorded time traces. This procedure leads to the characteristic chevron Rabi pattern displayed in Fig. 5.3a, which was similarly observed in Refs. [Zha+14; Mat+19], and can be considered as the time domain counterpart to the avoided level crossing. These oscillations occur because energy is periodically transferred between cavity and magnon system with a frequency given according to the generalized Rabi frequency

$$\tilde{g} = \sqrt{g_0^2 + \Delta\omega^2}, \tag{5.6}$$

and $\Delta\omega = \omega_c - \omega_r$. We can see that the Rabi frequency increases with further detuning, as observed in Fig. 5.3a. Taking the time trace at the crossing point (Fig. 5.3c, gray line) and fitting a damped sine to it, we extract a decay time of $\tau = 77.6\,\text{ns}$ corresponding well to the spectroscopic result of $1/\kappa_{\text{crp}} = 75.8\,\text{ns}$ and an oscillation period of $t_R = 2\pi/g = 1/24.6\,\text{MHz} = 40.6\,\text{ns}$ equaling the spectroscopic results. The slight distortion of the Rabi pattern at $234\,\text{mT}$ is due to the coupling to a higher order FMR mode. The single pulse experiment excited the beat mode, as expected, and confirms the spectroscopic results.

Normal Modes - Two Pulse Experiment

The next step is a two-pulse experiment, in which we excite one of the two normal modes $\xi_\pm$ instead of the beat mode. Hence, two pulses with a matched phase offset
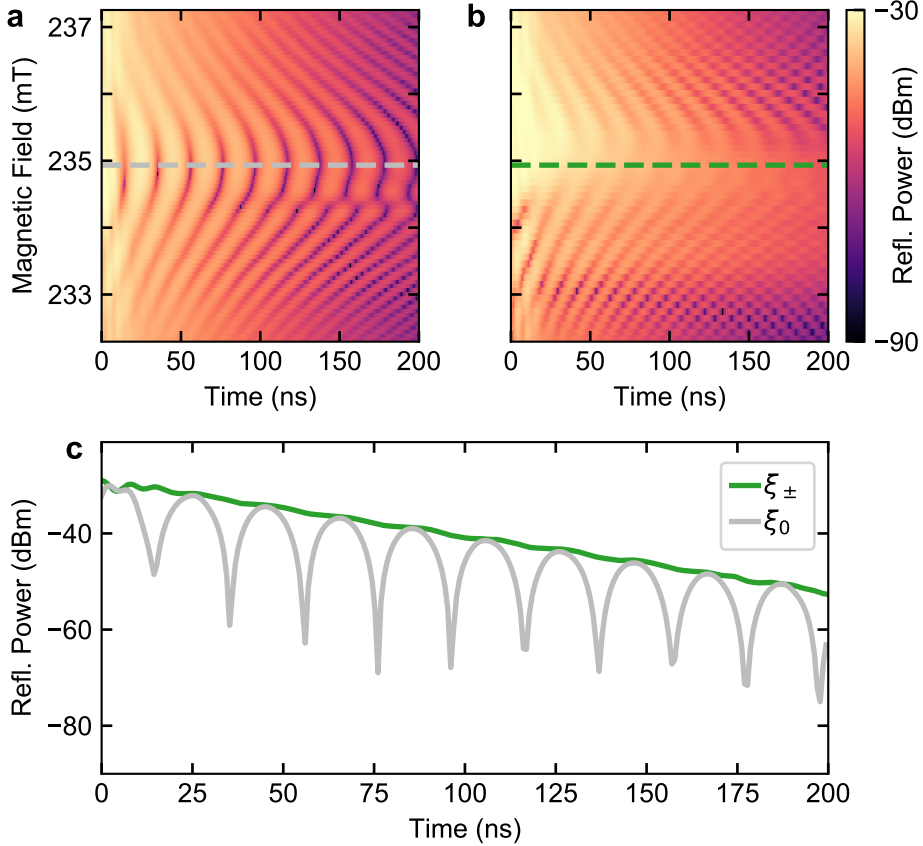
Figure 5.3: Time resolved cavity response for beat- and normal mode of the cavity magnon polariton (CMP). a The time evolution of the cavity for different magnetic field values shows classical magnon Rabi oscillations, i.e., the beat mode ξ_0, after a single excitation pulse to the cavity. The energy swaps periodically between the two sub systems. Another spurious magnon mode is visible close to 234 mT. **b** Normal mode $\xi_\pm$ response of the cavity. Phase and amplitude matched pulses are emitted to cavity and magnon. At the crossing point (dashed line), the two sub-systems are excited equally, no energy is exchanged and the magnon Rabi oscillations are suppressed. **c** Line cuts at the crossing points emphasizing the different responses of the beat and normal mode of **a** and **b**. As expected, the beat mode shows sinusoidal oscillations whereas the normal mode shows a straight exponential decay. [Wol+20]

and amplitude ratio are applied to the cavity and magnon system simultaneously. We again sweep the magnetic field over the crossing point to compare the one-pulse Rabi pattern with the two-pulse one (Fig. 5.3b). Far detuned from the crossing point, where the amplitude matching does not hold, we can observe Rabi oscillations in both cases. If the FMR approaches the cavity resonance however, the oscillations become more shallow and vanish completely at the crossing point. We can thus observe how the second pulse directly changes the state of the CMP from the beat mode to one of the normal modes.

Fig. 5.3c illustrates the difference of the two modes by a comparison of the time traces at the crossing point. The two-pulse time trace shows a simple exponential decay with no oscillations. Hence, no energy is exchanged and both systems oscillate with the same amplitude and follow the applied phase offset as predicted by the electromagnetic model and intuitively understood in the picture of coupled pendula. The measured results agree well with numeric simulations of two coupled oscillators (see Appendix B.3). We thus conclude that we can indeed not only excite the beat mode ξ_0 but also the normal modes $\xi_\pm$ with the presented technique.

5.4.2 CMP Mode Composition

Considering the picture of two coupled oscillators, we know that any superposition of beat and normal mode should be possible to excite, depending on the chosen initial state, which translates to applied phase offset and amplitude ratio in CMP experiments. Our first goal is to find an analytic expression of the CMP mode composition with respect to these two controlling parameters. Afterwards, we test how well the analytic solution can be reproduced experimentally.

Analytic derivation of the CMP Mode Composition

Again, we start with the expression, Eq. (5.5), for the stored cavity energy

$$E_c(t) = \frac{1}{2}\omega_0^2 x_c^2 + \frac{1}{2}\dot{x}_c^2, \tag{5.5'}$$

in which we will later substitute Δ and φ. In the next step, we have to find equations for the amplitude x_c of the cavity oscillator and its derivative. These are given by the general solution for two coupled oscillators:

$$x_c = A\cos((\omega_0 + g)\,t + \phi_0) + B\cos((\omega_0 - g)\,t - \phi_0), \tag{5.7}$$
$$x_r = A\cos((\omega_0 + g)\,t + \phi_0) - B\cos((\omega_0 - g)\,t - \phi_0), \tag{5.8}$$

with A,B and ϕ_0 as free parameters depending on the initial condition, i.e., the state of the oscillator right after the pulses have stopped. The damping term has been neglected since it can be factored out and therefore does not change the CMP mode composition over time. Substituting Eq. (5.7) and its derivative into Eq. (5.5) while neglecting terms proportional to g, since $g \ll \omega_0$, yields

$$E_c(t) = \frac{1}{2}\omega^2(|A|^2 + |B|^2) + \omega^2 |AB| - 2\omega^2 |AB| \sin(g\,t + \phi_0)^2. \tag{5.9}$$

The parameters A and B are already denoted as complex variables. We express them via matrix transformation of the non-diagonal system defined by our control parameters: $A = 1 + \Delta e^{i\phi}$ and $B = 1 - \Delta e^{i\phi}$.

$$E = \frac{\omega_0^2}{2}\left(\underbrace{2\left(1 + \Delta^2\right) - 2\sqrt{(1 - \Delta^2)^2 + 4\Delta \sin^2 \varphi}}_{c(1-\lambda)} + \underbrace{4\sqrt{(1 - \Delta^2)^2 + 4\Delta \sin^2 \varphi}\cos(g\,t + \phi_0)^2}_{c(1+\lambda)} \right). \tag{5.10}$$

The first underlined term is constant over time and hence corresponds to the normal mode, whereas the second underlined part contains an oscillating term and therefore describes the amount of the beat mode. Employing the underlined abbreviations and solving for c and λ yields

$$\lambda = \frac{-\Delta^2 + 3\sqrt{(\Delta^2 + 1)^2 - 4\Delta^2 \cos^2 \varphi} - 1}{\Delta^2 + \sqrt{(\Delta^2 + 1)^2 - 4\Delta^2 \cos^2 \varphi} + 1}, \tag{5.11}$$

$$c = \Delta^2 + \sqrt{(\Delta^2 + 1)^2 - 4\Delta^2 \cos^2 \varphi} + 1, \tag{5.12}$$

We can define a new constant p_0, which includes c and gives the proportionality between stored energy and emitted power of the system. Eq. (5.10) with its natural exponential decay can then be rewritten as

$$P_c(t) = p_0 \left[(1 - \lambda) + (1 + \lambda) \cos^2(g\,t + \phi_0)\right] e^{-t/\tau}. \tag{5.13}$$

This equation describes the time evolution of the CMP system in the strong coupling regime depending on the parameter λ, which has inherent bounds of -1 and 1. For $\lambda = 1$ the CMP exists in the pure beat mode ξ_0 and for $\lambda = -1$ in either normal mode $\xi_\pm$. The parameter λ is therefore a measure for the CMP mode composition. Figure. 5.4a depicts the analytic solution for the mode composition with respect to Δ and φ. As expected, the normal modes (red elliptic regions) can be excited for matching power ratio and phase offsets of 0° and 180°. A phase offset of $\varphi = \pm 90°$ results in the beat mode (blue area) for any power ratio. If the power ratio is big enough, the phase offset is inconsequential and mainly the beat mode is excited, as is evident from the picture of two coupled oscillator. In between these values, superpositions of beat mode and normal mode are possible; containing equal amounts, for example, as displayed by the white regions in Fig. 5.4.

Experimental Verification

To verify the capability of our control technique, we compare the analytic solution to experimental data. Cavity and magnon system are tuned to the crossing point. We apply simultaneous pulses to each subsystem and sweep the phase offset of the pulses as well as the attenuation in the magnon manipulation line. Eq. (5.13) is fit to the recorded time traces for every combination of φ and Δ, from which λ is extracted and displayed in Fig. 5.4b. The experimental results reveal a behavior close to the analytic solution. We can identify the two red elliptic regions representing the normal modes surrounded by the blue area standing for the beat mode. However, one can observe a shift towards lower frequency and a slope between the two ellipses. Investigating these discrepancies, we use numeric simulations and recognize that these deviations are most likely caused by a remaining cable delay δt below the resolution of the DAC (1 ns), spurious crosstalk ζ between one subsystem and the microwave port of the other system or a remaining frequency detuning Δf due to a drifting external magnetic field. Figures 5.4c,d show the effects of these parameter. For example the simulated data with $\delta t = 0.01$ ns and $\zeta = 0.1$ reproduce the experimental results well and would explain the slight deviations from the analytic solution.

In conclusion, arbitrary phase offsets and power ratios for the applied pulses enable us to prepare the CMP system in any superposition of beat mode and normal mode. The experimental results agree well with the oscillator model and the electromagnetic coupling model [Bai+15]. Moreover controlling the CMP subsystems separately allows to choose the phase offset between the systems at will and independent of the external magnetic field. This extends the results of Bai *et al.*, where the phase offset for a single pulse experiment was purely given by the external field. Such a control over the phase offset may benefit spin rectification experiments [HGH16].

5.5 Dynamic Control

Coming back to our introductory statement with the need for short gates in CMP based information technology, we now demonstrate a dynamic control of the CMP within a single decay. The experimental results are numerically verified and explained in the picture of coupled oscillators.
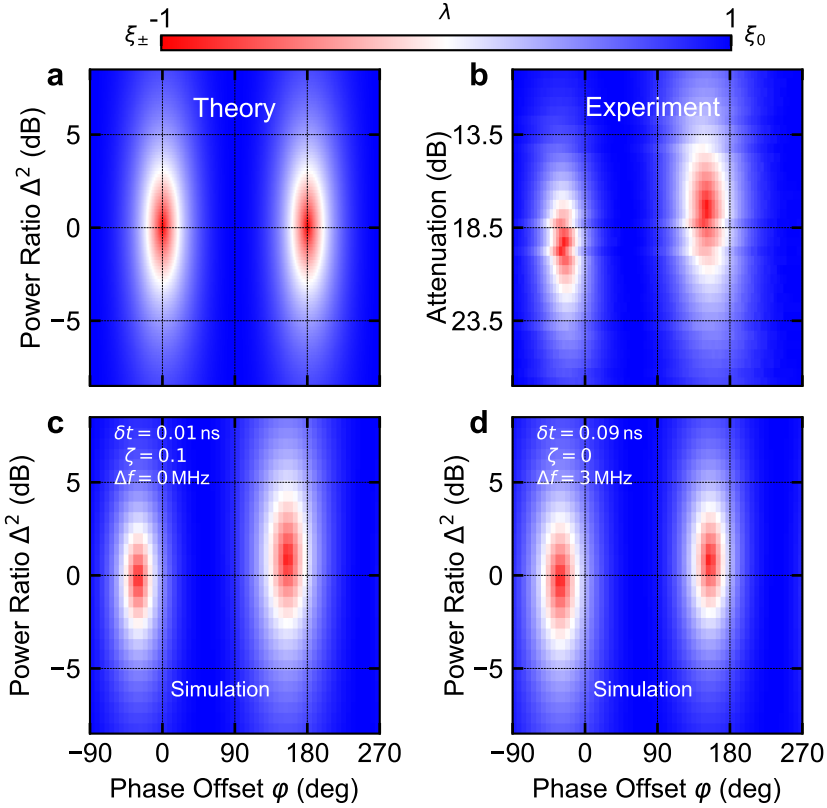
Figure 5.4: Mode composition of cavity magnon-polaritons (CMP). The mode composition of a CMP can be controlled via applied phase offset φ and power ratio Δ^2. The parameter λ is a measure for the mode composition with -1 representing the normal modes (red regions), 1 the pure beat mode (blue region) and any superposition in between. **a**. Analytical solution calculated from Eq. (5.11). **b** Experimental data of the cavity response. λ is extracted from fits of Eq. (5.13) to the measured time traces. The experimental attenuation corresponds to the power ratio with an undetermined offset. Slight discrepancies can be explained by experimental imperfections such as a minimal time lag between the pulses δt, crosstalk ζ or mismatched resonance frequencies Δf. **c** and **d** show simulated results incorporating these imperfections. [Wol+20]
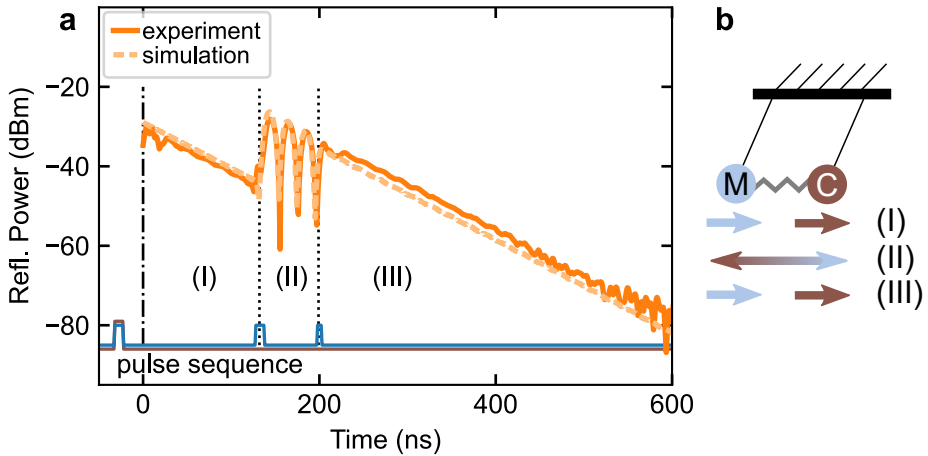
Figure 5.5: Dynamic control of energy exchange. a The time resolved response of the cavity can be divided into three phases: (I) The cavity magnon polariton (CMP) is excited in the normal mode by matching pulses to both subsystems. (II) A second pulse to the magnon introduces energy and brings the system in the beat mode. Energy exchange happens until a third pulse equalizes the energies of the two subsystems and (III) the CMP is again in its normal mode. Simulated data agree well with the experiment. Solid blue and brown lines represent applied pulses (height not scaled). **b** Pendula representation illustrates the different modes during the decay. [Wol+20]

5.5.1 Dynamic Manipulation of the Mode Composition

In this experiment, we expand the capability of mode composition control to the dynamic case. Our goal is a change from normal mode to beat mode and back within a single decay of the CMP. The experimental results are shown in Fig. 5.5a. Again, we tune the CMP to its crossing point and prepare it in its normal mode by matching pulses to magnon system and cavity. A single exponential decay can be observed; both systems have the same energy and oscillate with a fixed phase offset (0° or 180°). Circa 150 ns later, we apply a second pulse only to the magnon system, such that an energy difference between the two sub-systems arises. The excess energy will now be transferred between the two systems. Hence, the CMP is in its beat mode and classical magnon Rabi oscillations are visible in the cavity response. We shortly let the CMP evolve freely before bringing it back to the normal mode; again by applying a pulse only to the magnon system. This pulse must have a matched phase and amplitude such that either the excess energy of the magnon is extracted or if, at the time of the pulse, the energy is stored in the cavity, the same amount of energy has to be introduced to the magnon system. We also note that due to the finite length of the microwave pulses and the coupling between the two systems, an applied pulse always affects both systems. It is therefore
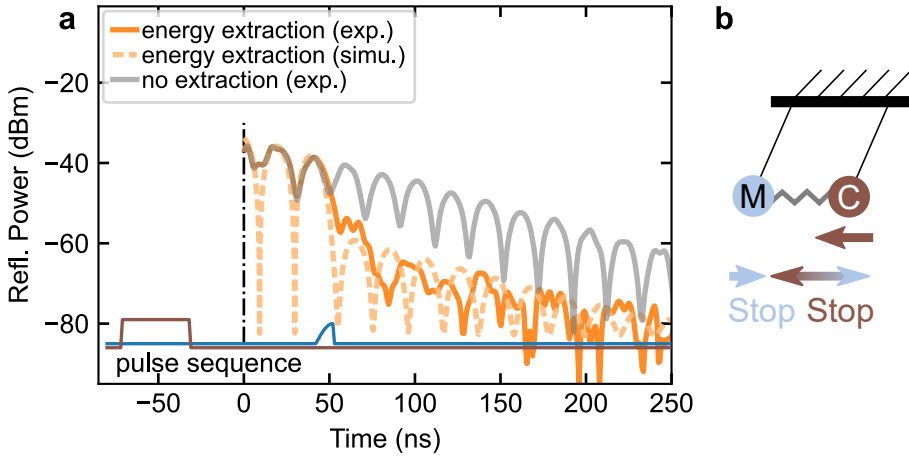
Figure 5.6: Time resolved cavity response of dynamic energy extraction. a A first pulse to the cavity excites the cavity magnon polariton (CMP) in the beat mode. Applying a second anti-phase drive tone to the magnon system extracts the total energy by destructive interference. This extraction is visible in a 20 dB drop compared to the unextracted response (gray line). Solid blue and brown lines represent applied pulses (height not scaled) for the extraction case. Ring-up, $t < 0\,\text{ns}$, is omitted for clarity. **b** Pendula sketch represents the applied scheme and its effect. [Wol+20]

crucial to find the correct timing, phase offset and amplitude, which we achieve by sweeping all parameters in the simulation and experiment. After this pulse, the Rabi oscillations stop and a pure exponential decay is visible. The CMP is prepared in one of its normal modes again. The experimental results are additionally verified by numerical simulations (dashed line in Fig. 5.5) showing an excellent agreement.

The just described behavior can also be intuitively understood in the picture of the coupled pendula (Fig. 5.5b). The first simultaneous pulses excite both pendula with the same amplitude and the coupled system oscillates in-phase (anti-phase). The second pulse gives an additional push to one pendulum. It therefore oscillates with a higher amplitude and this additional energy is periodically transferred between the pendula. Then the third pulse softly equalizes the amplitudes of both pendula. The translation to the electromagnetic model can be easily drawn by substituting cavity current and FMR magnetization for either pendulum.

5.5.2 Dynamic Energy Extraction

In a second experiment we replicate a technique known as active noise control (ANC) [EN90; KM99] in acoustics, which is currently especially popular in headphones, and apply it to the CMP. ANC is based on destructive interference to hinder

acoustic noise from reaching one's ear. The incoming acoustic wave is recorded, its anti-phase counterpart is calculated in real-time and emitted so that the two waves cancel each other out at the position of the observer.

Here, we show a complete energy extraction from the CMP system by emitting an anti-phase pulse. The results are displayed in Fig. 5.6a. A first pulse to the cavity brings the CMP into its beat mode. We let the Rabi oscillations shortly evolve. At the time, when the energy is transferred from the cavity to the magnon system, we apply an amplitude matched pulse in anti-phase to the magnon system countering the incoming energy and hence extracting almost all energy. This manifests in a sharp 20 dB-drop of the reflected cavity power. Again, we note that due to the strong coupling applying an anti-phase pulse to the magnon also influences the cavity and hence the pulse has to be timed correctly such that it matches cavity as well as magnon energy. Leaving this last comment aside, we can again intuitively understand this CMP behavior in the picture of two coupled pendula (see Fig. 5.6b). The first pendula is excited and the system is found oscillating in its beat mode. In the moment when all energy is transferred to the second pendulum, we suddenly stop this pendulum by grabbing it and therefore both pendula are at rest containing no energy anymore.

We validate the experiments by a numerical simulation, which reproduces the observed behavior well. The amount of the drop in the reflected power strongly depends on the accuracy of the amplitude matching. The chosen simulation parameters also result in a 20 dB drop but in the simulation, the classical Rabi-like oscillation continue as there is still energy left in the system. These low amplitude oscillation mix with input noise in the experiment

The two presented experiments demonstrates the first dynamic and coherent control schemes of the CMP. These schemes allow for a manipulation of the CMP modes and for a change of the overall energy during its natural decay time.

5.6 Discussion

In summary, we established a coherent control over both CMP parts, the cavity and magnon system, by using manipulation pulses on the timescale of nanoseconds. With the presented time domain setup, we are able to observe the transition from the beat mode (maximum energy exchange) to the normal modes (no energy exchange) of the CMP at its crossing point. Furthermore, we employed these results for a dynamic control of the different modes and for the extraction of the total energy from the system by destructive interference within the sample. All the

results agree well with the CMP theory models of coupled oscillators and phase correlation developed by Bai *et al.* [Bai+15]. The consistency of our experiments and numerical simulations underpins the validity of these coupling models.

The demonstration of coherent control in the time domain may open the door to further information technology research based on the CMP. On the one hand, the regime of level attraction, discussed in Ch. 4, has been theoretically linked to entanglement [Yua+20], which may be useful for quantum computing application in the future, and predictions for the CMP time evolution have been given. The presented setup here would allow for preparing the CMP in this regime and subsequently a validation of the given predictions. On the other hand, by adding a non-linearity, such as a superconducting qubit, to the system, it should be possible to encode qubit states in magnons [Rei15] with gate schemes similar to what has been shown with superconducting resonators [Hof+08; Leg+13; Vla+13; Hee+17]. The disadvantage of the short magnon life time compared to superconducting resonators is balanced by their demonstrated capability in converting microwaves into optical light [Osa+16; Hai+16]. Hence, one may think of hybrid systems comprising superconducting resonators for storage and magnon based frequency converters for long range information transfer, leading to a functional quantum network [Kim08].

6 Towards Understanding Magnon Decoherence

6.1 Introduction

Quantum devices strongly suffer from environmental noise [Kra+19], which limits their life- and coherence time. Through interaction with the environment, information can become lost. Whereas much effort has been spent on improving the coherence times of superconducting qubits [Kra+19; OW13], the same is not true for magnonic materials. This has opened a gap in coherence, see Sec. 2.5, which may hamper the usefulness of the CMP as a mediator between quantum systems and magnetic devices drastically. Research on decoherence mechanisms in magnons is thus imperative.

Investigating coherence properties of a resonating system, one can examine the linewidth as well as the jitters of the resonance frequency, i.e., frequency noise. Both methods are ways to probe the resonator's environment and possible loss channels. While the linewidth is primarily a measure of the lifetime (see Sec. 3.2) mainly due to energy loss, frequency noise may give information about the interactions with several other resonating systems in the environment. Gaining information about these systems can in turn help improving lifetimes.

A prominent example for the connection between loss and frequency noise are fluctuating two-level systems (TLS) [MCL19]. Recall from Sec. 2.5 and recent experiments [Tab+15; Pfi+19; Kos+19] that magnons are believed to be subject to TLS influence. Furthermore, an interaction between TLS and a resonating system leads to frequency fluctuations. These fluctuations can be described by their noise power spectral density (PSD), a measure of the fluctuation strength in a given frequency interval. The PSD will be explained in detail in Sec. 6.2.1. Now, drawing on the knowledge derived for superconducting resonators [Gao+07; Bur+14; Bur+13; Bre+17], we know that a bath of TLS coupled to a resonator leads to the typical $1/f$-decay of the frequency noise PSD. Furthermore, this noise PSD is influenced by the drive power of the resonator and the ambient temperature. From the specific

temperature dependence, for instance, it could then be concluded that the TLS in the bath have to interact with each other [Bur+14]. Hence, crucial information about the noisy environment can be extracted by a noise spectroscopy.

Coming back to magnons: Little is known about noise in these systems apart from the finding of telegraphic noise in the transmission amplitude of a YIG-magnon waveguide [Rum+19]. In this chapter, we will now explore magnon frequency noise of a YIG sphere at mK-temperature. I will start by giving a theoretic description of noise, i.e., random processes (Sec. 6.2), before comparing different measurement setups for extracting frequency noise (Sec. 6.3) and explaining possible pitfalls in noise measurements. In Sec. 6.4, the measurement results are presented, compared to the results of TLS in superconducting resonators and subsequently examined with methods developed for time series analysis [Box+15].
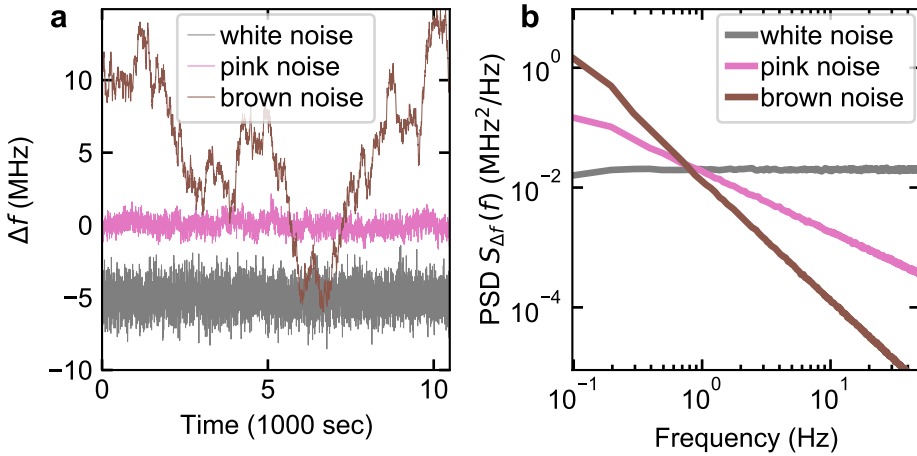
Figure 6.1: Comparison of noise processes with a different exponent in their frequency dependence. The time traces (**a**) of generated random data follow different frequency power laws as seen in their PSDs (**b**). The slope in the loglog plot gives the frequency exponent: white noise $\propto f^0$, pink noise $\propto f^{-1}$ and brown noise $\propto f^{-2}$. It is evident that with an increased (negative) exponent high frequency fluctuations are reduced, whereas big fluctuations occur over a long time. For better visibility time traces have an offset of $5\,\text{MHz}$ each and brown noise data is scaled by a factor of 0.3.

6.2 Statistics of Random Processes

6.2.1 Noise Power Spectral Density

Noise describes (unwanted) random fluctuations occurring in a specific variable; in our case the frequency shift Δf of the FMR. Tracking this shift over a certain time and with a given sampling rate f_s yields time traces showing the amplitude of these random fluctuations, see Fig. 6.1a. The standard way for noise analysis in physics is looking at these fluctuations in the frequency domain instead of the time domain. Here, the PSD $S(f)$ is the quantity of interest. The Wiener-Khinchin theorem [Wie30; Khi34]

$$S_{\Delta f}(f) = \int_{-T}^{T} r_{\Delta f}(\tau)\,e^{-i2\pi f\tau} d\tau \qquad (6.1)$$

relates the autocorrelation function

$$r_{\Delta f}(\tau) = \langle \Delta f(t)\Delta f(t+\tau) \rangle = \lim_{T\to\infty} \frac{1}{2T} \int_{-T}^{T} \Delta f(t)\Delta f(t+\tau)dt, \qquad (6.2)$$

to the PSD via Fourier transformation. The autocorrelation is a measure of how well the signal is correlated with itself for different time lags τ and is, in essence, a convolution. Employing the convolution theorem, one can easily calculate an estimate of the PSD, also called periodogram, by discrete Fourier transformation of the recorded time traces:

$$\tilde{S}_{\Delta f}(f) = \frac{1}{N f_s} \left| \sum_{n=1}^{N} \Delta f_n e^{-i2\pi f n\delta t} \right|^2. \qquad (6.3)$$

The tilde, which will be dropped from here on, denotes that this formula only gives an estimate of the "true" PSD. The PSD is normed correctly by the sampling rate and the number of samples N. The squared value of the signal in Eq. (6.3) accounts for the concept of power in a generalized form. Consequently, the PSD shows the fluctuation strength and its scaling on frequency. Also note that the PSD is a density and hence the noise power is calculated by an integration over the frequency interval of interest. The variance of the PSD however does not reduce with increasing samples N but instead one has to average M estimates to smooth it [Bar48]. In this work, Welch's method [Wel67] is employed for the PSD calculation. The recorded signal of N samples is split up into M segments with D overlapping points and additional windowed to reduce spectral leakage. The periodograms, Eq. (6.3), are calculated separately and then averaged. A long recording time with

a high number of segments yields a PSD with low variance, necessary for further insight about the underlying noise mechanisms.

Let us consider a few examples to become familiar with this concept: Considering so-called white noise, uncorrelated noise, we would find a δ distribution for $\tau = 0$ and zero everywhere else in the autocorrelation. The PSD therefore shows a flat line. However if a correlation over time exists, noise processes often, but not always, follow a simple power law $S(f) = \alpha/f^n$, where α describes the strength at $1\,\mathrm{Hz}$ and the exponent n defines the "type" or "color" of the noise process:

- white noise, no frequency dependence, $n = 0$,

- pink noise, higher power towards lower frequencies, $n = 1$,

- brown or red noise, even stronger power at low frequencies, $n = 2$,

Figure 6.1 visualizes these different types of noise processes. The noise color is often chosen in analogy to the respective frequencies of visible light and depends on the underlying random process.

As a last side note, the Wiener–Khinchin theorem is only applicable for signals that are wide-sense stationary, i.e., the mean value and the variance of the signal do not change over time. Fortunately, this requirement is fulfilled for all the measurements presented in this chapter.

6.2.2 Time Series Analysis - ARMA Model

Alas, as we will later see, the simple examples presented above are not adequate to describe magnon frequency noise. To quantitatively model this noise, we will have to leave the standard way of looking at the data only in the frequency domain but instead analyze the recorded time series directly. The chosen procedure to evaluate the data is related to what is known as "maximum entropy spectral estimation" [BdWB02].

Essential concepts to apply time-series analysis to magnon frequency noise are now explained. Details can be found in standard text books about the subject, e.g., Refs. [SS17; PW93; SZ99; Box+15]. A basic approach is the so-called ARMA model comprising the autoregressive (AR) and the moving average (MA) process. The data point y_t of a time series in this model is calculated as follows:
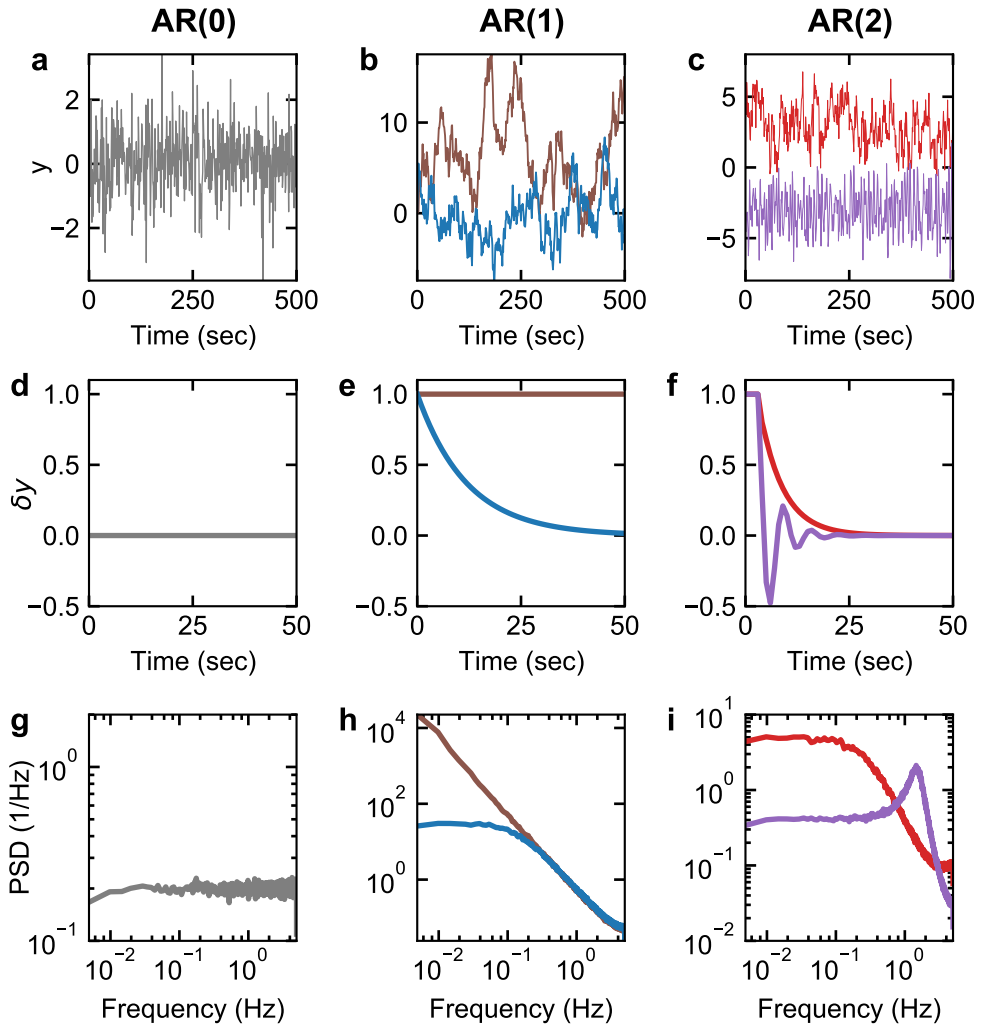
Figure 6.2: Examples of different order AR-processes. Panels in the first row (**a-c**) depict possible time traces of AR(0) to AR(2) processes. The AR(0) process is white noise calculated with $\sigma = 1$. The chosen parameters for the brown and blue line in the AR(1) processes are $a_1 = 1$ and $a_1 = 0.96$, respectively. The two AR(2) process' time traces are generated with $a_1 = 0.6$, $a_2 = 0.2$ (red) and $a_1 = 0.9$, $a_2 = -0.6$ and shifted by an offset for better visibility. The second row (**d-f**) illustrates the effect of a one-time shock δy, i.e., a single perturbation, over time. White noise AR(0) is independent of the current state. For brown noise (brown line) all random changes are summed up. Reducing a_1 (blue line) leads to an exponential decay of a one-time shock. For stationary AR(2) processes a one-time shock either decays in some form of exponential (red line) as well or shows a damped oscillations (purple line). This oscillation is also visible with a tendency to change sign the time trace. The last row (**g-i**) shows the power spectral density of the different processes.

$$y_t = c + \epsilon_t + \underbrace{\sum_{i=1}^{p} a_i y_{t-i}}_{\text{AR}(p)} + \underbrace{\sum_{j=1}^{q} b_j \epsilon_{t-j}}_{\text{MA}(q)}, \tag{6.4}$$

where c is a constant, denoting the mean, and can be set to zero by normalization, ϵ_t denotes Gaussian white noise with standard deviation σ. In the AR process, the next data point is the sum of the last p data points with weights a_i plus white noise, whereas in the MA process, a weighted sum of the last q noise terms is used for the next data point, again with added white noise. The focus lies on the AR-process and the MA-process is only used to illustrate the difference in the (partial) autocorrelation functions in the next section.

Again, we can gain an understanding of AR processes by looking at simple examples. Fig. 6.2 depicts the time traces (a-c), responses of a one-time shock, i.e. a single perturbation, (d-f) and the power spectral densities (g-i) of the AR(0) to AR(2) processes. It is evident that the AR(0) process is simple white noise, without any effects of shocks and a flat PSD, as previously discussed (Sec. 6.2.1). In the AR(1) process, choosing $a_1 = 1$ leads to a random walk, or in physical terms, Brownian noise. All noise terms are summed up. Considering the sum as a simple integration, which gives a factor of $1/f$ after Fourier transformation, explains why the PSD of Brownian noise follows the characteristic $1/f^2$ law. If $0 < a_1 < 1$, a one-time shock decays exponentially over time, and hence the system is pulled back to the mean value more strongly. Therefore, big fluctuations are forbidden and the PSD is found to be a Lorentzian. In continuous time, this process is known by the name "Ornstein Uhlenbeck process" [UO30] and was used to model Brownian motion with a friction coefficient. In the AR(2) process, one will either find a mean reverting force or a damped oscillation around the mean, depending on the chosen values for a_1 and a_2. Thus, the time series will either look similar to the AR(1) process or has the tendency to change the sign frequently, resulting in PSDs close to a Lorentzian or with some form of a peak at the oscillating frequency, respectively. Higher order stationary AR processes also either revert back to the mean or oscillate around it, described by sums of exponentials and oscillations. Of course, one could also find parameters a_i such that y_t diverges. These processes, however, are not stationary and hence not useful for our discussion.

Moreover, the PSD of an AR(p) process can be written in a closed form [Box+15]

$$S(f) = \frac{2\sigma^2 \delta t}{\left|1 - \sum_{k=1}^{p} a_k e^{-i2\pi k \delta t f}\right|}, \tag{6.5}$$
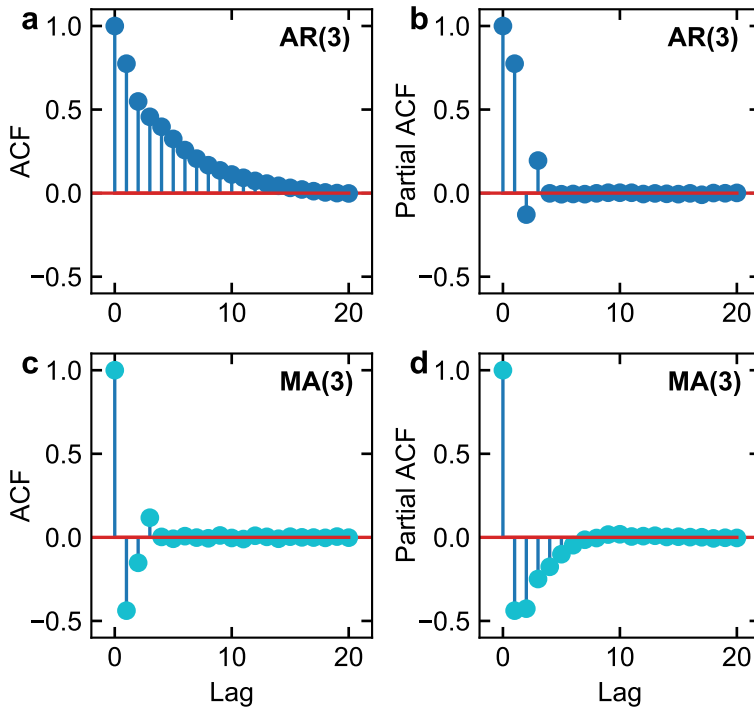
Figure 6.3: (Partial) autocorrelation functions of AR(3) and MA(3) processes. Panels **a** and **b** show the autocorrelation (ACF) and partial autocorrelation functions (PACF) of an AR(3) process, respectively. Panels **c** and **d** illustrate the same functions for an MA(3) process. AR(p) processes exhibit PACF values different from zero for lags up to p, whereas MA(q) processes show the same characteristic for q in the ACF. Hence, the order of either process can be estimated via the PACF and ACF, respectively.

with δt as the inverse sampling frequency. Hence, if the order and parameter values of the AR process are known, obtaining the PSD is straight forward.

6.2.3 Autocorrelation Function and Partial Autocorrelation Function

After this short discussion of the ARMA model, the natural question should be raised: How do we find out which process and what order describes our time series data? Fortunately, the answer is given by the autocorrelation (ACF) and partial autocorrelation function (PACF).

The ACF (in discrete time) describes how similar data points with certain time lag τ behave. Now, instead of using the integral definition Eq. (6.2), we consider

the stochastic version of the ACF: We calculate the (co-)variance for different time lags and normalize it by the overall variance σ_X^2:

$$r_\tau = \frac{\mathbf{E}\left[(X_t - \mu)(X_{t+\tau} - \mu)\right]}{\sigma_X^2}, \tag{6.6}$$

with μ as mean value. For the AR(1) process with $a_1 < 1$, one can immediately see that the autocorrelation function will decay exponentially, since the points with time lag n are influenced via a factor of a_1^n by the point at $t - n$. The white noise part should of course average out for enough data points. Similarly to the effect of one-time shocks in Fig. 6.2, the ACF of AR(p) processes will show an exponential-like decay with possible oscillations.

A concept, somewhat more intriguing, is the *partial* autocorrelation function. It calculates the direct (linear) similarity between data points with time lag n, i.e., the indirect influence via time lags up to $n - 1$ is removed. For instance, calculating the PACF for $n = 3$, the effect of a_1^3 and a_2^2 is removed. Since by definition no direct influence for lags $n > p$ exists in an AR(p) model, one can estimate the order p of the process by looking at how many lags show a value significantly different from zero in the PACF. Several ways exist to calculate the PACF. One such way is based on the Yule-Walker equations [Yul27; Wal31], which will be described in the next section.

Without going into detail, but to contrast the AR process to the MA process, we find the exact opposite: The MA(q) process shows value up to q in the ACF, as a direct consequence of its definition, where shocks only affect values up to time lag q. On the other hand an exponential-like decay is seen in the PACF. Figure 6.3a-d summarizes the previous paragraphs by illustrating this opposite behavior of the MA and AR processes in the ACF and PACF. It also concludes how the order of the respective process can be estimated.

6.2.4 Yule-Walker Equations

Solely determining the order of an AR-model of course is not sufficient. The next step must be to estimate the respective coefficients. Here, the Yule-Walker equations come in handy. They are a set of linear equations relating the AR coefficients to the autocorrelations. Furthermore, they can also be employed to calculate the PACF. The equations, written in matrix form, are as follows:

$$\begin{pmatrix} 1 & r_1 & r_2 & \dots \\ r_1 & 1 & r_1 & \dots \\ r_2 & r_1 & 1 & \dots \\ \vdots & \vdots & \vdots & \ddots \\ r_{p-1} & r_{p-2} & r_{p-3} & \dots \end{pmatrix} \begin{pmatrix} a_1 \\ a_2 \\ a_3 \\ \vdots \\ a_p \end{pmatrix} = \begin{pmatrix} r_1 \\ r_2 \\ r_3 \\ \vdots \\ r_p \end{pmatrix}. \tag{6.7}$$

Here, r_i denotes the autocorrelation at lag i. Hence, after knowing the order p of the AR process, we can calculate the a_i coefficients by simply estimating the r_i according to Eq. (6.6) and solving Eq. (6.7).

The Yule-Walker equations, also help in calculating the PACF. (The mathematical derivation can be found in Ref. [Box+15]). One can equate the order p of the AR process to the lag number n of interest and iteratively increase n and consequently p. Since in the AR process, the direct dependence between two data points with time lag p is given solely by $a_{p=n}$. Subsequently, this value represents the PACF at time lag n.

Although the Yule-Walker equations are simple to utilize, small errors in r_i can lead to unstable solutions. A more robust way, for example, is given by the Burg algorithm [BDT05], which estimates the parameters based on a least square prediction.

6.3 Measurement Setup

6.3.1 Comparison of Different Noise Spectroscopy Setups

To see how frequency noise can be measured, we will compare different measurement setups available for noise spectroscopy and show that, despite not often used in the literature, a commercial vector network analyzer may be the best choice due to its ease of handling. Fig. 6.4 shows schematics of the three measurement setups considered in the following:

Pound loop

The Pound loop [Lin+11] is the state of the art frequency noise measurement setup and was used on superconducting resonators, for instance. This setup tries to constantly lock the excitation frequency to the resonance frequency with a PID controller. Changes of the resonance frequency are registered via a power detector,
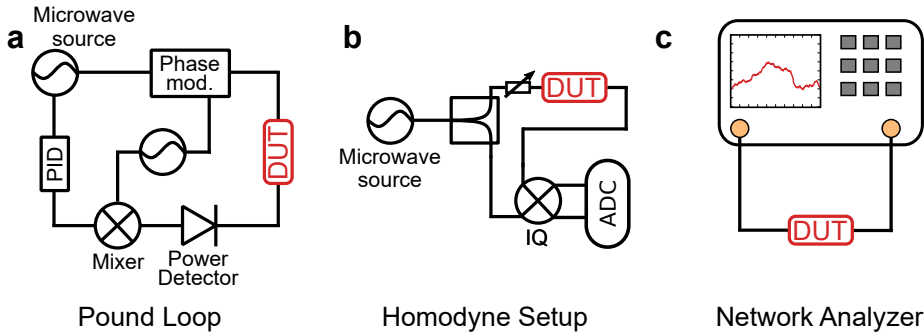
Figure 6.4: Schematics of different noise measurement setup. a The pound loop [Lin+11] locks the emitted microwave signal to the resonance frequency by constantly measuring the reflected or transmitted signal and correcting the frequency employing a PID controller if the resonance shifts. **b** The homodyne setup measures phase fluctuations due to frequency shifts of the resonator. The excitation frequency is kept constant and the signal is split allowing for a down conversion of the transmitted signal from the resonator. After down conversion, the IQ voltages are recorded and a time trace of $\arg S_{21}$ is calculated. This time trace corresponds to the fluctuations in the resonance frequency. **c** A vector network analyzer (VNA) is based on the same principle as the homodyne setup. However the VNA offers advantages during the measurement process, such as an easy calibration and a high dynamic range.

giving an error for the PID to be corrected. These frequency adjustments therefore directly give the frequency fluctuations over time. Despite its direct and precise measurement principle, the Pound loop has the drawback of a non-of-the-shelf and sophisticated setup, which can be difficult to build and to configure.

Homodyne Detection Setup

The basic ingredients of a homodyne setup are a microwave source, an ADC and an IQ-Mixer. The microwave signal with fixed frequency, roughly equaling the resonance frequency, is split such that one part excites the device under test (DUT) and the other part serves as a reference signal. The reflected/transmitted signal of the DUT is then converted to DC via the IQ Mixer and the reference signal. The I and Q voltages from the mixer are recorded with the ADC card. Since $\arg S_{21} = \arctan Q/I$ one measures phase fluctuations over time, which can be related to frequency noise. This setup was used in Refs. [Maz04; Gao+07; Gao08; Bre+17]. However it has several drawbacks: the IQ mixer is an imperfect device requiring a careful calibration. Moreover the range of power in which the IQ mixer performs well is limited and a conversion loss occurs. The choice of a suitable

ADC card is not trivial either, since one often needs a low sampling rate, sufficient memory and a high dynamic range.

Vector Network Analyzer

The homodyne setup is basically the self-made version of a commercial vector network analyzer. A VNA, though mostly used for frequency sweeps, also offers a continuous wave mode. The S-Matrix element can be recorded at a fixed frequency over time. This procedure is based on the same principle as above and hence the option we need for noise measurements. Compared to the previous setups, a VNA offers several perks, such as an easy calibration, low available sampling frequency, a high range of output power and a high dynamic range. The use of a network analyzer is straight forward, making it the setup of choice in this work. The main disadvantage is again that it measures frequency noise only indirectly via phase noise.

6.3.2 Conversion of Phase to Frequency Noise

As seen in Sec. 3.2, the phase response of a resonator arises due to the measurement process and is linked to the physical quantities. In our case, the quantity of interest is the resonance frequency. Interaction with the environment leads to fluctuations $\Delta\varphi$, which are then visible in the phase of the S matrix element. We can employ Eq. (3.16) for the phase response of a notch-type resonator at frequencies $\omega_0 + \Delta\omega$ and probe frequency ω_0. Neglecting the fluctuations in the denominator of the arctan argument, since $\Delta\omega \ll \omega_0$, we find the equation is equivalent to fixed resonator frequency and detuned probe frequency. Hence, we have a direct relation between phase $\Delta\varphi$ and frequency fluctuation. Moreover Eq. (3.16) can be linearized for small frequency fluctuations around the resonance frequency to

$$\Delta\varphi = (-2Q_\mathrm{L} + 2Q_\mathrm{i})\,\frac{\Delta\omega}{\omega_0}. \tag{6.8}$$

As a side note, assuming critical coupling with $Q_\mathrm{i} = 2Q_\mathrm{L}$ this equation simplifies to the Barkhausen relation $\Delta\varphi = 2Q_\mathrm{L}\Delta\omega$ [Rub09] in the literature. However, since critical coupling is often not the case in real measurements, we employ Eq. (6.8) and determine the prefactor by a linear fit of $\arg S_{21}$. The relation above is only valid if the sampling frequency is below the so-called Leeson frequency $\omega_\mathrm{L} = \omega_0/(2Q_\mathrm{L})$, which equals the linewidth (HWHM) of the resonator. Otherwise one does not measure frequency fluctuations but "instantaneous phase" fluctuations.
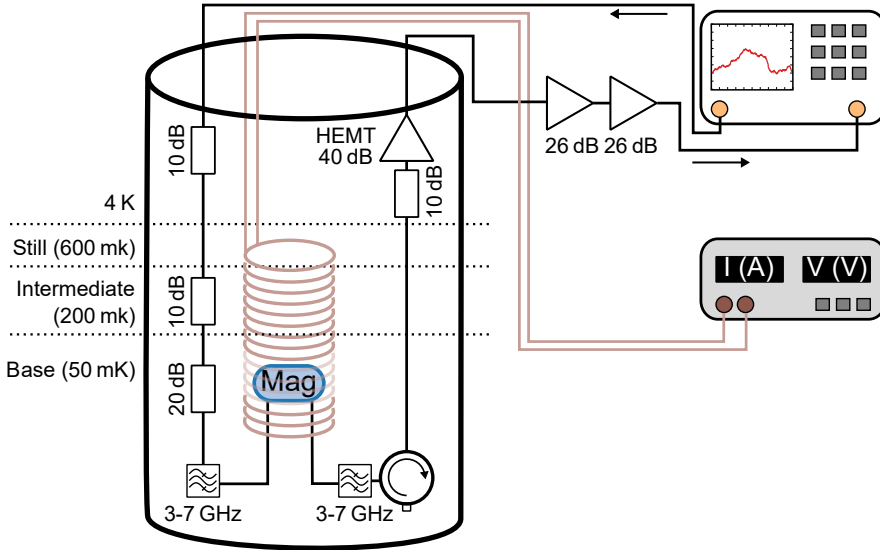
Figure 6.5: Implementation of the noise spectroscopy setup with the sample inside a cryostat. The microwave signal emitted by the vector network analyzer (VNA) is attenuated at the several stages of a cryostat before it reaches the magnetic material (a YIG-sphere mounted inside a solenoid coil) at the base stage. The transmitted signal is amplified by a high electron mobility transistor (HEMT) at the 4 K stage and again at room temperature before it is recorded by the VNA. The external bias field is controlled by a current source. From 70 K downwards, superconducting dc-cables are used going over into the solenoid coil, which is fixated at the still stage.

For more information, see Refs. [Bur13; RB10]. The above condition is fulfilled for all measurements in this work, by sampling frequencies $f_s < 1\,\mathrm{kHz}$.

6.3.3 Cryogenic Setup

So far, all the experiments in this work have been performed at room temperature. Now however, we want to find information about magnon coherence at temperatures below 1 K. Hence, we need to reach such low temperatures. In our case a "dry" dilution refrigerator makes this possible. The working principle of such a dilution refrigerator is explained, based on Ref. [EH05], in the following paragraphs.

The central part of such a dilution refrigerator is a closed circulation of a ^{3}He/^{4}He mixture. This mixture exhibits a special feature below 870 mK: a spatial phase separation of a ^{3}He-rich phase and a diluted phase with only a small amount of ^{3}He within the ^{4}He. (Below 200 mK the ^{3}He-rich phase is almost pure). A cooling process can now happen because crossing the phase boundary from the pure phase

into the diluted phase costs energy, which will be drawn from the environment. The standard technical realization of this phase transition is as follows: The two phases of the mixture are separated in the mixing chamber, which is installed on the base plate and will hence have the coldest temperature. The mixing chamber is connected to the still, fixated on the still plate, in a way that ^{3}He from the diluted phase will flow from the mixing chamber into the still, because of an osmotic pressure produced by pumping at the still via a room temperature pump. This pumping process exclusively evaporates ^{3}He creating a concentration gradient. Since ^{3}He is now missing in the dilute phase, it has to cross the boundary from the pure phase. Of course the previously pumped ^{3}He has to be reintroduced into the mixing chamber from room temperature, where it is also cleaned in a nitrogen cold trap. On the way back the ^{3}He is condensed and further cooled by exchanging heat with the ^{3}He coming from the mixing chamber.

An every-day's life analogy illustrates this principle. Imagine, having water droplets on your skin after a shower or bath and standing in a room with open windows. The wind, playing the roll of the pumping process, will inevitably lead to the evaporation of the water on your skin by hitting the topmost molecules of the droplets. Similar to the explanation above, crossing the phase boundary between liquid and gaseous is energy-costly, the energy is drawn from your body, and you will feel cold.

A well functioning cryostat requires a vacuum of $P < 1 \times 10^{-5}$ mbar to reduce unwanted heat exchange. Moreover the cold temperature is reached over several stages, which are all thermally isolated. A pulse tube cooler in combination with a Joule-Thompson valve provides the pre-cooling down to 1 K for dry cryostats.

The magnetic field biasing the FMR is generated by a superconducting solenoid coil, which is fixed at the still plate, giving the advantage of a reduced heat entry at the base plate due to ac-losses in the superconductor. The sample, of course, is mounted on the base plate.

The noise spectroscopy setup also has to be adjusted for cold temperatures. An implementation is depicted in Fig. 6.5. The microwave tone coming from room temperature is attenuated to reduce thermal photon noise and also to minimize the heat impact on the base stage. This attenuation takes place at three cryostat stages with attenuations of 10, 10 and 20 dB. As the signal has to be strongly attenuated, we also need to amplify it again before recording. We employ a low noise high electron mobility transistor (HEMT) for this purpose. An additional attenuator is installed before the HEMT to prevent compression of the amplifier. The sample is further shielded from other noise sources by band pass filters and circulator

reducing the impact of HEMT noise radiated backwards. The signal is additionally amplified with a pair of room temperature amplifiers before it enters the VNA.

6.3.4 Parasitic Noise Sources

Interpreting noise spectra can be difficult, especially since noise arising in the measurement setup can cover that of the sample. For a proper analysis, a correct assignment of the measured noise spectra to the respective devices in the setup is crucial. In our case three different noise sources have to be considered: sample noise, HEMT noise and current noise. I will revise the behavior of amplifier phase noise, as explained in Ref. [BR12] before presenting the measurement procedure for current noise, which directly translates to FMR frequency noise.

Microwave Amplifier Noise

Friis formula [Poz12] gives an expression for the equivalent noise temperature T_e of an amplifier chain, i.e., the temperature that would produce the amount of Johnson Nyquist noise

$$T_e = T_1 + \frac{T_2}{G_1} + \frac{T_3}{G_1 G_2} + ...,$$ (6.9)

with single noise temperatures T_i and gains G_i. It follows that the first amplifier stage determines the total noise temperature, under the condition of sufficient gain. Hence, we can confine our discussion to the HEMT amplifier in our setup. Microwave amplifier noise has a power dependence that requires a careful comparison of measurements with different input power to the HEMT. For instance, on- and off-resonant measurements of a microwave resonator with individual transmission amplitudes may show different noise levels but may both arise due to HEMT noise.

Two distinct mechanisms are responsible for amplifier noise. One mechanism leads to white noise, which scales inversely with input power P_0, whereas the other, seen as flicker noise, does not. According to Ref. [BR12] the HEMT noise PSD is given by:

$$S_{\varphi,\text{HEMT}} = \frac{C}{f} + \frac{kT_e}{P_0}$$ (6.10)

Without any input, an amplifier produces white noise, as proven by Nyquist [Nyq28], and follows a PSD of $S \propto k_B T_e$. The equivalent noise temperature is device and ambient temperature specific. The amplifier adds a certain but constant amount of noise to the actual input signal. A conversion to phase noise then gives the inverse scaling with power. An intuitive explanation can be gained by considering

the complex plane. The greater the input power, the further away is the signal from the origin and the effect of small fluctuations is reduced. We can use the arcsin function to obtain the angle in the complex plane. Linearizing it yields the inverse proportional dependence on input power.

Flicker noise, however, arises due to near-dc $1/f$ processes, which are upconverted to ω_0 with the input signal. This noise process scales linearly with input power. A conversion to phase noise however then exactly compensates this scaling and the $1/f$ part in the phase noise PSD is independent of input power [Bou+98]. Hence, by considering these power-dependencies, we can evaluate the HEMT phase noise PSD. An off-resonant noise measurement ($\omega_0 \neq \omega_r$) with different VNA output powers will reveal a constant $1/f$ part, which gives a lower limit for the observable sample noise.

Current Noise

The resonance frequency of the Kittel mode is controlled by the external bias field, $\omega_r = \gamma B$, which in turn is set by the bias current. This relation however means that current fluctuations are directly proportional to frequency fluctuations, $\Delta f \propto \Delta I$. To exclude current fluctuations as a trivial explanations for the measurement, the current noise PSD as produced by the source is measured independently.

We obtain the PSD by using an FFT spectrum analyzer and measuring the voltage drop over an resistor inserted in series to the solenoid. An RC high-pass with a cutoff frequency of $f_c = 0.032\,\mathrm{Hz}$ removes the DC part of the signal and thereby increases the sensitivity to small fluctuations, as otherwise the dynamic range would limit the measurement. We find a $1/f$ current noise with amplitude of $S_{\Delta I}(1\,\mathrm{Hz}) = 6 \times 10^{-13}\,\mathrm{A^2/Hz}$, which translates to a frequency noise PSD of $S_{\Delta f}(1\,\mathrm{Hz}) = 1 \times 10^6\,\mathrm{Hz^2/Hz}$. As we will see in Sec. 6.4, this value is lower than the measured phase noise of the sample and we can conclude that current noise does not profoundly affect our measurements.

6.4 Frequency Noise and Linewidth

6.4.1 Linewidth of a YIG-Sphere at mK-Temperatures

Noise spectroscopy, in our case, is best performed on a single resonator. In a coupled system, such as the CMP, frequency noise of either resonator would directly affect its coupled counterpart, compare Eq. (2.14). This would make it difficult to disentangle
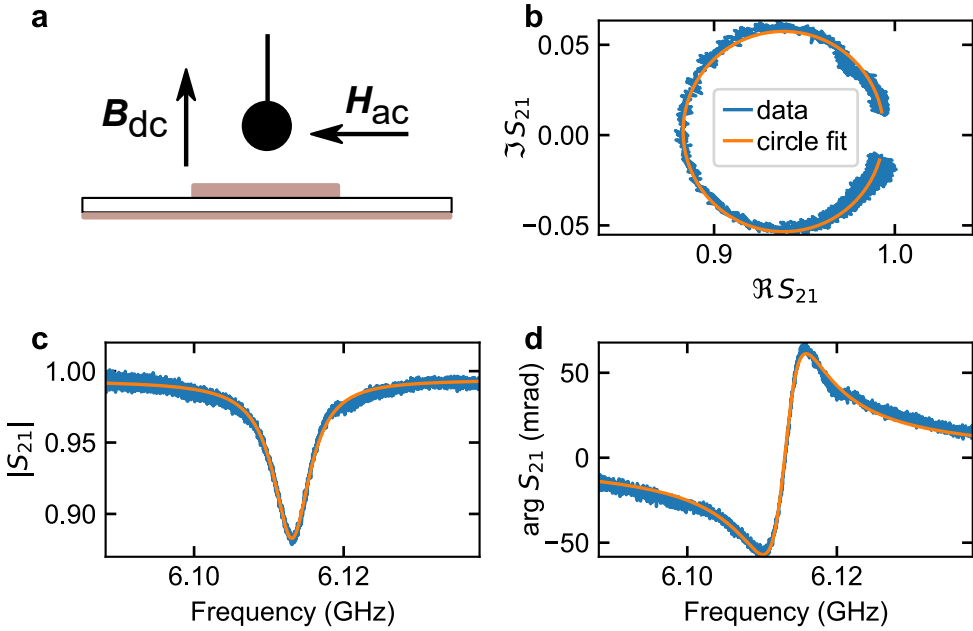
Figure 6.6: S_{21} response and circle fit of the ferromagnetic resonance. a Sketch of the sample geometry. **b** The scattering data in the complex plan draws a resonance circle. **c** Amplitude of the scattering data shows the characteristic resonance dip with a small amplitude as a telltale sign of an under-coupled resonance. **d** Phase response follows the characteristic arctan behavior. The onset of a higher FMR mode is visible 5 MHz apart from the Kittel mode and may weakly interact. Blue lines describes the background-corrected measurement data at temperature $T = 50$ mK and drive power $P = -90$ dBm. Solid orange lines represent the circle fit, yielding the internal linewidth for further evaluation.

the influence of the cavity on the magnon and vice versa. But before performing the noise spectroscopy, we want to examine the linewidth dependence on power and temperature to see the possible influence of TLS. Recall from Sec. 2.5 that previous measurements indicating TLS in magnons have either been performed where the magnetic system was coupled to a (copper) cavity or on a YIG thin film; however not yet on a sphere.

Sample

For the following experiments, we choose a YIG sphere with diameter $d = 0.2$ mm positioned over a microstrip transmission line. The FMR can then be described by a notch-type configuration (see Sec. 3.2). A schematic of the sample as well the measured S_{21} values are depicted in Fig. 6.6. From this response, we can conclude
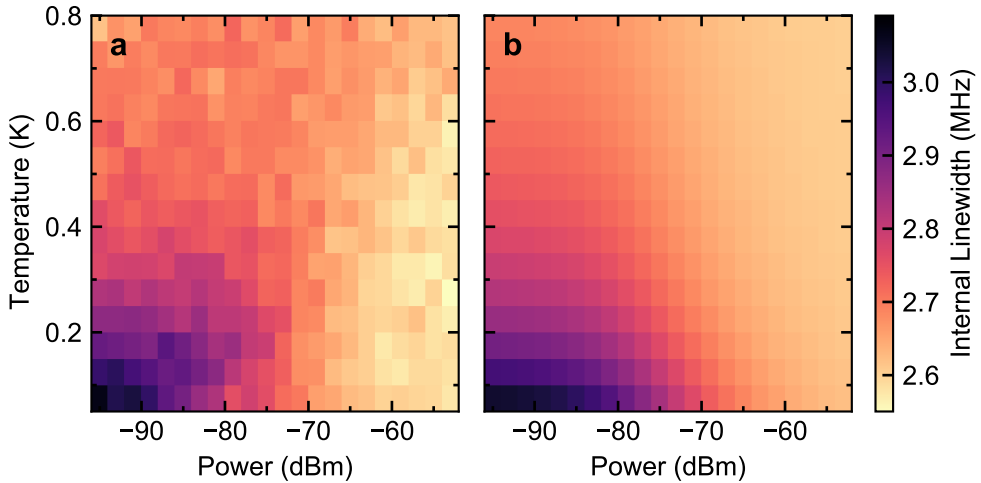
Figure 6.7: Linewidth reduction depending on power and temperature in the mk-region. Internal linewidth (HWHM) of the measured data as extracted by the circle fit is shown in Panel **a**, and contrasted to theory in **b**. Here, the data are generated with the standard TLS formula Eq. (2.24), where a temperature dependence of the critical power is neglected. The parameters are chosen manually with $k_0 = 0.5\,\text{MHz}$, $k_{\text{off}} = 2.6\,\text{MHz}$ and $P_c = -70\,\text{dBm}$. A difference in the two plots is visible in the intermediate region suggesting a scaling of P_c with temperature. At high temperatures in the measured data, another loss mechanism independent of TLS may start to become visible.

that the sample is strongly under-coupled ($Q_i = 995$ to 1200, $Q_c \approx 9125$), which flattens the slope in the phase response and hence leads to lower phase noise (assuming equal frequency noise, see Sec. 6.3.2) but also reduces the HEMT white noise, since more photons reach the amplifier, see Sec. 6.3.4).

Linewidth Measurement

We measure the FMR linewidth for excitation powers of $-96\,\text{dBm}$ to $-52\,\text{dBm}$, where the cable attenuation inside and out of the cryostat is estimated to be $20\,\text{dB}$. The temperature is swept over a range from $50\,\text{mK}$ to $800\,\text{mK}$. The FMR microwave scattering data, S_{21}, are corrected by the complex baseline data with a detuned FMR mode. Subsequently, the corrected data are circle-fitted [Pro+15] and the internal Q-factor and resonance frequency are extracted which yields the internal linewidth (HWHM). Figure 6.7a shows a 2D color plot of the linewidth depending on power and temperature. For our sphere, a decrease of the linewidth with increasing power and temperature is observed. However, this decrease is smaller than in previous works, only on the order of $0.5\,\text{MHz}$ as compared to our previous work [Pfi+19] with a change of $1\,\text{MHz}$. Here, we refrain from a more quantitative analysis, which

can be found in Refs. [Pfi+19; Kos+19]. Moreover, the results from fits to the TLS formula, Eq. (2.24), strongly depend on the fitting procedure and respective model, (see Appendix C.1 for a more detailed discussion on the problem.) Instead, we simply contrast the measured data to numerical values following the linewidth contribution according to Eq. (2.24), with manually chosen parameters (Fig. 6.7b). A difference from this model is visible in the behavior for intermediate powers and temperatures. For the numerically generated data, a constant P_c with temperature is assumed. However, the critical power depends on the TLS coherence, giving a possible temperature dependence. Indeed, Schickfuss *et al.* [VH77] observed such a temperature dependent P_c in glasses. A similar behavior was found for the linwewidth in magnons [Kos+19] and may also explain the described discrepancy of our data.

At temperatures around 700 mK temperature peak processes due to impurities [Sei64; CTT65] may already begin, covering up the small power dependence observed at lower temperatures. Furthermore, the power independent linewidth contribution, 2.5 MHz is high compared to previous works. This may be due to a badly polished sphere [SLK61; Nem64] or eddy currents induced in the transmission line [MK15; Kos16] (see Sec. 2.5). This high constant linewidth may already indicate a minor role of TLS in our sample.

In summary, we observed a power and temperature dependent linewidth decrease. Although this decrease is smaller than previously reported, it may be ascribed to a TLS model with a temperature dependent P_c. A quantitative statement as well as a final answer about the loss mechanisms, however, is difficult to draw from the data. In the next section, we will apply noise spectroscopy, in order to have a complementary tool to the simple linewidth evaluation.

6.4.2 Frequency Noise: Power and Temperature Dependence

Employing the constant wave mode of a VNA with drive frequency equal to the resonance frequency, we measure the phase response over time, as explained in Sec. 6.3.1. The phase fluctuations are converted to frequency fluctuations (sec. 6.3.2) and subsequently the frequency noise PSD is calculated with Welch's algorithm [Wel67]. This procedure is repeated for drive powers of -100 dBm to -60 dBm and in a temperature range of 50 mK to 800 mK, as well as for two different FMR frequencies, around 4 GHz and 6 GHz. In Fig. 6.8 three PSDs measured at $\omega_r/2\pi = 6$ GHz are shown exemplary. The PSDs are also compared to the phase noise produced by the HEMT, (scaled with the same factor of the conversion to frequency noise), and the equivalent frequency noise produced by fluctuations in the current source. We can make the following observations:
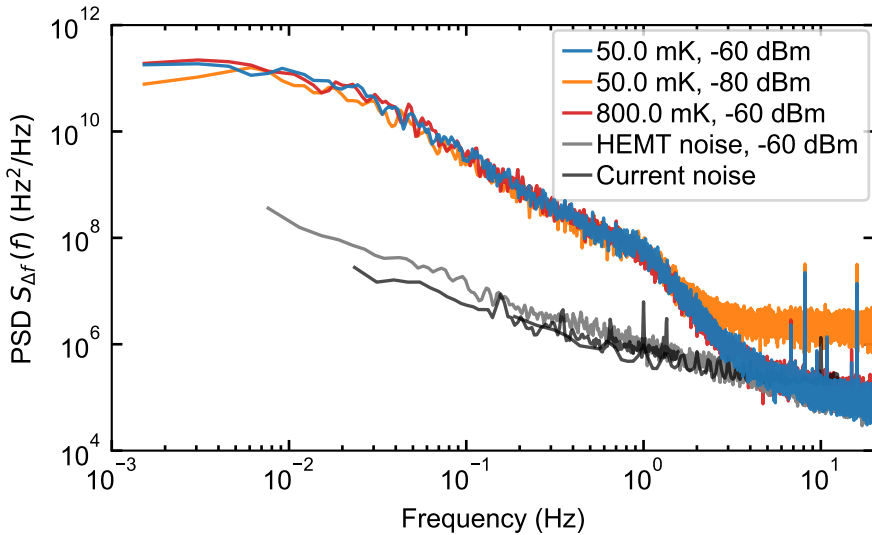
Figure 6.8: Frequency noise power spectral density (PSD) for different input powers and temperatures. The colored lines exemplarily depict three FMR frequency noise PSDs calculated from time traces recorded at $\omega_r/2\pi = 6.11\,$GHz of phase fluctuations according to Welch's method. No dependence of power and temperature is visible. Grey and black lines show HEMT phase noise and current noise converted into their frequency noise equivalent, respectively. At frequencies above $2\,$Hz an increase in the white noise baseline of the HEMT is visible for the orange curve.

- The frequency noise PSD measured on magnon resonance is higher than either HEMT noise and current noise. This suggests that the observed frequency fluctuations indeed arise in the sample.[1]

- The magnon noise PSD does not follow a simple $1/f$ form, but rather a Lorentzian for frequencies below $1\,$Hz. For higher frequencies, a steep decrease is visible before reaching the HEMT noise baseline.

- No power- and temperature dependence of the noise PSD can be found. The low-frequency noise part below $1\,$Hz is identical for both observed resonance frequencies but differs from there on. See Appendix C.3 for more data.

We recall that for superconducting resonators the impact of a TLS produces a $1/f$ decay in the noise PSD, the noise amplitude at $1\,$Hz scales with a square root power dependence, and temperature also influences the data, depending on the interaction between the TLS [Bur+14; MCL19]. Since the measured magnon noise

---

[1] The curious reader who wonders about fluctuations in the earth magnetic field can find a rough comparison in Appendix C.2.
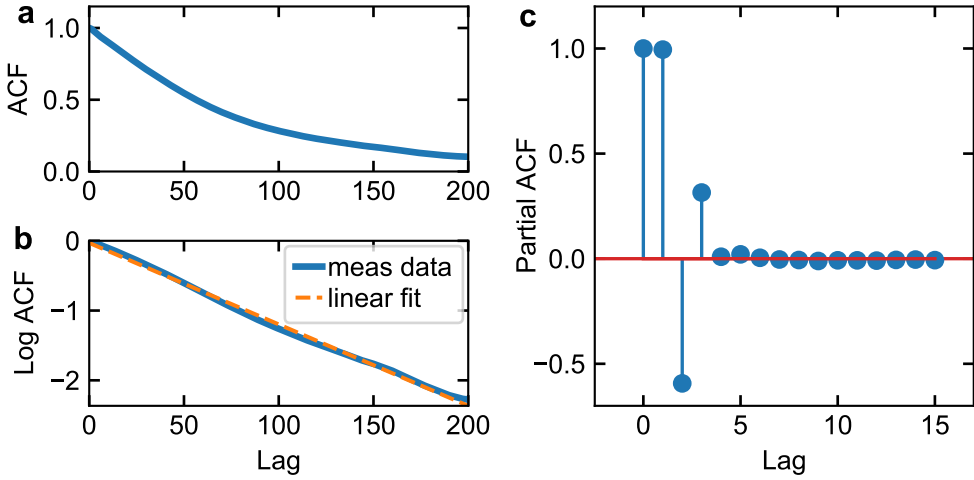
Figure 6.9: Autocorrelation (ACF) and partial autocorrelation (PACF) of magnon frequency fluctuations. The ACF **a** calculated from the time trace of frequency fluctuations reveals an exponential-like decay with small deviations from the pure form visible in the logarithmic ACF **b**. The PACF of the frequency fluctuations is shown in **c**. A partial correlation exists only up to lag 3 suggesting the fluctuations can be described by an AR(3) model. Before calculating the ACF and PACF a post-averaging was performed to filter out unwanted oscillation and HEMT white noise, resulting in an artificial sampling rate of $f_s = 8\,\text{Hz}$.

PSD does not exhibit any of these features, we can conclude that, despite seeing a linewidth reduction, the main noise mechanism for magnons at mK-temperature is *not* caused by TLS. However, it is impossible to infer that there are no TLS participating. The TLS part of the PSD could simply be too small to show in the data. For instance, the frequency noise in superconducting resonators is found to be around $S(1\,\text{Hz}) = 1 \times 10^4\,\text{Hz}^2/\text{Hz}$ to $1 \times 10^5\,\text{Hz}^2/\text{Hz}$ [Bur+14], which is well below the observed noise power in the FMR case.

Moreover, the functional form of the PSD taken at $\omega_r/2\pi \approx 6.11\,\text{GHz}$ with its steep decrease at $1\,\text{Hz}$ is puzzling and requires us to employ time series analysis for more details.

6.4.3 Frequency Noise: Time Series Analysis

In this section, we will investigate the measured frequency noise by analyzing the time trace data. Our objective is to find a model describing the measured noise data leading to a closed form for the PSD. We choose the data recorded with $-60\,\text{dBm}$ at $50\,\text{mK}$, which has the lowest HEMT baseline. However, compared to the data

Table 6.1: Estimated values of the AR(3) process describing the frequency noise time trace, after post-averaging leading to a sampling rate of $f_s = 8\,\text{Hz}$.

	σ (kHz)	a_1	a_2	a_3
Yule-Walker	5.284	1.764	-1.079	0.309
Burg	5.275	1.766	-1.083	0.311

presented in the previous section, we first perform a post averaging of the time trace, giving an artificial sampling rate of $f_s = 8\,\text{Hz}$, to filter out HEMT noise and periodic oscillations.

Parameter Estimation

Taking the new averaged time trace, we calculate the ACF (Fig. 6.9a), which shows an exponential-like decay. Such a decay, could be expected due to the Lorentzian form at low frequencies in the PSD. Recall that the PSD is the Fourier transform of the ACF. However, we also saw a steeper decay above $1\,\text{Hz}$ indicating deviations from a single exponential. And indeed a log plot of the ACF (Fig. 6.9b) shows small oscillations added to the straight line.

From the discussion in Sec. 6.2.3, we also know that an exponential decay in the ACF is untypical for an MA process but points towards an AR process. The PACF (Fig. 6.9c) shows values distinctly different from zero at three time lags, apart from zero. Hence, the measured and averaged noise time trace is estimated by an AR(3) Process. We note that the estimated order depends on the chosen (artificial) sampling rate, see Appendix C.4 for a more detailed discussion.

In the next step, we use the Yule-Walker equations to estimate the parameters of the AR(3) process and compare them with the Burg algorithm (Sec. 6.2.2). The estimated values are stated in Tab. 6.1 and yield an exponential-like decay of a one-time shock, indicating some form of friction in the system. With the estimated AR parameters, we can also generate a new time trace and compare the features of the generated one with the actual one. A simple visual analysis shows that both exhibit small fluctuations, occurring with the same high frequency, and the occasional big jumps, see Fig. 6.10b.

PSD Calculation

From the generated time trace data we can also calculate the PSD employing Welch's algorithm again and find a striking agreement with the measured data,

see Fig. 6.10b. Moreover, employing the closed form for the spectral density of an AR(p) process, Eq. (6.5) and rewriting it for third order, we find

$$S(f) = \frac{2\sigma^2 \delta t}{1 + \alpha_{123} + 2\alpha_1 \cos(2\pi\delta t \, f) + 2\alpha_2 \cos(4\pi\delta t \, f) - 2\alpha_3 \cos(6\pi\delta t \, f)}, \quad (6.11)$$

with $\delta t = 1/f_s$ as sampling time. The prefactors α_i are sums of the estimated AR parameters a_i: $\alpha_{123} = a_1^2 + a_2^2 + a_3^2$, $\alpha_1 = -a_1 + a_1 a_2 + a_2 a_3$, $\alpha_2 = -a_2 + a_1 a_3$, $\alpha_3 = a_3$.

Comparing the closed form of the PSD with the measured and generated data, we find an excellent agreement. Hence, we can conclude that the measured, and post-averaged, magnon frequency noise can be well modeled by an AR-Process with some form of mean-reverting process and without any oscillations of one-time shocks.

6.5 Discussion

In conclusion, we first investigated the Kittel-mode linewidth of a YIG sphere at mK temperature before performing a frequency noise spectroscopy. The linewidth data show a decrease with increasing power and temperature, pointing towards loss due to TLS. However, it is difficult to draw an accurate conclusion, since it strongly depends on the chosen fitting procedure.

The power spectral densities obtained by noise spectroscopy do not show a $1/f$ decay, no power- and no temperature dependence in the observed range, which rules out TLS as the main source of frequency fluctuation. Still, some influence due to TLS may be there but may be overlaid by another process.

The functional form of the PSD cannot be described by a simple power law, which led us to employ a time series analysis. We found that an AR(3) process best models the post averaged data with a sampling frequency of 8 Hz. The higher order AR process indicates a mean-reverting mechanism, which is more complicated then a pure damped Brownian motion (Ornstein-Uhlenbeck process). An explanation may be several interleaved noise processes that occur on different time scales [MS98]. Below 0.1 Hz, the data can be described by an AR(1) process (Appendix C.4), corresponding to the observed Lorentzian in the PSD and rendering higher order parameters unimportant in this particular frequency range.
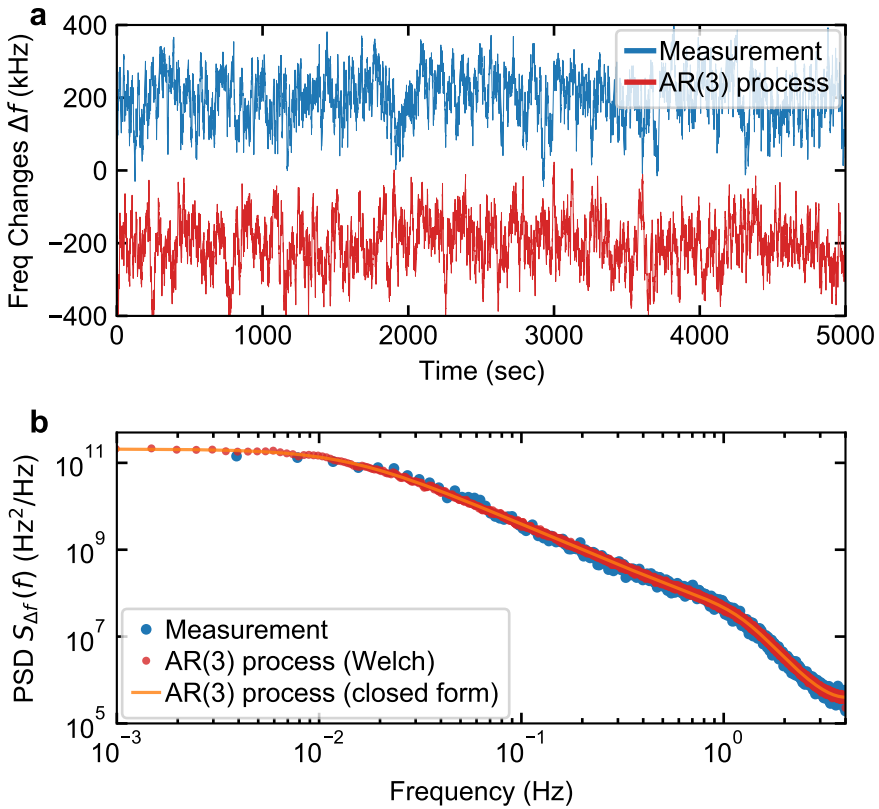
Figure 6.10: Comparison of AR(3) process with measured FMR fluctuations. a Generated time trace based on an AR(3) process exhibits similar feature as measured (and averaged) data regarding peak to peak values and amplitude distribution of the fluctuations. **b** The qualitative similarity is confirmed by identical power spectral densities calculated according to Welch's algorithm and the closed form of the spectral density for an AR(3) process.

We can compare the results to other magnetic noise investigations in the literature; first of all, the amplitude noise of a magnon wave guide measured at room temperature [Rum+19]. In this work, the PSD shows a Lorentzian as well, which however arises due to random telegraphic noise instead of a damped Brownian motion. The contrary results suggest different noise mechanisms for amplitude noise in wave guides and frequency noise of magnetic sphere in notch type configuration. Noise properties have also been examined for magnetic tunnel junction oscillators. There as well, a Lorentzian PSD is found [Hou+09; Qui+10], but for the (instantaneous) phase noise instead of frequency noise. For these systems, the Lorentzian is a consequence of white noise added to the cosine argument in the oscillator function. Furthermore and in contrast to magnetic flux noise in superconducting devices,

which are most likely caused by surface spins and magnetic moments of trapped electrons [KDC07; Sen+08; Kum+16; KFE16], magnon frequency noise does not show a $1/f$ decay and must hence arise from a distinctly different process.

Searching for the origin of magnon frequency noise, we can start by considering the Kittel formula [Kit48] for non-spherical geometries. There, a dependence on the saturation magnetization M_s via demagnetization factors N_i comes into play:

$$\omega_r = \gamma \sqrt{\left(H_e + (N_x - N_z)M_s\right)\left(H_e + (N_y - N_z)M_s\right)}. \tag{6.12}$$

The different quantities in Eq. (6.12) imply possible suspects for frequency noise. Fluctuations may occur in the magnetic field due to a fluctuating environment in the crystal, which has been considered by existing theoretical works [KH70; MS98; For+09]. However, the fluctuations have always been assumed as white noise, which is in contrast to the results of this work.

Fluctuations may also take place in the saturation magnetization, i.e., the number of aligned spin changes randomly. This could be again due to a fluctuating magnetic crystal field. Considering Eq. (6.12), we see that magnetization noise propagates via the demagnetization factors into the resonance frequency. Although for a sphere, the demagnetization factors cancel each other out, the saturation magnetization still affects the resonance frequency via YIG's magnetic anisotropy [Lee+16]. This hypothesis of magnetization fluctuations could be tested by performing a noise spectroscopy on a thin-film magnonic material, instead of a sphere, and for different orientations towards the external field.

Moreover, through spin noise spectroscopy [Zap13; SP16] a spatial spread of the g-factor, which is included in γ in Eq. (6.12), was found in semiconductor devices [Ber+13]. Such a spread is linked to the inhomogeneous spin dephasing rate. Although this link arises from a local shifting of the band structure due to the dopands in semiconductors, one should not directly exclude a comparable mechanism for spin waves in insulating materials, such as YIG.

Still more research is necessary to identify the origin of TLS and their coupling to the uniform mode, as well as to develop a microscopic theory of magnon noise mechanism. Yet, the presented data and the chosen evaluation method may help to reach this goal.

7 Conclusion and Outlook

Within the framework of this work, we set out to obtain a control over different CMP properties, and successfully demonstrated a spectroscopic manipulation of the coupling strength as well as a dynamic change of the CMP mode composition in the time domain. Additionally, magnon frequency noise at mK temperatures was observed as an initial effort in the quest of controlling the loss rate.

By experimentally implementing [Bov+20] a two-tone scheme as proposed in Ref. [GSX18], we showed how the coupling strength can be controlled depending on two parameters, i.e., the phase difference between and amplitude ratio of magnon and cavity signal. Choosing in-phase drive tones increases the repulsive coupling strength by an amount determined via the amplitude ratio, whereas anti-phase tones, decrease the coupling strength. By choosing an amplitude ratio for anti-phase tones beyond unity, one can prepare the CMP in the level attraction regime, where the two eigenmodes coalesce. This regime has been more extensively studied in optical systems [MA19; Ber+18] but has now also found its way into CMP research [WH20]. Our work contributed to this new field of dissipative coupling in the CMP by introducing an in-situ tunability option. No mechanical change of the sample is required. Moreover, this tuning scheme sets itself apart by a continuous parameter space of the phase difference allowing for a coexistence of level attraction and repulsion.

In the future, this two-tone control scheme may help push the CMP into the deep strong coupling regime, which would inherently not be possible for the CMP. Additionally, level attraction has theoretically been linked to entanglement [Yua+20], opening new ways for CMP based quantum computing. The presented work could be continued by investigating level attraction in the single magnon regime and from the time-domain perspective, which could verify the theoretical predictions of Ref. [Yua+20].

Adapted from superconducting qubit experiments, we presented a time-domain setup to phase-coherently manipulate both CMP subsystems in the ns-range while recording the reflected energy from the cavity [Wol+20]. We used the same control parameters as in our spectroscopic experiment, but employed short coherent pulses. With such pulses, we were able to prepare the CMP, biased to its crossing point, in

any superposition of its eigenmodes. We also extended this control to the dynamic case, altering the CMP modes within a single decay as well as extracting the total energy from the system. The experimental results were validated by an analytically derived expression for the mode composition with respect to the control parameters and numerical simulations. Together, these results underpinned the CMP coupling models [Bai+15] from the time domain perspective.

The described control technique, yet performed at room temperature, may pave the way for a future encoding on qubit states in magnons. A shared anharmonicity from a coupling to a superconducting qubit, similar to experiments with superconducting resonators [Hof+08] would allow for such an encoding. This would require more advanced pulse schemes than presented here but could be easily achieved with our setup. Although the coherence times of magnons are short compared to superconducting resonators, additional options are given by a magnon gradient memory [Zha+15], for instance, and more importantly by the possibilities of magnon radiofrequency-to-light converters [His+16; Zha+16; Osa+16; Hai+16]. It will still be a long way to reach a suitable conversion efficiency. But from there on, a functioning quantum internet [Kim08] based on information transfer via the CMP and light signals would be possible.

Contributing to the goal of improving magnon coherence, we performed linewidth measurements and an FMR noise spectroscopy at mK temperatures. The linewidth data revealed a power and temperature dependence, which has been previously reported and attributed to TLS. In contrast, the noise spectroscopy data is power- as well as temperature independent and can therefore not be attributed to TLS. Moreover, the PSD has a function form close to a Lorentzian but with a steep decrease at 1 Hz. A subsequent time series analysis uncovered that the noise data can be best described by an AR(3) process (under a sampling rate of 8 Hz). The higher order parameters suggest a more complicated process than a simple damped Brownian motion. Most likely several noise processes with different time scales play a role. A microscopic theory explaining these noise processes is yet to be developed. The presented and applied time series analysis, however, may also be useful for noise evaluation in other fields, e.g., spin noise spectroscopy, spin current noise and spin torque oscillator noise, yielding information about the involved timescales of the systems' noise.

Future tasks for a more detailed understanding of possible FMR noise mechanisms may be investigating the effects of sample size and surface polishing, which would point towards the location of noise sources. Additionally, different materials can be observed, predominantly LiFe. Spheres fabricated from this material have a non-monotonous dispersion showing an extremum [Gor+18] and hence an insensitivity

to field fluctuations. Data taken at such an insensitivity point would help in confining the fluctuating physical quantities.

For even more sophisticated noise spectroscopy experiments, a qubit could be employed. Superconducting qubits have proven themselves as working sensors for electromagnetic fields [Sch+18; Kri+20], magnon numbers [Lac+17], environmental flux noise [Byl+11; Yan+13] and TLS noise [Lis+16; Lis+19]. Similar to experiments probing fluctuations of a driven superconducting resonator coupled to the qubit [Yan+18], frequency as well as occupation number fluctuations of an indirectly coupled magnon [Tab+15] would shift the qubit frequency. These shifts could be read out by spin locking sequences [Ith+05; Yan+13], for examples. The results could be cross-checked by an inductive qubit magnon coupling, utilizing a planar approach of the hybrid system [Sch20] and an in-plane magnetic field configuration [Sch+19]. The magnetic field produced by the ferromagnetic material affects the magnetic flux in the SQUID loop of the tunable qubit and hence also leads to frequency fluctuations, which could be again measured with the spin locking technique.

As a final conclusion, with the demonstration of controlling the coupling strength and different CMP modes, we hope to have opened new paths to advance computational CMP research. The performed noise spectroscopy is one more experimental step towards improving magnon coherence, with which hybrid magnonics could be pushed closer to functional applications.

Bibliography

[All+14]   R. Alléaume, C. Branciard, J. Bouda, T. Debuisschert, M. Dianati, et al.: *Using Quantum Key Distribution for Cryptographic Purposes: A Survey*. Theoretical Computer Science. Theoretical Aspects of Quantum Cryptography – Celebrating 30 Years of BB84 **560** (2014), 62–81. DOI: 10.1016/j.tcs.2014.09.018 (cit. on p. 1).

[AHV72]   P. w Anderson, B. I. Halperin, and c. M. Varma: *Anomalous Low-Temperature Thermal Properties of Glasses and Spin Glasses*. The Philosophical Magazine: A Journal of Theoretical Experimental and Applied Physics **25** (1972), 1–9. DOI: 10.1080/14786437208229210 (cit. on p. 17).

[AE15]   A. S. G. Andrae and T. Edler: *On Global Electricity Usage of Communication Technology: Trends to 2030*. Challenges **6** (2015), 117–157. DOI: 10.3390/challe6010117 (cit. on p. 1).

[Aru+19]   F. Arute, K. Arya, R. Babbush, D. Bacon, J. C. Bardin, et al.: *Quantum Supremacy Using a Programmable Superconducting Processor*. Nature **574** (2019), 505–510. DOI: 10.1038/s41586-019-1666-5 (cit. on p. 2).

[Bai+15]   L. Bai, M. Harder, Y. P. Chen, X. Fan, J. Q. Xiao, and C.-M. Hu: *Spin Pumping in Electrodynamically Coupled Magnon-Photon Systems*. Physical Review Letters **114** (2015), 227201. DOI: 10.1103/PhysRevLett.114.227201 (cit. on pp. 2, 5, 10–12, 37, 57, 62, 88).

[Bar48]   M. S. Bartlett: *Smoothing Periodograms from Time-Series with Continuous Spectra*. Nature **161** (1948), 686–687. DOI: 10.1038/161686a0 (cit. on p. 65).

[Bay+17]   A. Bayer, M. Pozimski, S. Schambeck, D. Schuh, R. Huber, D. Bougeard, and C. Lange: *Terahertz Light–Matter Interaction beyond Unity Coupling Strength*. Nano Letters **17** (2017), 6340–6344. DOI: 10.1021/acs.nanolett.7b03103 (cit. on p. 14).

[Ber+18]   N. R. Bernier, L. D. Tóth, A. K. Feofanov, and T. J. Kippenberg: *Level Attraction in a Microwave Optomechanical Circuit*. Physical Review A **98** (2018), 023841. DOI: 10.1103/PhysRevA.98.023841 (cit. on pp. 40, 44, 87).

[Ber+13]   F. Berski, H. Kuhn, J. G. Lonnemann, J. Hübner, and M. Oestreich: *Ultrahigh Bandwidth Spin Noise Spectroscopy: Detection of Large g-Factor Fluctuations in Highly-n-Doped GaAs*. Physical Review Letters **111** (2013), 186602. DOI: 10.1103/PhysRevLett.111.186602 (cit. on p. 86).

[Bho+19]   B. Bhoi, B. Kim, S.-H. Jang, J. Kim, J. Yang, Y.-J. Cho, and S.-K. Kim: *Abnormal Anticrossing Effect in Photon-Magnon Coupling*. Physical Review B **99** (2019), 134426. DOI: 10.1103/PhysRevB.99.134426 (cit. on pp. 3, 41).

[Bia+17]   J. Biamonte, P. Wittek, N. Pancotti, P. Rebentrost, N. Wiebe, and S. Lloyd: *Quantum Machine Learning*. Nature **549** (2017), 195–202. DOI: 10.1038/nature23474 (cit. on p. 1).

[Bla+04]   A. Blais, R.-S. Huang, A. Wallraff, S. M. Girvin, and R. J. Schoelkopf: *Cavity Quantum Electrodynamics for Superconducting Electrical Circuits: An Architecture for Quantum Computation*. Physical Review A **69** (2004), 062320. DOI: 10.1103/PhysRevA.69.062320 (cit. on pp. 2, 14).

[Blo46]   F. Bloch: *Nuclear Induction*. Physical Review **70** (1946), 460–474. DOI: 10.1103/PhysRev.70.460 (cit. on p. 18).

[BdWB02]   R. Bos, S. de Waele, and P. M. T. Broersen: *Autoregressive Spectral Estimation by Application of the Burg Algorithm to Irregularly Sampled Data*. IEEE Transactions on Instrumentation and Measurement, 51 (6) (2002). URL: https://repository.tudelft.nl/islandora/object/uuid%3A870559f7-f1e9-4968-83da-edd19485eaaf (cit. on p. 66).

[Bou+98]   V. Bouchiat, D. Vion, P. Joyez, D. Esteve, and M. H. Devoret: *Quantum Coherence with a Single Cooper Pair*. Physica Scripta **1998** (1998), 165. DOI: 10.1238/Physica.Topical.076a00165 (cit. on p. 77).

[BR12]   R. Boudot and E. Rubiola: *Phase Noise in RF and Microwave Amplifiers*. IEEE Transactions on Ultrasonics, Ferroelectrics and Frequency Control **59** (2012), 2613–2624. DOI: 10.1109/TUFFC.2012.2502 (cit. on p. 76).

[Bou+16]   J. Bourhill, N. Kostylev, M. Goryachev, D. L. Creedon, and M. E. Tobar: *Ultrahigh Cooperativity Interactions between Magnons and Resonant Photons in a YIG Sphere*. Physical Review B **93** (2016), 144420. DOI: 10.1103/PhysRevB.93.144420 (cit. on p. 14).

[Bov+20]   I. Boventer, C. Dörflinger, T. Wolz, R. Macêdo, R. Lebrun, M. Kläui, and M. Weides: *Control of the Coupling Strength and Linewidth of a Cavity Magnon-Polariton*. Physical Review Research **2** (2020), 013154. DOI: 10.1103/PhysRevResearch.2.013154 (cit. on pp. 3, 4, 13, 36–38, 42, 44, 51, 87, 111).

[Bov+19] I. Boventer, M. Kläui, R. Macêdo, and M. Weides: *Steering between Level Repulsion and Attraction: Broad Tunability of Two-Port Driven Cavity Magnon-Polaritons*. New Journal of Physics **21** (2019), 125001. DOI: `10.1088/1367-2630/ab5c12` (cit. on pp. 3, 4, 36, 37, 44).

[Bov+18] I. Boventer, M. Pfirrmann, J. Krause, Y. Schön, M. Kläui, and M. Weides: *Complex Temperature Dependence of Coupling and Dissipation of Cavity Magnon Polaritons from Millikelvin to Room Temperature*. Physical Review B **97** (2018), 184420. DOI: `10.1103/PhysRevB.97.184420` (cit. on pp. 16, 52).

[Box+15] G. E. P. Box, G. M. Jenkins, G. C. Reinsel, and G. M. Ljung: *Time Series Analysis: Forecasting and Control*. John Wiley & Sons, 2015. 709 pp. (cit. on pp. 64, 66, 68, 71).

[Bra18]   J. Braumüller: *Quantum Simulation Experiments with Superconducting Circuits* (2018). DOI: `10.5445/KSP/1000081315` (cit. on pp. 22–25).

[Bra+17] J. Braumüller, M. Marthaler, A. Schneider, A. Stehli, H. Rotzinger, M. Weides, and A. V. Ustinov: *Analog Quantum Simulation of the Rabi Model in the Ultra-Strong Coupling Regime*. Nature Communications **8** (2017), 779. DOI: `10.1038/s41467-017-00894-w` (cit. on p. 49).

[Bre+17] J. D. Brehm, A. Bilmes, G. Weiss, A. V. Ustinov, and J. Lisenfeld: *Transmission-Line Resonators for the Study of Individual Two-Level Tunneling Systems*. Applied Physics Letters **111** (2017), 112601. DOI: `10.1063/1.5001920` (cit. on pp. 63, 72).

[BDT05]   P. J. Brockwell, R. Dahlhaus, and A. A. Trindade: *Modified Burg Algorithms for Multivariate Subset Autoregression*. Statistica Sinica **15** (2005), 197–213. URL: `https://www.jstor.org/stable/24307247` (cit. on p. 71).

[Bur+14] J. Burnett, L. Faoro, I. Wisby, V. L. Gurtovoi, A. V. Chernykh, et al.: *Evidence for Interacting Two-Level Systems from the 1/f Noise of a Superconducting Resonator*. Nature Communications **5** (2014), ncomms5119. DOI: `10.1038/ncomms5119` (cit. on pp. 4, 63, 64, 81, 82).

[Bur+13] J. Burnett, T. Lindström, M. Oxborrow, Y. Harada, Y. Sekine, P. Meeson, and A. Y. Tzalenchuk: *Slow Noise Processes in Superconducting Resonators*. Physical Review B **87** (2013), 140501. DOI: `10.1103/PhysRevB.87.140501` (cit. on p. 63).

[Bur13]   J. Burnett: *High Prescision Readout of Superconducting Resonators*. 2013 (cit. on p. 74).

[Bur+19]   J. J. Burnett, A. Bengtsson, M. Scigliuzzo, D. Niepce, M. Kudra, P. Delsing, and J. Bylander: *Decoherence Benchmarking of Superconducting Qubits*. npj Quantum Information **5** (2019), 1–8. DOI: `10.1038/s41534-019-0168-5` (cit. on p. 19).

[Byl+11]   J. Bylander, S. Gustavsson, F. Yan, F. Yoshihara, K. Harrabi, G. Fitch, D. G. Cory, Y. Nakamura, J.-S. Tsai, and W. D. Oliver: *Noise Spectroscopy through Dynamical Decoupling with a Superconducting Flux Qubit*. Nature Physics **7** (2011), 565–570. DOI: `10.1038/nphys1994` (cit. on p. 89).

[Cao+19]   Y. Cao, J. Romero, J. P. Olson, M. Degroote, P. D. Johnson, et al.: *Quantum Chemistry in the Age of Quantum Computing*. Chemical Reviews **119** (2019), 10856–10915. DOI: `10.1021/acs.chemrev.8b00803` (cit. on p. 1).

[CKL93]   V. Cherepanov, I. Kolokolov, and V. L'vov: *The Saga of YIG: Spectra, Thermodynamics, Interaction and Relaxation of Magnons in a Complex Magnet*. Physics Reports **229** (1993), 81–144. DOI: `10.1016/0370-1573(93)90107-0` (cit. on pp. 15, 16).

[CGS11]   Y. D. Chong, L. Ge, and A. D. Stone: *P T -Symmetry Breaking and Laser-Absorber Modes in Optical Scattering Systems*. Physical Review Letters **106** (2011), 093902. DOI: `10.1103/PhysRevLett.106.093902` (cit. on p. 44).

[CSH14]   A. V. Chumak, A. A. Serga, and B. Hillebrands: *Magnon Transistor for All-Magnon Data Processing*. Nature Communications **5** (2014), 4700. DOI: `10.1038/ncomms5700` (cit. on p. 1).

[CTT65]   B. H. Clarke, K. Tweedale, and R. W. Teale: *Rare-Earth Ion Relaxation Time and G Tensor in Rare-Earth-Doped Yttrium Iron Garnet. I. Ytterbium*. Physical Review **139** (1965), A1933–A1943. DOI: `10.1103/PhysRev.139.A1933` (cit. on p. 80).

[Cle+10]   A. A. Clerk, M. H. Devoret, S. M. Girvin, F. Marquardt, and R. J. Schoelkopf: *Introduction to Quantum Noise, Measurement, and Amplification*. Reviews of Modern Physics **82** (2010), 1155–1208. DOI: `10.1103/RevModPhys.82.1155` (cit. on pp. 13, 22, 28–30).

[Dic54]   R. H. Dicke: *Coherence in Spontaneous Radiation Processes*. Physical Review **93** (1954), 99–110. DOI: `10.1103/PhysRev.93.99` (cit. on p. 12).

[EN90]   S. Elliott and P. Nelson: *The Active Control of Sound*. Electronics & Communications Engineering Journal **2** (1990), 127. DOI: `10.1049/ecej:19900032` (cit. on p. 60).

[EBB20]   M. Elyasi, Y. M. Blanter, and G. E. W. Bauer: *Resources of Nonlinear Cavity Magnonics for Quantum Information*. Physical Review B **101** (2020), 054402. DOI: 10.1103/PhysRevB.101.054402 (cit. on p. 2).

[EH05]   C. Enss and S. Hunklinger: *Low-Temperature Physics*. Berlin Heidelberg: Springer-Verlag, 2005. DOI: 10.1007/b137878 (cit. on pp. 18, 74).

[Flo+19]   G. Flower, M. Goryachev, J. Bourhill, and M. E. Tobar: *Experimental Implementations of Cavity-Magnon Systems: From Ultra Strong Coupling to Applications in Precision Measurement*. New Journal of Physics **21** (2019), 095004. DOI: 10.1088/1367-2630/ab3e1c (cit. on pp. 3, 14, 35).

[For+09]   J. Foros, A. Brataas, G. E. W. Bauer, and Y. Tserkovnyak: *Noise and Dissipation in Magnetoelectronic Nanostructures*. Physical Review B **79** (2009), 214407. DOI: 10.1103/PhysRevB.79.214407 (cit. on p. 86).

[Gao08]   J. Gao: *The Physics of Superconducting Microwave Resonators*. PhD thesis. California Institute of Technology, 2008. URL: http://resolver.caltech.edu/CaltechETD:etd-06092008-235549 (cit. on pp. 18, 19, 27, 72).

[Gao+07]   J. Gao, J. Zmuidzinas, B. A. Mazin, H. G. LeDuc, and P. K. Day: *Noise Properties of Superconducting Coplanar Waveguide Microwave Resonators*. Applied Physics Letters **90** (2007), 102507. DOI: 10.1063/1.2711770 (cit. on pp. 4, 19, 63, 72).

[Gir14]   S. M. Girvin: "Circuit QED: Superconducting Qubits Coupled to Microwave Photons". *Quantum Machines: Measurement and Control of Engineered Quantum Systems*. Ed. by M. Devoret, B. Huard, R. Schoelkopf, and L. F. Cugliandolo. Oxford University Press, 2014, pp. 113–256. DOI: 10.1093/acprof:oso/9780199681181.003.0003 (cit. on p. 31).

[Gis+02]   N. Gisin, G. Ribordy, W. Tittel, and H. Zbinden: *Quantum Cryptography*. Reviews of Modern Physics **74** (2002), 145–195. DOI: 10.1103/RevModPhys.74.145 (cit. on p. 1).

[Gor+14]   M. Goryachev, W. G. Farr, D. L. Creedon, Y. Fan, M. Kostylev, and M. E. Tobar: *High-Cooperativity Cavity QED with Magnons at Microwave Frequencies*. Physical Review Applied **2** (2014), 054002. DOI: 10.1103/PhysRevApplied.2.054002 (cit. on pp. 14, 48).

[Gor+18]   M. Goryachev, S. Watt, J. Bourhill, M. Kostylev, and M. E. Tobar: *Cavity Magnon Polaritons with Lithium Ferrite and Three-Dimensional Microwave Resonators at Millikelvin Temperatures*. Physical Review B **97** (2018), 155129. DOI: 10.1103/PhysRevB.97.155129 (cit. on pp. 36, 88).

[GSX18]   V. L. Grigoryan, K. Shen, and K. Xia: *Synchronized Spin-Photon Coupling in a Microwave Cavity*. Physical Review B **98** (2018), 024406. DOI: 10.1103/PhysRevB.98.024406 (cit. on pp. 3, 36–38, 87).

[Gro96]   L. K. Grover: *A Fast Quantum Mechanical Algorithm for Database Search. Proceedings of the Twenty-Eighth Annual ACM Symposium on Theory of Computing - STOC '96*. The Twenty-Eighth Annual ACM Symposium. Philadelphia, Pennsylvania, United States: ACM Press, 1996, pp. 212–219. DOI: 10.1145/237814.237866 (cit. on p. 2).

[Hai+16]   J. A. Haigh, A. Nunnenkamp, A. J. Ramsay, and A. J. Ferguson: *Triple-Resonant Brillouin Light Scattering in Magneto-Optical Cavities*. Physical Review Letters **117** (2016), 133602. DOI: 10.1103/PhysRevLett.117.133602 (cit. on pp. 2, 62, 88).

[Har+18]   M. Harder, Y. Yang, B. M. Yao, C. H. Yu, J. W. Rao, Y. S. Gui, R. L. Stamps, and C.-M. Hu: *Level Attraction Due to Dissipative Magnon-Photon Coupling*. Physical Review Letters **121** (2018), 137203. DOI: 10.1103/PhysRevLett.121.137203 (cit. on pp. 3, 13, 36, 41, 42, 44, 111).

[HGH16]   M. Harder, Y. Gui, and C.-M. Hu: *Electrical Detection of Magnetization Dynamics via Spin Rectification Effects*. Physics Reports. Electrical Detection of Magnetization Dynamics via Spin Rectification Effects **661** (2016), 1–59. DOI: 10.1016/j.physrep.2016.10.002 (cit. on p. 57).

[HH18]   M. Harder and C.-M. Hu: "Chapter Two - Cavity Spintronics: An Early Review of Recent Progress in the Study of Magnon–Photon Level Repulsion". *Solid State Physics*. Ed. by R. E. Camley and R. L. Stamps. Vol. 69. Academic Press, 2018, pp. 47–121. DOI: 10.1016/bs.ssp.2018.08.001 (cit. on pp. 2, 9, 11, 13, 28).

[Hee+17]   R. W. Heeres, P. Reinhold, N. Ofek, L. Frunzio, L. Jiang, M. H. Devoret, and R. J. Schoelkopf: *Implementing a Universal Gate Set on a Logical Qubit Encoded in an Oscillator*. Nature Communications **8** (2017), 94. DOI: 10.1038/s41467-017-00045-1 (cit. on p. 62).

[His+16]   R. Hisatomi, A. Osada, Y. Tabuchi, T. Ishikawa, A. Noguchi, R. Yamazaki, K. Usami, and Y. Nakamura: *Bidirectional Conversion between Microwave and Light via Ferromagnetic Magnons*. Physical Review B **93** (2016), 174427. DOI: 10.1103/PhysRevB.93.174427 (cit. on pp. 2, 88).

[Hof+08]   M. Hofheinz, E. M. Weig, M. Ansmann, R. C. Bialczak, E. Lucero, M. Neeley, A. D. O'Connell, H. Wang, J. M. Martinis, and A. N. Cleland: *Generation of Fock States in a Superconducting Quantum Circuit*. Nature **454** (2008), 310–314. DOI: 10.1038/nature07136 (cit. on pp. 2, 62, 88).

[HP40]   T. Holstein and H. Primakoff: *Field Dependence of the Intrinsic Domain Magnetization of a Ferromagnet*. Physical Review **58** (1940), 1098–1113. DOI: 10.1103/PhysRev.58.1098 (cit. on p. 7).

[Hou+09] D. Houssameddine, U. Ebels, B. Dieny, K. Garello, J.-P. Michel, B. Delaet, B. Viala, M.-C. Cyrille, J. A. Katine, and D. Mauri: *Temporal Coherence of MgO Based Magnetic Tunnel Junction Spin Torque Oscillators*. Physical Review Letters **102** (2009), 257202. DOI: 10.1103/PhysRevLett.102.257202 (cit. on p. 85).

[Hue+13] H. Huebl, C. W. Zollitsch, J. Lotze, F. Hocke, M. Greifenstein, A. Marx, R. Gross, and S. T. B. Goennenwein: *High Cooperativity in Coupled Microwave Resonator Ferrimagnetic Insulator Hybrids*. Physical Review Letters **111** (2013), 127003. DOI: 10.1103/PhysRevLett.111.127003 (cit. on pp. 2, 14).

[Ith+05] G. Ithier, E. Collin, P. Joyez, P. J. Meeson, D. Vion, et al.: *Decoherence in a Superconducting Quantum Bit Circuit*. Physical Review B **72** (2005), 134519. DOI: 10.1103/PhysRevB.72.134519 (cit. on p. 89).

[JC63]   E. T. Jaynes and F. W. Cummings: *Comparison of Quantum and Semiclassical Radiation Theories with Application to the Beam Maser*. Proceedings of the IEEE **51** (1963), 89–109. DOI: 10.1109/PROC.1963.1664 (cit. on p. 13).

[Jon18]   N. Jones: *How to Stop Data Centres from Gobbling up the World's Electricity*. Nature **561** (2018), 163–166. DOI: 10.1038/d41586-018-06610-y (cit. on p. 1).

[Kar+16] A. D. Karenowska, A. V. Chumak, A. A. Serga, and B. Hillebrands: "Magnon Spintronics". *Handbook of Spintronics*. Ed. by Y. Xu, D. D. Awschalom, and J. Nitta. Dordrecht: Springer Netherlands, 2016, pp. 1505–1549. DOI: 10.1007/978-94-007-6892-5_53 (cit. on p. 1).

[KL61]   T. Kasuya and R. C. LeCraw: *Relaxation Mechanisms in Ferromagnetic Resonance*. Physical Review Letters **6** (1961), 223–225. DOI: 10.1103/PhysRevLett.6.223 (cit. on p. 16).

[Kem21]   S. Kemp: *Digital 2021: Global Overview Report*. DataReportal – Global Digital Insights. 2021. URL: https://datareportal.com/reports/digital-2021-global-overview-report (cit. on p. 1).

[KFE16]   S. Kempf, A. Ferring, and C. Enss: *Towards Noise Engineering: Recent Insights in Low-Frequency Excess Flux Noise of Superconducting Quantum Devices*. Applied Physics Letters **109** (2016), 162601. DOI: 10.1063/1.4965293 (cit. on p. 86).

[Kha+12]   M. S. Khalil, M. J. A. Stoutimore, F. C. Wellstood, and K. D. Osborn: *An Analysis Method for Asymmetric Resonator Transmission Applied to Superconducting Devices*. Journal of Applied Physics **111** (2012), 054510. DOI: 10.1063/1.3692073 (cit. on p. 27).

[Khi34]   A. Khintchine: *Korrelationstheorie der stationären stochastischen Prozesse*. Mathematische Annalen **109** (1934), 604–615. DOI: 10.1007/BF01449156 (cit. on p. 65).

[Kim08]   H. J. Kimble: *The Quantum Internet*. Nature **453** (2008), 1023–1030. DOI: 10.1038/nature07127 (cit. on pp. 2, 62, 88).

[Kit48]   C. Kittel: *On the Theory of Ferromagnetic Resonance Absorption*. Physical Review **73** (1948), 155–161. DOI: 10.1103/PhysRev.73.155 (cit. on pp. 6, 86).

[KDC07]   R. H. Koch, D. P. DiVincenzo, and J. Clarke: *Model for $1/F$ Flux Noise in SQUIDs and Qubits*. Physical Review Letters **98** (2007), 267003. DOI: 10.1103/PhysRevLett.98.267003 (cit. on pp. 19, 86).

[Koc+19]   A. F. Kockum, A. Miranowicz, S. D. Liberato, S. Savasta, and F. Nori: *Ultrastrong Coupling between Light and Matter*. Nature Reviews Physics **1** (2019), 19–40. DOI: 10.1038/s42254-018-0006-2 (cit. on pp. 13, 14).

[Kos+19]   S. Kosen, A. F. van Loo, D. A. Bozhko, L. Mihalceanu, and A. D. Karenowska: *Microwave Magnon Damping in YIG Films at Millikelvin Temperatures*. APL Materials **7** (2019), 101120. DOI: 10.1063/1.5115266 (cit. on pp. 4, 16, 19, 63, 80).

[Kos16]   M. Kostylev: *Coupling of Microwave Magnetic Dynamics in Thin Ferromagnetic Films to Stripline Transducers in the Geometry of the Broadband Stripline Ferromagnetic Resonance*. Journal of Applied Physics **119** (2016), 013901. DOI: 10.1063/1.4939470 (cit. on pp. 16, 80).

[KGT16]   N. Kostylev, M. Goryachev, and M. E. Tobar: *Superstrong Coupling of a Microwave Cavity to Yttrium Iron Garnet Magnons*. Applied Physics Letters **108** (2016), 062402. DOI: 10.1063/1.4941730 (cit. on p. 14).

[Kra+19]   P. Krantz, M. Kjaergaard, F. Yan, T. P. Orlando, S. Gustavsson, and W. D. Oliver: *A Quantum Engineer's Guide to Superconducting Qubits*. Applied Physics Reviews **6** (2019), 021318. DOI: 10.1063/1.5089550 (cit. on pp. 2, 49, 63).

[Kri+20]   M. Kristen, A. Schneider, A. Stehli, T. Wolz, S. Danilin, et al.: *Amplitude and Frequency Sensing of Microwave Fields with a Superconducting Transmon Qudit*. npj Quantum Information **6** (2020), 1–5. DOI: 10.1038/s41534-020-00287-w (cit. on p. 89).

[KDG10]   V. V. Kruglyak, S. O. Demokritov, and D. Grundler: *Magnonics*. Journal of Physics D: Applied Physics **43** (2010), 264001. DOI: 10.1088/0022-3727/43/26/264001 (cit. on p. 1).

[KH70]   R. Kubo and N. Hashitsume: *Brownian Motion of Spins*. Progress of Theoretical Physics Supplement **46** (1970), 210–220. DOI: 10.1143/PTPS.46.210 (cit. on p. 86).

[Kum+16]   P. Kumar, S. Sendelbach, M. A. Beck, J. W. Freeland, Z. Wang, H. Wang, C. C. Yu, R. Q. Wu, D. P. Pappas, and R. McDermott: *Origin and Reduction of $1/F$ Magnetic Flux Noise in Superconducting Devices*. Physical Review Applied **6** (2016), 041001. DOI: 10.1103/PhysRevApplied.6.041001 (cit. on p. 86).

[KM99]   S. M. Kuo and D. R. Morgan: *Active Noise Control: A Tutorial Review*. Proceedings of the IEEE **87** (1999), 943–973. DOI: 10.1109/5.763310 (cit. on p. 60).

[Kus19]   S. V. Kusminskiy: *Quantum Magnetism, Spin Waves, and Optical Cavities*. 2019 (cit. on p. 6).

[Lac+19]   D. Lachance-Quirion, Y. Tabuchi, A. Gloppe, K. Usami, and Y. Nakamura: *Hybrid Quantum Systems Based on Magnonics*. Applied Physics Express **12** (2019), 070101. DOI: 10.7567/1882-0786/ab248d (cit. on p. 2).

[Lac+17]   D. Lachance-Quirion, Y. Tabuchi, S. Ishino, A. Noguchi, T. Ishikawa, R. Yamazaki, and Y. Nakamura: *Resolving Quanta of Collective Spin Excitations in a Millimeter-Sized Ferromagnet*. Science Advances **3** (2017), e1603150. DOI: 10.1126/sciadv.1603150 (cit. on pp. 2, 13, 89).

[Lac+20]   D. Lachance-Quirion, S. P. Wolski, Y. Tabuchi, S. Kono, K. Usami, and Y. Nakamura: *Entanglement-Based Single-Shot Detection of a Single Magnon with a Superconducting Qubit*. Science **367** (2020), 425–428. PMID: 31974250. DOI: 10.1126/science.aaz9236 (cit. on pp. 2, 13).

[LL35]   L. D. Landau and E. Lifshitz: *On the Theory of the Dispersion of Magnetic Permeability in Ferromagnetic Bodies*. Phys. Z. Sowjet. (1935) (cit. on p. 9).

[Lee+16]   S. Lee, S. Grudichak, J. Sklenar, C. C. Tsai, M. Jang, Q. Yang, H. Zhang, and J. B. Ketterson: *Ferromagnetic Resonance of a YIG Film in the Low Frequency Regime*. Journal of Applied Physics **120** (2016), 033905. DOI: 10.1063/1.4956435 (cit. on p. 86).

[Leg+13]   Z. Leghtas, G. Kirchmair, B. Vlastakis, M. H. Devoret, R. J. Schoelkopf, and M. Mirrahimi: *Deterministic Protocol for Mapping a Qubit to Coherent State Superpositions in a Cavity*. Physical Review A **87** (2013), 042315. DOI: 10.1103/PhysRevA.87.042315 (cit. on p. 62).

[Li+20]   Y. Li, W. Zhang, V. Tyberkevych, W.-K. Kwok, A. Hoffmann, and V. Novosad: *Hybrid Magnonics: Physics, Circuits, and Applications for Coherent Information Processing*. Journal of Applied Physics **128** (2020), 130902. DOI: 10.1063/5.0020277 (cit. on p. 2).

[Lin+11]   T. Lindström, J. Burnett, M. Oxborrow, and A. Y. Tzalenchuk: *Pound-Locking for Characterization of Superconducting Microresonators*. Review of Scientific Instruments **82** (2011), 104706. DOI: 10.1063/1.3648134 (cit. on pp. 71, 72).

[Lis+16]   J. Lisenfeld, A. Bilmes, S. Matityahu, S. Zanker, M. Marthaler, M. Schechter, G. Schön, A. Shnirman, G. Weiss, and A. V. Ustinov: *Decoherence Spectroscopy with Individual Two-Level Tunneling Defects*. Scientific Reports **6** (2016), 23786. DOI: 10.1038/srep23786 (cit. on p. 89).

[Lis+19]   J. Lisenfeld, A. Bilmes, A. Megrant, R. Barends, J. Kelly, P. Klimov, G. Weiss, J. M. Martinis, and A. V. Ustinov: *Electric Field Spectroscopy of Material Defects in Transmon Qubits*. npj Quantum Information **5** (2019), 1–6. DOI: 10.1038/s41534-019-0224-1 (cit. on p. 89).

[Mai+17]   H. Maier-Flaig, S. Klingler, C. Dubs, O. Surzhenko, R. Gross, M. Weiler, H. Huebl, and S. T. B. Goennenwein: *Temperature-Dependent Magnetic Damping of Yttrium Iron Garnet Spheres*. Physical Review B **95** (2017), 214423. DOI: 10.1103/PhysRevB.95.214423 (cit. on p. 16).

[MK15]   I. S. Maksymov and M. Kostylev: *Broadband Stripline Ferromagnetic Resonance Spectroscopy of Ferromagnetic Films, Multilayers and Nanostructures*. Physica E: Low-dimensional Systems and Nanostructures **69** (2015), 253–293. DOI: 10.1016/j.physe.2014.12.027 (cit. on pp. 16, 80).

[Mat+19]   C. Match, M. Harder, L. Bai, P. Hyde, and C.-M. Hu: *Transient Response of the Cavity Magnon-Polariton*. Physical Review B **99** (2019), 134445. DOI: 10.1103/PhysRevB.99.134445 (cit. on pp. 3, 47, 53).

[Maz04]   B. A. Mazin: *Microwave Kinetic Inductance Detectors*. California Institute of Technology, 2004. DOI: 10.7907/GZ72-V784 (cit. on pp. 22, 23, 72).

[MA19]   M.-A. Miri and A. Alù: *Exceptional Points in Optics and Photonics*. Science **363** (2019). pmid: 30606818. DOI: 10.1126/science.aar7709 (cit. on pp. 36, 39, 40, 44, 87).

[MS98]   K. Miyazaki and K. Seki: *Brownian Motion of Spins Revisited*. The Journal of Chemical Physics **108** (1998), 7052–7059. DOI: 10.1063/1.476123 (cit. on pp. 84, 86).

[Mor+17]   R. G. E. Morris, A. F. van Loo, S. Kosen, and A. D. Karenowska: *Strong Coupling of Magnons in a YIG Sphere to Photons in a Planar Superconducting Resonator in the Quantum Limit*. Scientific Reports **7** (2017), 11511. DOI: 10.1038/s41598-017-11835-4 (cit. on p. 47).

[MCL19]   C. Müller, J. H. Cole, and J. Lisenfeld: *Towards Understanding Two-Level-Systems in Amorphous Solids: Insights from Quantum Circuits*. Reports on Progress in Physics **82** (2019), 124501. DOI: 10.1088/1361-6633/ab3a7e (cit. on pp. 17–19, 63, 81).

[Nak08]   S. Nakamoto: "Bitcoin: A Peer-to-Peer Electronic Cash System". 2008. URL: https://bitcoin.org/en/bitcoin-paper (cit. on p. 1).

[Nem64]   J. Nemarich: *Contribution of the Two-Magnon Process to Magnetostatic-Mode Relaxation*. Physical Review **136** (1964), A1657–A1664. DOI: 10.1103/PhysRev.136.A1657 (cit. on pp. 16, 80).

[Nyq28]   H. Nyquist: *Thermal Agitation of Electric Charge in Conductors*. Physical Review **32** (1928), 110–113. DOI: 10.1103/PhysRev.32.110 (cit. on p. 76).

[OW13]   W. D. Oliver and P. B. Welander: *Materials in Superconducting Quantum Bits*. MRS Bulletin **38** (2013), 816–825. DOI: 10.1557/mrs.2013.229 (cit. on p. 63).

[Osa+16]   A. Osada, R. Hisatomi, A. Noguchi, Y. Tabuchi, R. Yamazaki, K. Usami, M. Sadgrove, R. Yalla, M. Nomura, and Y. Nakamura: *Cavity Opto-magnonics with Spin-Orbit Coupled Photons*. Physical Review Letters **116** (2016), 223601. DOI: 10.1103/PhysRevLett.116.223601 (cit. on pp. 2, 62, 88).

[Pal+14]   E. Paladino, Y. M. Galperin, G. Falci, and B. L. Altshuler: *1/f Noise: Implications for Solid-State Quantum Information*. Reviews of Modern Physics **86** (2014), 361–418. DOI: 10.1103/RevModPhys.86.361 (cit. on p. 19).

[PW93]   D. B. Percival and A. T. Walden: *Spectral Analysis for Physical Applications*. Cambridge: Cambridge University Press, 1993. DOI: 10.1017/CBO9780511622762 (cit. on p. 66).

[PA98]   P. J. Petersan and S. M. Anlage: *Measurement of Resonant Frequency and Quality Factor of Microwave Resonators: Comparison of Methods*. Journal of Applied Physics **84** (1998), 3392–3402. DOI: 10.1063/1.368498 (cit. on p. 27).

[Pfi19]   M. Pfirrmann: *Adding Nonlinearity to an Electromagnetic-Magnonic Quantum Hybrid Device*. Karlsruher Institut für Technologie (KIT) / Karlsruher Institut für Technologie (KIT), 2019. 120 pp. DOI: 10.5445/IR/1000100336 (cit. on pp. 2, 13, 28, 116).

[Pfi+19] M. Pfirrmann, I. Boventer, A. Schneider, T. Wolz, M. Kläui, A. V. Ustinov, and M. Weides: *Magnons at Low Excitations: Observation of Incoherent Coupling to a Bath of Two-Level Systems*. Physical Review Research **1** (2019), 032023. DOI: 10.1103/PhysRevResearch.1.032023 (cit. on pp. 4, 16, 19, 63, 79, 80, 116).

[Phi72]   W. A. Phillips: *Tunneling States in Amorphous Solids*. Journal of Low Temperature Physics **7** (1972), 351–360. DOI: 10.1007/BF00660072 (cit. on p. 17).

[Phi87]   W. A. Phillips: *Two-Level States in Glasses*. Reports on Progress in Physics **50** (1987), 1657–1708. DOI: 10.1088/0034-4885/50/12/003 (cit. on p. 18).

[Pla+20] A. P. M. Place, L. V. H. Rodgers, P. Mundada, B. M. Smitham, M. Fitzpatrick, et al.: *New Material Platform for Superconducting Transmon Qubits with Coherence Times Exceeding 0.3 Milliseconds*. 2020. arXiv: 2003.00024 (cit. on p. 4).

[Poz12]   D. M. Pozar: *Microwave Engineering*. 4th ed. Hoboken, NJ: Wiley, 2012. 732 pp. (cit. on pp. 5, 21, 23, 24, 76).

[Pre18]   J. Preskill: *Quantum Computing in the NISQ Era and Beyond*. Quantum **2** (2018), 79. DOI: 10.22331/q-2018-08-06-79 (cit. on p. 1).

[Pro+15] S. Probst, F. B. Song, P. A. Bushev, A. V. Ustinov, and M. Weides: *Efficient and Robust Analysis of Complex Scattering Data under Noise in Microwave Resonators*. Review of Scientific Instruments **86** (2015), 024706. DOI: 10.1063/1.4907935 (cit. on pp. 27, 79, 116).

[PMS19]   I. Proskurin, R. Macêdo, and R. L. Stamps: *Microscopic Origin of Level Attraction for a Coupled Magnon-Photon System in a Microwave Cavity*. New Journal of Physics **21** (2019), 095003. DOI: 10.1088/1367-2630/ab3cb7 (cit. on pp. 3, 36).

[qki]   qkitgroup: *Qkit - a Quantum Measurement Suite in Python*. URL: https://github.com/qkitgroup/qkit (cit. on p. 49).

[Qui+10] M. Quinsat, D. Gusakova, J. F. Sierra, J. P. Michel, D. Houssameddine, et al.: *Amplitude and Phase Noise of Magnetic Tunnel Junction Oscillators*. Applied Physics Letters **97** (2010), 182507. DOI: 10.1063/1.3506901 (cit. on p. 85).

[Rab37]   I. I. Rabi: *Space Quantization in a Gyrating Magnetic Field*. Physical Review **51** (1937), 652–654. DOI: 10.1103/PhysRev.51.652 (cit. on p. 12).

[Rau+]   M. Rauchs, A. Blandin, A. Dek, and Y. Wu: *Cambridge Bitcoin Electricity Consumption Index (CBECI)*. URL: https://cbeci.org/ (cit. on p. 1).

[Rei15]   D. J. Reilly: *Engineering the Quantum-Classical Interface of Solid-State Qubits*. npj Quantum Information **1** (2015), 15011. DOI: 10.1038/npjqi.2015.11 (cit. on p. 62).

[RZ69]   S. M. Rezende and N. Zagury: *Coherent Magnon States*. Physics Letters A **29** (1969), 47–48. DOI: 10.1016/0375-9601(69)90788-9 (cit. on p. 2).

[Rub09]   E. Rubiola: *Phase noise and frequency stability in oscillators*. CERN Document Server. 2009. URL: https://cds.cern.ch/record/2150670 (cit. on p. 73).

[RB10]   E. Rubiola and R. Brendel: *A Generalization of the Leeson Effect*. 2010. arXiv: 1004.5539 (cit. on p. 74).

[Rum+19]   S. Rumyantsev, M. Balinskiy, F. Kargar, A. Khitun, and A. A. Balandin: *The Discrete Noise of Magnons*. Applied Physics Letters **114** (2019), 090601. DOI: 10.1063/1.5088651 (cit. on pp. 64, 85).

[Sch20]   A. Schneider: *Quantum Sensing Experiments with Superconducting Qubits*. 2020. DOI: 10.5445/IR/1000117442 (cit. on pp. 13, 28, 89).

[Sch+18]   A. Schneider, J. Braumüller, L. Guo, P. Stehle, H. Rotzinger, M. Marthaler, A. V. Ustinov, and M. Weides: *Local Sensing with the Multilevel Ac Stark Effect*. Physical Review A **97** (2018), 062334. DOI: 10.1103/PhysRevA.97.062334 (cit. on p. 89).

[Sch+19]   A. Schneider, T. Wolz, M. Pfirrmann, M. Spiecker, H. Rotzinger, A. V. Ustinov, and M. Weides: *Transmon Qubit in a Magnetic Field: Evolution of Coherence and Transition Frequency*. Physical Review Research **1** (2019), 023003. DOI: 10.1103/PhysRevResearch.1.023003 (cit. on p. 89).

[Sch07]   D. I. Schuster: *Circuit Quantum Electrodynamics*. Yale University, 2007. URL: http://adsabs.harvard.edu/abs/2007PhDT.......167S (cit. on pp. 22, 23).

[Sei64]   P. E. Seiden: *Ferrimagnetic Resonance Relaxation in Rare-Earth Iron Garnets*. Physical Review **133** (1964), A728–A736. DOI: 10.1103/PhysRev.133.A728 (cit. on p. 80).

[Sen+08]   S. Sendelbach, D. Hover, A. Kittel, M. Mück, J. M. Martinis, and R. McDermott: *Magnetism in SQUIDs at Millikelvin Temperatures*. Physical Review Letters **100** (2008), 227006. DOI: 10.1103/PhysRevLett.100.227006 (cit. on p. 86).

[SCH10]   A. A. Serga, A. V. Chumak, and B. Hillebrands: *YIG Magnonics*. Journal of Physics D: Applied Physics **43** (2010), 264002. DOI: 10.1088/0022-3727/43/26/264002 (cit. on pp. 1, 8, 15).

[Sha38]   C. E. Shannon: *A Symbolic Analysis of Relay and Switching Circuits*. Transactions of the American Institute of Electrical Engineers **57** (1938), 713–723. DOI: 10.1109/T-AIEE.1938.5057767 (cit. on p. 1).

[Sha48]   C. E. Shannon: *A Mathematical Theory of Communication*. The Bell System Technical Journal **27** (1948), 379–423. DOI: 10.1002/j.1538-7305.1948.tb01338.x (cit. on p. 1).

[Shi07]   A. J. Shields: *Semiconductor Quantum Light Sources*. Nature Photonics **1** (2007), 215–223. DOI: 10.1038/nphoton.2007.46 (cit. on p. 14).

[Sho97]   P. W. Shor: *Polynomial-Time Algorithms for Prime Factorization and Discrete Logarithms on a Quantum Computer*. SIAM Journal on Computing **26** (1997), 1484–1509. DOI: 10.1137/S0097539795293172 (cit. on p. 2).

[SS17]   R. H. Shumway and D. S. Stoffer: *Time Series Analysis and Its Applications: With R Examples*. 4th ed. 2017. Springer Texts in Statistics. Cham: Springer International Publishing : Imprint: Springer, 2017. 1 p. DOI: 10.1007/978-3-319-52452-8 (cit. on p. 66).

[SP16]   N. A. Sinitsyn and Y. V. Pershin: *The Theory of Spin Noise Spectroscopy: A Review*. Reports on Progress in Physics **79** (2016), 106501. DOI: 10.1088/0034-4885/79/10/106501 (cit. on p. 86).

[SLK61]   M. Sparks, R. Loudon, and C. Kittel: *Ferromagnetic Relaxation. I. Theory of the Relaxation of the Uniform Precession and the Degenerate Spectrum in Insulators at Low Temperatures*. Physical Review **122** (1961), 791–803. DOI: 10.1103/PhysRev.122.791 (cit. on pp. 16, 80).

[SLL61]   E. G. Spencer, R. C. LeCraw, and R. C. Linares: *Low-Temperature Ferromagnetic Relaxation in Yttrium Iron Garnet*. Physical Review **123** (1961), 1937–1938. DOI: 10.1103/PhysRev.123.1937 (cit. on pp. 4, 16).

[Ste+20]   A. Stehli, J. D. Brehm, T. Wolz, P. Baity, S. Danilin, V. Seferai, H. Rotzinger, A. V. Ustinov, and M. Weides: *Coherent Superconducting Qubits from a Subtractive Junction Fabrication Process*. Applied Physics Letters **117** (2020), 124005. DOI: 10.1063/5.0023533 (cit. on p. 49).

[Ste06]   J. Stepišnik: *NMR down to Earth*. Nature **439** (2006), 799–800. DOI: 10.1038/439799a (cit. on p. 118).

[SZ99]   H. von Storch and F. W. Zwiers: *Statistical Analysis in Climate Research*. Cambridge: Cambridge University Press, 1999. DOI: 10.1017/CBO9780511612336 (cit. on p. 66).

[Sud+12]   V. Sudhir, M. G. Genoni, J. Lee, and M. S. Kim: *Critical Behavior in Ultrastrong-Coupled Oscillators*. Physical Review A **86** (2012), 012316. DOI: 10.1103/PhysRevA.86.012316 (cit. on p. 15).

[Tab+14]   Y. Tabuchi, S. Ishino, T. Ishikawa, R. Yamazaki, K. Usami, and Y. Nakamura: *Hybridizing Ferromagnetic Magnons and Microwave Photons in the Quantum Limit*. Physical Review Letters **113** (2014), 083603. DOI: 10.1103/PhysRevLett.113.083603 (cit. on pp. 4, 16, 19).

[Tab+15]   Y. Tabuchi, S. Ishino, A. Noguchi, T. Ishikawa, R. Yamazaki, K. Usami, and Y. Nakamura: *Coherent Coupling between a Ferromagnetic Magnon and a Superconducting Qubit*. Science **349** (2015), 405–408. pmid: 26160378. DOI: 10.1126/science.aaa3693 (cit. on pp. 2, 63, 89).

[Tab+16]   Y. Tabuchi, S. Ishino, A. Noguchi, T. Ishikawa, R. Yamazaki, K. Usami, and Y. Nakamura: *Quantum Magnonics: The Magnon Meets the Superconducting Qubit*. Comptes Rendus Physique. Quantum Microwaves / Micro-Ondes Quantiques **17** (2016), 729–739. DOI: 10.1016/j.crhy.2016.07.009 (cit. on pp. 2, 6, 8, 13, 15).

[UO30]   G. E. Uhlenbeck and L. S. Ornstein: *On the Theory of the Brownian Motion*. Physical Review **36** (1930), 823–841. DOI: 10.1103/PhysRev.36.823 (cit. on p. 68).

[Vla+13]   B. Vlastakis, G. Kirchmair, Z. Leghtas, S. E. Nigg, L. Frunzio, S. M. Girvin, M. Mirrahimi, M. H. Devoret, and R. J. Schoelkopf: *Deterministically Encoding Quantum Information Using 100-Photon Schrödinger Cat States*. Science **342** (2013), 607–610. pmid: 24072821. DOI: 10.1126/science.1243289 (cit. on p. 62).

[VH77]   M. Von Schickfus and S. Hunklinger: *Saturation of the Dielectric Absorption of Vitreous Silica at Low Temperatures*. Physics Letters A **64** (1977), 144–146. DOI: 10.1016/0375-9601(77)90558-8 (cit. on p. 80).

[Wal31]   G. T. Walker: *On Periodicity in Series of Related Terms*. Proceedings of the Royal Society of London. Series A, Containing Papers of a Mathematical and Physical Character **131** (1931), 518–532. DOI: 10.1098/rspa.1931.0069 (cit. on p. 70).

[Wal57]   L. R. Walker: *Magnetostatic Modes in Ferromagnetic Resonance*. Physical Review **105** (1957), 390–399. DOI: 10.1103/PhysRev.105.390 (cit. on p. 8).

[Wal58]   L. R. Walker: *Resonant Modes of Ferromagnetic Spheroids*. Journal of Applied Physics **29** (1958), 318–323. DOI: 10.1063/1.1723117 (cit. on p. 8).

[Wal+04]   A. Wallraff, D. I. Schuster, A. Blais, L. Frunzio, R.-S. Huang, J. Majer, S. Kumar, S. M. Girvin, and R. J. Schoelkopf: *Strong Coupling of a Single Photon to a Superconducting Qubit Using Circuit Quantum Electrodynamics*. Nature **431** (2004), 162–167. DOI: 10.1038/nature02851 (cit. on p. 14).

[Wan+09]   H. Wang, M. Hofheinz, J. Wenner, M. Ansmann, R. C. Bialczak, et al.: *Improving the Coherence Time of Superconducting Coplanar Resonators.* Applied Physics Letters **95** (2009), 233508. DOI: 10.1063/1.3273372 (cit. on p. 18).

[WH20]   Y.-P. Wang and C.-M. Hu: *Dissipative Couplings in Cavity Magnonics*. Journal of Applied Physics **127** (2020), 130901. DOI: 10.1063/1.5144202 (cit. on pp. 3, 13, 36, 87).

[Wan+18]   Y.-P. Wang, G.-Q. Zhang, D. Zhang, T.-F. Li, C.-M. Hu, and J. Q. You: *Bistability of Cavity Magnon Polaritons*. Physical Review Letters **120** (2018). DOI: 10.1103/PhysRevLett.120.057202 (cit. on p. 36).

[Wel67]   P. Welch: *The Use of Fast Fourier Transform for the Estimation of Power Spectra: A Method Based on Time Averaging over Short, Modified Periodograms*. IEEE Transactions on Audio and Electroacoustics **15** (1967), 70–73. DOI: 10.1109/TAU.1967.1161901 (cit. on pp. 65, 80).

[Wie30]   N. Wiener: *Generalized Harmonic Analysis*. Acta Mathematica **55** (1930), 117–258. DOI: 10.1007/BF02546511 (cit. on p. 65).

[Wol+20]   T. Wolz, A. Stehli, A. Schneider, I. Boventer, R. Macêdo, A. V. Ustinov, M. Kläui, and M. Weides: *Introducing Coherent Time Control to Cavity Magnon-Polariton Modes*. Communications Physics **3** (2020), 1–6. DOI: 10.1038/s42005-019-0266-x (cit. on pp. 4, 10, 47, 48, 52, 54, 58–60, 87, 113–115).

[XAN16]   Y. Xu, D. D. Awschalom, and J. Nitta, eds.: *Handbook of Spintronics. Vol. 2: ...* Springer Reference. Dordrecht: Springer, 2016. 977 pp (cit. on p. 1).

[Yan+18]   F. Yan, D. Campbell, P. Krantz, M. Kjaergaard, D. Kim, et al.: *Distinguishing Coherent and Thermal Photon Noise in a Circuit Quantum Electrodynamical System*. Physical Review Letters **120** (2018), 260504. DOI: 10.1103/PhysRevLett.120.260504 (cit. on p. 89).

[Yan+13]   F. Yan, S. Gustavsson, J. Bylander, X. Jin, F. Yoshihara, D. G. Cory, Y. Nakamura, T. P. Orlando, and W. D. Oliver: *Rotating-Frame Relaxation as a Noise Spectrum Analyser of a Superconducting Qubit Undergoing Driven Evolution*. Nature Communications **4** (2013), 2337. DOI: 10.1038/ncomms3337 (cit. on p. 89).

[Yan+19]   Y. Yang, J. Rao, Y. Gui, B. Yao, W. Lu, and C.-M. Hu: *Control of the Magnon-Photon Level Attraction in a Planar Cavity*. Physical Review Applied **11** (2019), 054023. DOI: 10.1103/PhysRevApplied.11.054023 (cit. on p. 41).

[Yao+19a] B. Yao, T. Yu, Y. S. Gui, J. W. Rao, Y. T. Zhao, W. Lu, and C.-M. Hu: *Coherent Control of Magnon Radiative Damping with Local Photon States*. Communications Physics **2** (2019), 1–8. DOI: 10.1038/s42005-019-0264-z (cit. on p. 41).

[Yao+19b] B. Yao, T. Yu, X. Zhang, W. Lu, Y. Gui, C.-M. Hu, and Y. M. Blanter: *The Microscopic Origin of Magnon-Photon Level Attraction by Traveling Waves: Theory and Experiment*. Physical Review B **100** (2019), 214426. DOI: 10.1103/PhysRevB.100.214426 (cit. on pp. 3, 41).

[Yos+18]   F. Yoshihara, T. Fuse, Z. Ao, S. Ashhab, K. Kakuyanagi, S. Saito, T. Aoki, K. Koshino, and K. Semba: *Inversion of Qubit Energy Levels in Qubit-Oscillator Circuits in the Deep-Strong-Coupling Regime*. Physical Review Letters **120** (2018), 183601. DOI: 10.1103/PhysRevLett.120.183601 (cit. on p. 14).

[Yos+17]   F. Yoshihara, T. Fuse, S. Ashhab, K. Kakuyanagi, S. Saito, and K. Semba: *Superconducting Qubit–Oscillator Circuit beyond the Ultrastrong-Coupling Regime*. Nature Physics **13** (2017), 44–47. DOI: 10.1038/nphys3906 (cit. on p. 14).

[Yua+20]   H. Y. Yuan, P. Yan, S. Zheng, Q. Y. He, K. Xia, and M.-H. Yung: *Steady Bell State Generation via Magnon-Photon Coupling*. Physical Review Letters **124** (2020), 053602. DOI: 10.1103/PhysRevLett.124.053602 (cit. on pp. 45, 62, 87).

[Yul27]   G. U. Yule: *On a Method of Investigating Periodicities Disturbed Series, with Special Reference to Wolfer's Sunspot Numbers*. Philosophical Transactions of the Royal Society of London. Series A, Containing Papers of a Mathematical or Physical Character **226** (1927), 267–298. DOI: 10.1098/rsta.1927.0007 (cit. on p. 70).

[Zap13]   V. S. Zapasskii: *Spin-Noise Spectroscopy: From Proof of Principle to Applications*. Advances in Optics and Photonics **5** (2013), 131–168. DOI: 10.1364/AOP.5.000131 (cit. on p. 86).

[Zha+17]   D. Zhang, X.-Q. Luo, Y.-P. Wang, T.-F. Li, and J. Q. You: *Observation of the Exceptional Point in Cavity Magnon-Polaritons*. Nature Communications **8** (2017), 1368. DOI: 10.1038/s41467-017-01634-w (cit. on pp. 13, 36, 41).

[Zha+16]   X. Zhang, N. Zhu, C.-L. Zou, and H. X. Tang: *Optomagnonic Whispering Gallery Microresonators*. Physical Review Letters **117** (2016), 123605. DOI: 10.1103/PhysRevLett.117.123605 (cit. on pp. 2, 88).

[Zha+14]   X. Zhang, C.-L. Zou, L. Jiang, and H. X. Tang: *Strongly Coupled Magnons and Cavity Microwave Photons*. Physical Review Letters **113** (2014), 156401. DOI: 10.1103/PhysRevLett.113.156401 (cit. on pp. 2, 3, 14, 35, 47, 53).

[Zha+15]   X. Zhang, C.-L. Zou, N. Zhu, F. Marquardt, L. Jiang, and H. X. Tang: *Magnon Dark Modes and Gradient Memory*. Nature Communications **6** (2015), 8914. DOI: 10.1038/ncomms9914 (cit. on pp. 3, 13, 88).

[ŽFD04]   I. Žutić, J. Fabian, and S. Das Sarma: *Spintronics: Fundamentals and Applications*. Reviews of Modern Physics **76** (2004), 323–410. DOI: 10.1103/RevModPhys.76.323 (cit. on p. 1).

List of Publications

[Wol+20]   **T. Wolz**, A. Stehli, A. Schneider, I. Boventer, R. Macêdo, A. V. Ustinov, M. Kläui, and M. Weides: *Introducing Coherent Time Control to Cavity Magnon-Polariton Modes*. Communications Physics **3** (2020), 1–6. DOI: 10.1038/s42005-019-0266-x.

[Sch+19]   A. Schneider, **T. Wolz**, M. Pfirrmann, M. Spiecker, H. Rotzinger, A. V. Ustinov, and M. Weides: *Transmon Qubit in a Magnetic Field: Evolution of Coherence and Transition Frequency*. Physical Review Research **1** (2019), 023003. DOI: 10.1103/PhysRevResearch.1.023003.

[Bov+20]   I. Boventer, C. Dörflinger, **T. Wolz**, R. Macêdo, R. Lebrun, M. Kläui, and M. Weides: *Control of the Coupling Strength and Linewidth of a Cavity Magnon-Polariton*. Physical Review Research **2** (2020), 013154. DOI: 10.1103/PhysRevResearch.2.013154.

[Ste+20]   A. Stehli, J. D. Brehm, **T. Wolz**, P. Baity, S. Danilin, V. Seferai, H. Rotzinger, A. V. Ustinov, and M. Weides: *Coherent Superconducting Qubits from a Subtractive Junction Fabrication Process*. Applied Physics Letters **117** (2020), 124005. DOI: 10.1063/5.0023533.

[Pfi+19]   M. Pfirrmann, I. Boventer, A. Schneider, **T. Wolz**, M. Kläui, A. V. Ustinov, and M. Weides: *Magnons at Low Excitations: Observation of Incoherent Coupling to a Bath of Two-Level Systems*. Physical Review Research **1** (2019), 032023. DOI: 10.1103/PhysRevResearch.1.032023.

[Kri+20]   M. Kristen, A. Schneider, A. Stehli, **T. Wolz**, S. Danilin, et al.: *Amplitude and Frequency Sensing of Microwave Fields with a Superconducting Transmon Qudit*. npj Quantum Information **6** (2020), 1–5. DOI: 10.1038/s41534-020-00287-w.

Appendix

A Coupling Strength Control

A.1 Phase Response of the Two Tone CMP by Input-Output Formalism

In Ch. 4 in the main text, we focused on the amplitude signal $|S_{11}|$ of the two-tone driven CMP and saw how the eigenmodes translates to features in the dispersion spectra. Here, we consider the phase response arg S_{11} for the same parameters and again calculated via input-output formalism, Eq. (4.8). The calculated data is displayed in Fig. A.1. Panel a depicts the standard single tone CMP response for comparison. Figure A.1b and c show the data for an increased level repulsion and for level merging. The phase dispersion spectra qualitatively look as expected. However, we can already notice, that the maximum phase values (see color bars) changes depending on applied phase difference and amplitude ratio, which is a simple consequence of the coupling strength now having an imaginary part. This however complicates the interpretation. Going further into the regime of level attraction / coexistence (Fig. A.1d and e), we can observe phase jumps of 2π. Recall, for a single cavity this should only be possible for the strongly overcoupled cavity, which is not the case here ($\kappa_c/2\pi = 1\,\text{MHz}$ and $\kappa_L/2\pi = 4\,\text{MHz}$). These strong phase jumps however only occur at specific magnon frequencies (field values) and never at the crossing points. Here, a problem arises with the calculated data: We can compare line traces at the crossing points (Fig. A.1f) to the experimental data presented in Ref. [Har+18; Bov+20] [1] In these experiments a phase jump of 2π was observed, as opposed to the numerical values with a small phase jump of only $\pi/5$. Hence, the input-output formalism fails to capture the correct phase behavior and may need further extensions to fit the experiment. Nevertheless it still provides some practicality for amplitude data in the level attraction regime.

---

[1] In Ref. [Har+18] a transmission cavity was employed, which changes the numerator of Eq. (4.8) but does not affect this argumentation.
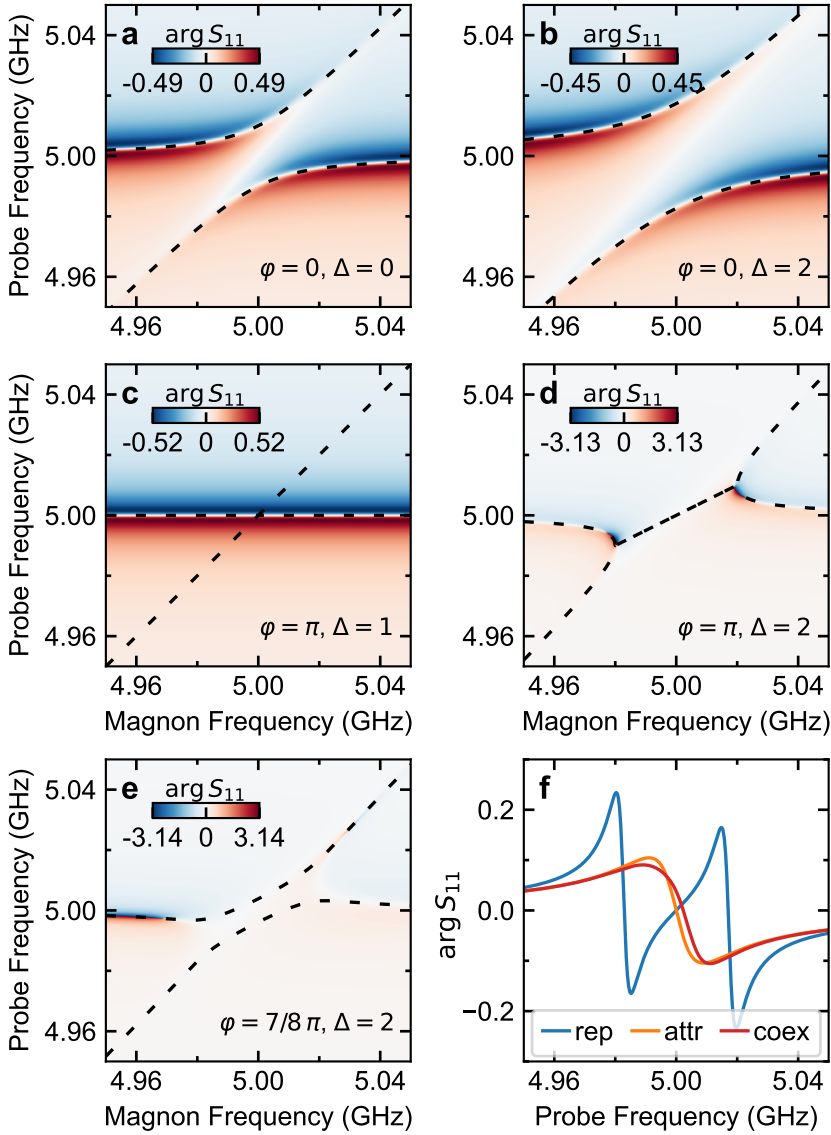
Figure A.1: Phase response of the two-tone CMP calculated according to Eq. (4.8). Chosen parameters are the same as in the main text. **a** One tone response, **b**, increased level repulsion, **c** level merging, **d** level attraction, **e** coexistence of attraction and repulsion, **e** line cuts at the crossing points of data from panels **b,d,e**.

B Coherent Time Control

B.1 Cable Delay

Figure B.1 shows the recorded time trace for a cable delay extraction scheme. The two pulses are emitted with a delay of 100 ns to each resonating system, but recorded with 107 ns as determined via Gaussian fits. Due to the filter function of the two resonating systems both pulses are slightly distorted.

B.2 Field Geometry and Cavity Configuration

Figure B.2 shows the field geometry of the employed CMP sample for the time domain experiments presented in Ch. 5. The magnon system is excited by the rf field generated around a micro strip line, which is glued to the copper re-entrant cavity. The stripline is made from a copper cladded Rogers TMM10i substrate with a thickness of 0.64 mm. It is 50 Ω matched and open ended. This field configuration minimizes unwanted crosstalk due to the perpendicular arrangement of the magnon and cavity field while only affecting the cavity minimally [Wol+20].
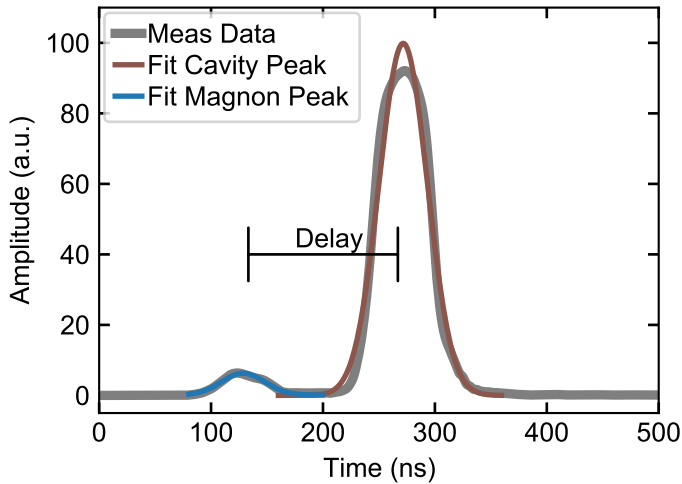
Figure B.1: Reflected and transmitted pulses for cable delay extraction. With a delay of 100 ns Gaussian pulses are emitted to magnon system and cavity, respectively. The recorded peaks are then fitted and the mean values of the Gaussians yield the cable delay; in this case 7 ns.
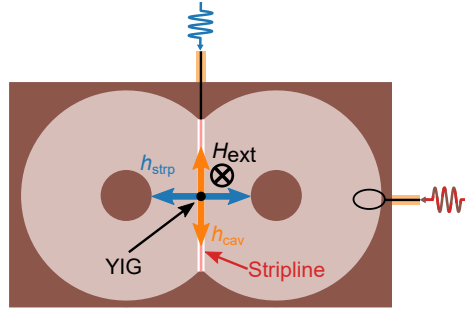
Figure B.2: Field geometry inside the re-entrant cavity. External (DC) bias field H_{ext}, cavity rf field h_{cav} and magnon rf field h_{strp} stand all perpendicular to each other, minimizing unwanted crosstalk. The magnon field is generated by a strip line beneath the YIG sphere. [Wol+20]

B.3 Simulation of One- and Two-Pulse Experiments

In this section, we verify the measured data presented and discussed in Sec. 5.4.1 by numerical simulations as described in Sec. 5.2.4. In the experiment with a single pulse to the cavity (Figs. B.3a,b), classical magnon Rabi oscillations are visible, i.e., the beat mode is excited. Simulated data shows the same color-coded Rabi-Chevron pattern apart from the higher order mode, which is neglected in the simulation. The two-pulse experiment (Figs. B.3a,b), i.e., simultaneous pulses to cavity and magnon system, in which the normal mode is excited also agrees well with the simulated data by showing diminishing oscillations towards the crossing point. Figures. B.3e,f display line traces at the crossing points (dashed lines) of the previous panels. The simulated data only exhibit a slightly straighter exponential decay than the measured due to the perfect amplitude matching as well as deeper oscillations due to zero crosstalk. In summary, for both experiments, an excellent agreement between measurement and simulation is found, which underpins the accuracy of the presented control method.
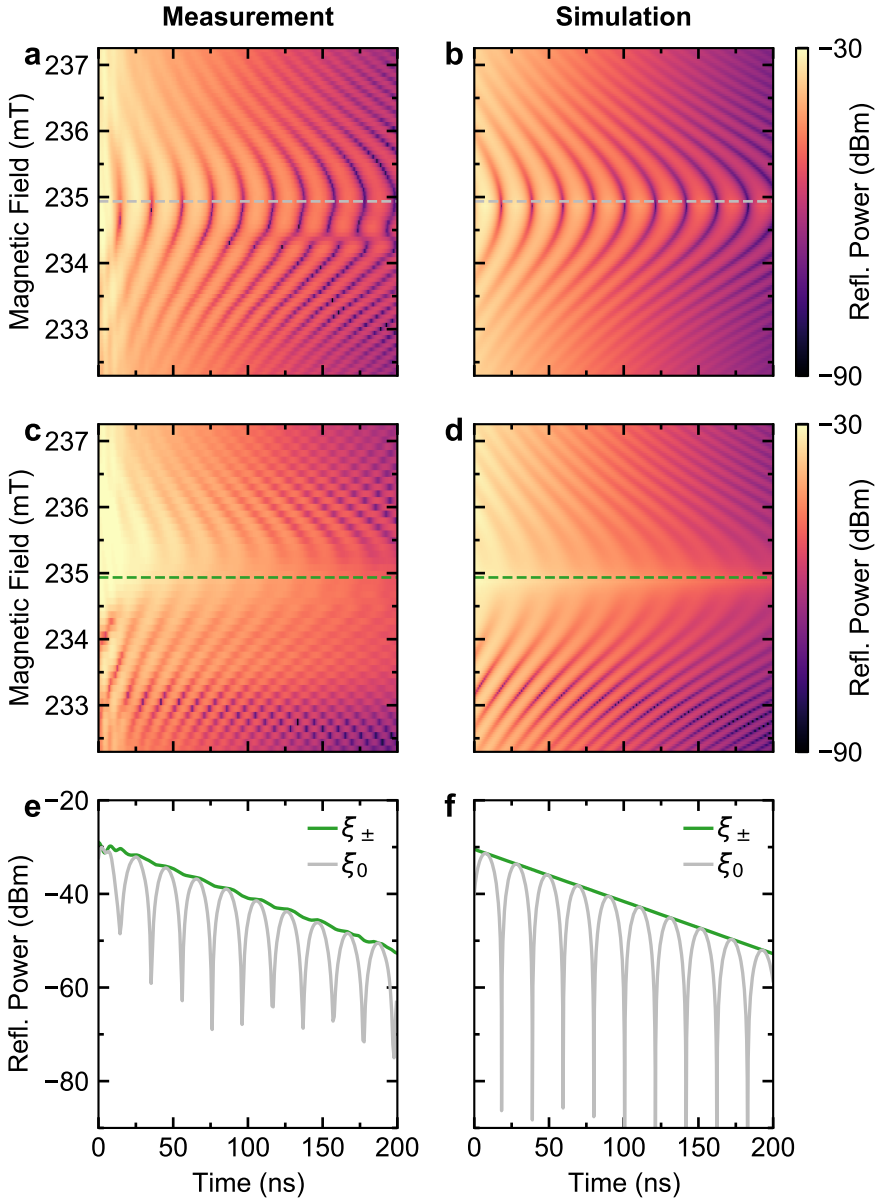
Figure B.3: Comparison of measured and simulated one and two pulse experiments. First row (**a,b**) shows classical magnon Rabi oscillation of the one pulse experiment, exciting the beat mode. Second row (**c,d**) depicts the data of a two pulse experiment with the normal mode excited at the crossing point. Third row (**e,f**) emphasizes the different responses by line cuts (dashed lines) at the crossing point. Figure adapted from [Wol+20].

C FMR Linewidth and Frequency Noise

C.1 Fits to Different TLS Models

Fitting linewidth data to the TLS-STM model, Eq. (2.24), requires several post processing steps and the choice of the respective procedure for each step can introduce errors, which are propagated and subsequently influence the final result. When drawing conclusions from the data, one should keep in mind that the chosen process can lead to a bias. In the following the three steps affecting these results are discussed.

First, the raw scattering data is often background corrected to ease the subsequent fitting procedure. A simple way is to simply divide the traces with an FMR resonance by an off-resonant measurement, or for CMP data by a mean trace, where the resonance data are excluded in the averaging process, see for instance [Pfi19]. However, what is not considered is that cable resonances can hybridize (to some extent) with the actual FMR resonance. A simple division does not account for such a hybridization. Hence, linewidth changes can be altered due to cable resonance and background correction.

Second, the decay rates have to be extracted from the (background corrected) data. For a simple FMR measurement the process is straight forward by using a circle-fit routine [Pro+15]. For a CMP measurement yielding a dispersion spectra, however, the choice is not that easy. One has to employ an equation for the coupled system, such as Eq. (3.37). But now one has to face the following choices, each coming with its own drawbacks. a) Fitting only the data at the crossing point. Here however most of the data are simply thrown away, and an additional circle fit to off-resonant data is required to determine the cavity parameters, which assumes that the coupling constant is not affected by the FMR mode. b) Fitting trace after trace for all magnetic field values. This procedure uses of course all the data but may have higher uncertainties of the parameter in the off-resonant region due to the small amplitude signal. c) Fitting the whole dispersion spectra in one calculation. This way may superficially yield the best results simply due to the biggest ratio of data to free parameters. However the implicit assumption is that the magnon decay rate stays constant over the magnetic field sweep. Recalling, that the excitation power of the magnon system changes with magnetic field and that the TLS linewidth contribution is power dependent, we can see that this option also produces an error. Compare Ref.[Pfi+19] for off-resonant decay rates.

Third, when fitting the decay rates to Eq. (2.24) the standard way has been to fit the data trace by trace, i.e., for fixed power but different temperatures and vice
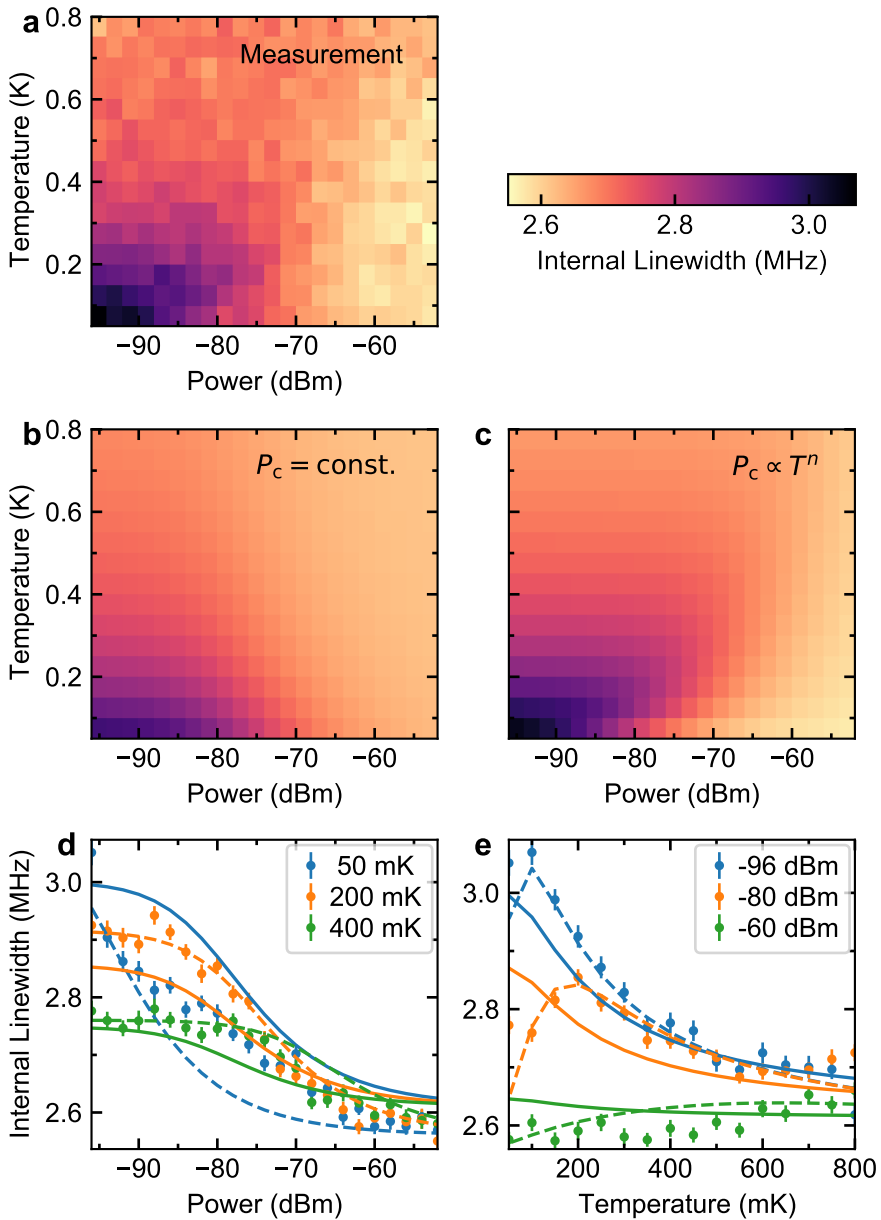
Figure C.1: Comparison of fits with and without a temperature dependence of P_c**. a** Measured and extracted internal Linewidth of FMR, **b** Least square fit of all data points with P_c = const, **c** similar fit but with $P_c \propto T^n$ and n as a phenomenological parameter. **d** and **e** show linecuts at different temperatures and powers. Circles represent measurement data, solid and dashed lines fit to constant (**b**) and changing (**c**) critical power, respectively.

versa. This proceeding however is subject to a form of "overfitting". Since for each trace the parameters $\kappa_{0,TLS}$ and κ_{offs} can be chosen independently, deviations from Eq. (2.24) can be absorbed into these two parameters and therefore biasing the whole evaluation towards a better fit. The other choice would again be to fit all data in one calculation. Here, however one has to consider the change of P_c with temperature, introducing a new free parameter. Moreover κ_{offs} can indeed change with temperature due to the beginning of temperature peak processes. This option then biases the evaluation rather away from the TLS model. Figure C.1 shows a comparison of the different fitting choices. Panel a depicts the measured and fitted linewidth (compare Sec. 6.4.1) and contrasts the data to fits to Eq. (2.24) with constant P_c (b) and $P_c \propto T^n$ with n as a phenomenological parameter between 2 and 4 (c). Both fits show qualitatively a behavior close to the measured data. However in the intermediate temperature region for high power, one can observe a discrepancy. The discrepancy becomes even more visible in the linecuts of the data for constant power and temperature (panels d and e). While certain traces fit well, others do show strong deviations. These deviations are bigger than in previously reported data due to the fixed $\kappa_{0,TLS}$ and κ_{offs}.

In summary, an accurate quantitative analysis of the TLS parameter for FMR/CMP linewidth data is difficult and hence a bullet-proof conclusion cannot be drawn easily.

C.2 Comparison to Fluctuations of the Earth Magnetic field

Figure C.2 shows a histogram of the measured frequency fluctuations converted to field fluctuations via the Kittel formula. The data fits well to a Gaussian function with a standard deviation of $\sigma \approx 3\,\mu T$. According to Ref. [Ste06] the earth magnetic field fluctuates in the range of 25 nT within one day, which is a factor 100 smaller than the standard deviation we observed within one hour.

C.3 Power Spectral Density Data

In the main text, three FMR frequency noise PSDs were presented for different power and temperature. In this section, we show more data to underpin the statement of independent frequency noise spectra with respect to power and temperature and also to illustrate the small difference between the spectra for the two examined resonance frequencies. Figure C.3a shows PSD data for a resonance frequency of $\omega_r/2\pi = 4.32\,\text{GHz}$ at fixed temperature. No power dependence is visible, apart from the increasing HEMT noise for lower input powers. The
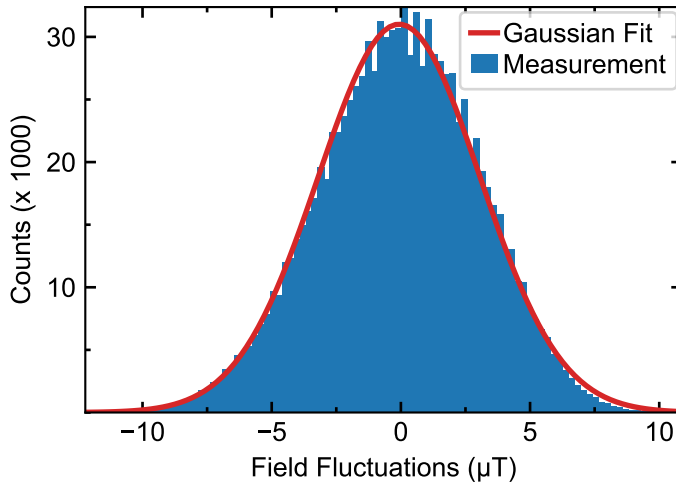
Figure C.2: Histogram of FMR frequency fluctuations converted to field fluctuations via the Kittel formula. Data has been subtracted by its mean value and subsequently fitted to a Gaussian function $f(x) = a \exp\left(x^2/(2\sigma^2)\right)$, with a as scaling parameter and σ as standard deviation.

same behavior can be seen in Fig. C.3b for data taken at $\omega_{\mathrm{r}}/2\pi = 6.11\,\mathrm{GHz}$. The temperature independence is illustrated Fig. C.3c.

Comparing the PSDs at $\omega_{\mathrm{r}}/2\pi \approx 4\,\mathrm{GHz}$ and $6\,\mathrm{GHz}$, one can notice a difference in the steep decrease at $1\,\mathrm{Hz}$. This variation may be due to a not fully saturated magnetization[2] in the sample. A complete saturation may result in a different internal magnetic environment and therefore in different noise interactions. A conclusive answer, however, is difficult to draw, especially due to the additional HEMT noise in that region.

C.4 PACF Dependence on Sampling Bandwidth

In section 6.4.3, we evaluated the PACF for a sampling rate of $8\,\mathrm{Hz}$ as a product of post-averaging to remove periodic fluctuations and the $1/f$ HEMT noise. The choice of sampling rate however influences the PACF. Figure C.4a shows the PACF dependence on the sampling rate for the first four lags. Values above $2\,\mathrm{Hz}$ are strongly influenced by periodic signals, which are not completely averaged; visible as peaks between $4\,\mathrm{Hz}$ and $20\,\mathrm{Hz}$ int the FMR PSD. Below $1\,\mathrm{Hz}$ predominantly lags $n = 1, 2$ are significant going over to a pure Brownian motion process with friction

---

[2] The saturation magnetization M_{s} for our YIG samples is specified to be $2\pi M_{\mathrm{s}}/\gamma = 4.9\,\mathrm{GHz}$.
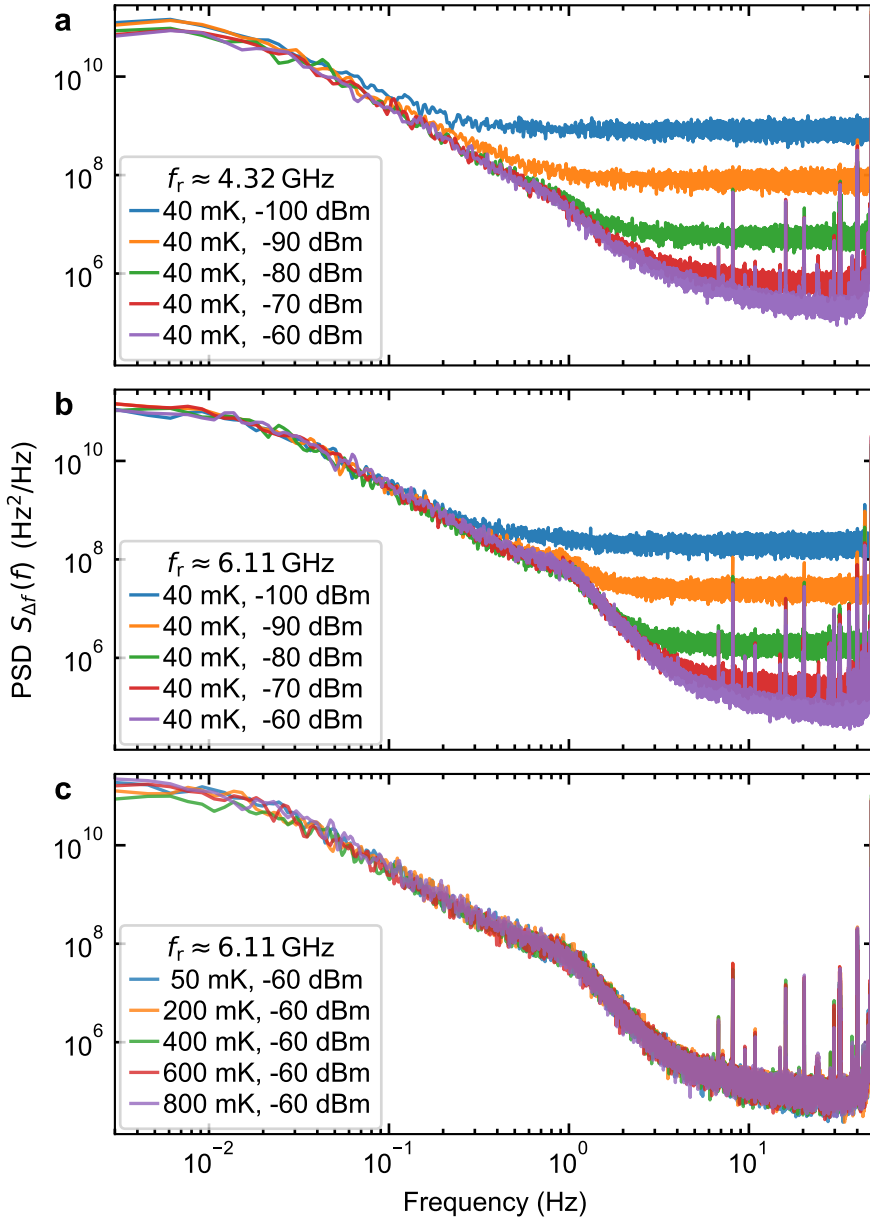
Figure C.3: FMR frequency noise power spectral densities (PSDs) for different power, temperature and resonance frequencies. a Frequency noise PSDs at $\omega_r/2\pi = 4.32\,\text{GHz}$ for constant temperature but different powers. Low frequency part is power independent. For decreasing power HEMT noise covers FMR noise. **b** Noise PSDs at $\omega_r/2\pi = 6.11\,\text{GHz}$ for constant temperature show now power dependence but a steeper decrease at 1 Hz than in a. **c** Noise PSDs are independent of temperature between $50\,\text{mK}$ and $800\,\text{mK}$.
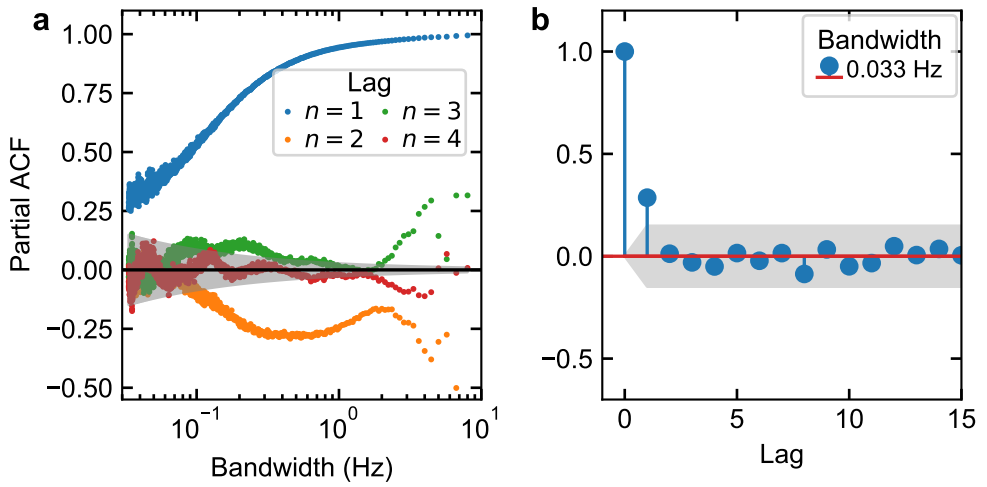
Figure C.4: Partial autocorrelation function (PACF) dependent on sampling bandwidth. Panel **a** depicts the PACF for the first four lags dependent on the post processing sampling bandwidth. Grey area denotes the 95 % confidence interval. Values in this region can be considered as statistically insignificant. **b** PACF for lags up to $n = 15$ for the lowest sampling bandwidth. Only the value at $n = 1$ is statistically significant suggesting Brownian motion with friction for high averaging times.

below $0.1\,\text{Hz}$, emphasized by Fig.C.4b. Values for lags $n > 1$ are not significant anymore.

Acknowledgments

I would like to express my sincerest gratitude to Prof. Martin Weides for giving me the opportunity to work on this PhD-project as well as his continuous and encouraging supervision and his great organizational skills. He has always made the time for many valuable discussions, created contacts to other experts in the field, and provided the necessary experimental equipment as fast as possible. I would also like to thank you for giving me the freedom and support to develop and test (my own) new ideas and for the many opportunities, including international conferences, where I could present my work.

I would also like to extend this gratitude to Prof. Alexey Ustinov for being my second examiner, for the use of the well-functioning infrastructure within his group, and his support during my PhD and HIRST scholarship.

My deepest appreciations go to Dr. Andre Schneider for his abundant help, his many good solutions to all sorts of physics problems as well as for his inspiring demeanor; to Micha Wildermuth for his unwavering patience in discussing open physics problems, his permanent willingness to offer valuable hands-on help and his being a great flat mate; to Alex Stehli for always sharing his huge knowledge and explaining the subtleties of many physics questions as well as for his friendly and witty attitude. Without you all, I would not have been able to realize many outcomes of this work. I owe a very important debt to you guys.

I would further like to thank Dr. Hannes Rotzinger for his valuable input, his help regarding experimental problems, his extensive introduction into cryo technique, his pleasant explanations and supportive advice going beyond physics.

I have been very happy to share such a fine working environment with exceptional colleagues, where everyone has also become a good friend and has made work more than enjoyable. First, my great office colleagues Dr. Alex Bilmes, Alex Stehli, and Dr. Yannick Schön, who all supported each other. Then, Dr. Jan Brehm, Martin Spiecker, Nico Voss, Max Kristen, Daria Gusenkova and Konrad Dapper. I am especially glad for the joint collaboration in operating the cryostats with

Karlsruhe, 07.05.2021   M.Sc. Tim Wolz